T2R2 東京科学大学 リサーチリポジトリ
Science Tokyo Research Repository

論文 / 著書情報
Article / Book Information

題目(和文)	
Title(English)	Ultrafast photoinduced dynamics of the electron donor-acceptor type metal-organic framework
著者(和文)	BANUSamiran
Author(English)	Samiran Banu
出典(和文)	学位:博士(理学), 学位授与機関:東京工業大学, 報告番号:甲第12666号, 授与年月日:2024年3月26日, 学位の種別:課程博士, 審査員:腰原 伸也,沖本 洋一,大島 康裕,河野 正規,谷口 耕治
Citation(English)	Degree:Doctor (Science), Conferring organization: Tokyo Institute of Technology, Report number:甲第12666号, Conferred date:2024/3/26, Degree Type:Course doctor, Examiner:,,,,
学位種別(和文)	博士論文
Category(English)	Doctoral Thesis
種別(和文)	要約
Type(English)	Outline

Powered by T2R2 (Science Tokyo Research Repository)

Ultrafast photoinduced dynamics of the electron donor-acceptor type metal-organic framework

By

Samiran Banu

Submitted to the Department of Chemistry, School of Science

Doctor of Philosophy

at the

TOKYO INSTITUTE OF TECHNOLOGY

Supervisors: Professor Shinya Koshihara and Professor Yoichi Okimoto

Koshihara-Okimoto Laboratory

Abstract

The photo-control of macroscopic physical properties in the solid state is widely known as photoinduced phase transition (PIPT). Ultrafast switching phenomena caused by PIPT have been particularly important because of their potential applications in optical data storage, fast-switching devices, sensors, etc.

Over the past two decades, a family of porous materials known as metal-organic frameworks (MOFs) has been developed significantly, opening a new avenue in molecular materials science. Because of their porous nature, MOF materials have shown potential applications for electrocatalysis, energy storage devices, gas sensor equipment, etc. Regrettably, ultrafast photocontrol of physical properties in MOF systems has rarely been reported. Nevertheless, MOFs with charge-transfer (CT)-type phase transitions may provide an ideal system for observing fast photo-responses of electronic states.

In the present study, as a target material for PIPT, we focused on the DA-type (where D = donor and A = acceptor) layered MOF system, $(NPr_4)_2[Fe_2(Cl_2An)_3]$ (prepared by Prof. Miyasaka's group, IMR, Tohoku Univ.), which exhibits two-step CT phase transition (T_c = 317 and 354 K). At T_c, CT occurs between Fe and Cl_2An ions, which magnetic, structural, and spectroscopic measurements have confirmed. This system's mechanism of phase transitions has been discussed as multi-stability due to the balance between the valence and the Coulomb interaction, like the neutral-ionic (NI) phase transition. It should be noted that there is no apparent structural change at each T_c, probably due to the rigid bond nature between Fe and Cl_2An ions, contrary to the existence of dimerization of the lattice in the typical NI system, TTF-CA. Therefore, the phase transition of this system can be viewed as a purely electronic one. Then, an efficient photoinduced CT phase transition can be expected without lattice structural deformation by weak photoexcitation.

Here, we observed highly efficient photoinduced CT dynamics in the DA-type layered MOF: $(NPr_4)_2[Fe_2(Cl_2An)_3]$ by using time-resolved spectroscopy with a pulse width of 90-fs at room temperature (RT: 300 K). The photoinduced spectral changes are similar to the thermally

induced spectral change at around 2.6 eV, suggesting photoinduced valence change of the Cl_2An ions. However, we observed a considerable difference in the spectral shapes in the CT transition and mid-IR regions. We found two unexpected new photoinduced absorption bands from the spectra analysis, one at the higher-energy side of the main CT band and the other in the mid-IR energy range—just immediately after photoexcitation. The observed spectral change strongly implies the disappearance of the local inversion center on the Cl_2An ion instantly upon photoexcitation, causing an ultrafast change in the lattice structure due to the softening of rigid bonds. This has never been realized in a thermal phase transition. These findings demonstrate that a new electronic state with a unique lattice structure—i.e., a photoinduced hidden state—appears in this MOF system at ultra-high speed (within 110 fs) upon photoexcitation at RT.

Early-stage dynamics for the formation of structurally modulated photoinduced hidden state, discussed in the previous section, is still unclear, and we thought of a way to visualize them in this study. Herein, we used pump-probe spectroscopy with nearly single-cycle optical, infrared pulses (pulse width ~ 6 fs) to investigate early-stage dynamics for photoinduced structurally modulated state formation. This study was done in collaboration with Prof Iwai's group at Tohoku University. After the initial large spectral change due to the photoinduced CT at Δt = 0 fs, there is a clear spectral change in the relaxation process (redshift of zero-crossing point) from 0 to 50 fs, suggesting sequential structural change corresponding to the "hidden state" we observed. Meanwhile, there is no further spectral change up to at least 500 fs. In addition, we observed coherent oscillations in the time evolution of $\Delta R/R$. According to the analysis of the coherent oscillations, we found the IR active and Raman inactive mode in the thermal equilibrium phases ~ 494 cm^{-1} becomes Raman active in the photoinduced state at least after 50 fs, which implies a photoinduced symmetry breaking of this material. Hence, we assumed that the formation timescale of the hidden state from the initial purely electronic excited state must be ~50 fs.

We have successfully demonstrated an efficient photoinduced CT conversion between Fe and Cl_2An ions ($Cl_2An^{3-} + Fe^{3+} \rightarrow Cl_2An^{2-} + Fe^{2+}$) at RT. But now we intend to observe the photoinduced reverse CT ($Fe^{2+} + Cl_2An^{2-} \rightarrow Fe^{3+} + Cl_2An^{3-}$), i.e., conversion from high-temperature (HT) to LT phase. We performed a time-resolved experiment to realize such thought by exciting the intramolecular transition in Cl_2An^{2-} ion (~ 2.6 eV) with $E \parallel$ chain for pump and probe pulses in the HT phase (380 K). The photoinduced $\Delta R/R$ spectrum at 2 ps can

be well reproduced by simulated ΔR/R spectrum in the CT energy range, suggesting a successful observation of photoinduced reverse CT between the Fe and Cl_2An ions. In addition to the above result, we observed a threshold behavior for realizing reverse CT for the pump excitation fluence, i.e., $I_{ex} > 1.0$ mJ/cm^2, suggesting the cooperativity in reverse CT.

In summary, we demonstrate ultrafast and efficient photoinduced charge-transfer dynamics, along with a unique lattice-structure modulation, occur within 50 fs in the donor–acceptor type metal-organic framework, $(NPr_4)_2[Fe_2(Cl_2An)_3]$, at room temperature. Also, we successfully demonstrated the observation of reverse charge transfer by exciting at 380 K. We believe the present study provides an essential first step toward realizing flexible photo-control of metal-organic frameworks and opening the way for developing magnetically active photo-switching metal-organic frameworks in such robust structures. This discovery will also represent a novel photoinduced phase transition material and enrich the study of optical properties of solid and fundamental physics.

Table of Contents

Chapter 1

1. Research Background

This chapter first describes the overview of the photoinduced phase transition (PIPT) phenomenon. The basic concepts of PIPT are explained by the renowned phenomenological model constructed in the early 2000s, and the historical background of PIPT research is reviewed. Subsequently, the concept of the DA-type system and its photoinduced responses is summarized. The basic overview of metal-organic framework systems is also depicted. At the end of this chapter, the objectives and the motivations for this research work are described.

1.1 Photoinduced phase transition (PIPT)

1.1.1 Overview of PIPT

A phase of matter is uniform concerning its physical and chemical properties. As defined by chemistry, thermodynamics, and other related fields, a phase transition (or phase change) is a physical transition between one state of a medium and another. Solids, liquids, gases, and plasma are the primary phases of matter, solid H_2O (ice) melting into liquid H_2O (water) is an example of a phase transition. However, free energy takes a global minimum at each temperature in all these phases, called an equilibrium phase.

For broad scientific interest, phase transitions accompanied by electronic, magnetic, dielectric, and structural changes in equilibrium conditions are fascinating from the perspective of research and application. These changes result from cooperative interactions between molecules/atoms under changing external conditions/ stimuli. As an example, the equilibrium phase transitions of transition metal oxides with a perovskite structure have been widely studied for several decades, including metal-to-insulator (M-to-I) transitions [1,2],

ferroelectricity [3], quantum paraelectricity [4], and superconductivity [5]. But in this research, we are mainly interested in phase transition induced by light, which invokes the question towards equilibrium phase transition; photo-irradiation excites materials to another potential surface with a different structure from the ground state.

Our next topic focuses on nonequilibrium phases caused by excitations or stimulation. Although these states usually have higher energies than the equilibrium state, depending on how they are stimulated or excited, we can get many more varieties of states, regardless of the equilibrium phase. But surely, they also relax to the starting equilibrium phase after a while. From a research and practical standpoint, phase transitions that emerge from cooperative interactions between constituent molecules/atoms under varying external conditions and are of interest are followed by electronic, magnetic, dielectric, and structural changes.

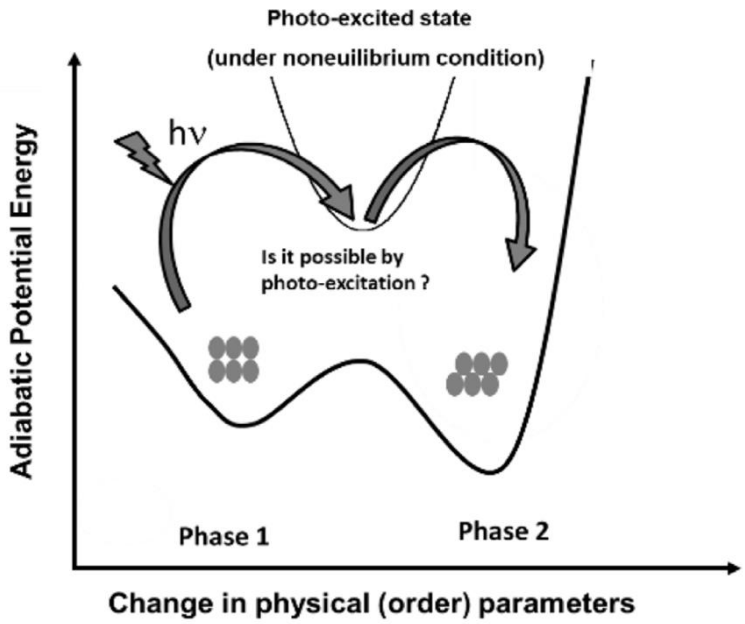

Fig. 1.1: Schematic conceptualizing the photoinduced phase transition (PIPT). The phase transition from phase 1 to another phase (phase 2) of the adiabatic potential energy is induced through the photo-excited state [6].

Among all external stimuli, to control materials functionality in a fast, non-thermal, and contactless way, it is essential to understand how molecular systems with strong electron-electron, electron-lattice, and magnetic correlations interact with light. Materials are excited by photo-irradiation to a distinct potential surface with a structure from their ground state (see Phase 1 in Fig. 1.1). Phase 2 in Fig. 1.1 represents a situation where relaxation via an excited-state potential surface could cause a material to change phases Under nonequilibrium conditions. Generally, this type of switch is known as photoinduced phase transition (PIPT) [6,7].

In 1997, Nasu [6] added energy relaxation from the excitonic state to collective excitation, mediated by lattice-relaxed excitons, to the theoretical framework of charge-density-wave (CDW) systems. According to Fig. 1.2, the concept of PIPT has been generalized by this framework. Because the classical (incoherent) energy-relaxation process is a part of this family of PIPT occurrences, it is called classical (incoherent) PIPT. Here, the vertical axis is equivalent to the adiabatic potential energy in a microscopic viewpoint. The horizontal axis corresponds to the configuration coordinate for structural phase transition, magnetization for magnetic phase transition, etc., which are usually considered as order parameters. After photoexcitation, when the material absorbs the photon energy, the ground state at the minimum free energy is vertically excited to the Frank-Condon state (according to the Franck–Condon principle). In general, the time scale of the electronic excitation process occurs within femtoseconds (10^{-15} s), which is nearly the reciprocal of the excitation photon energy. Since this process is too fast, the lattice structural configurations are considered frozen in this time scale. The Frank-Condon state with high excess energy is unstable. Thus, it relaxes too many stable states accompanying microscopic structural changes. Through the relaxation process, a part of the excited state converts to the initial state, while another part goes to a new hidden macroscopic order, which

researchers are interested in studying. The new order prevails due to the inherent cooperative interaction known as the domino effect, and excited domains are formed. This metastable condition, also known as the "false ground state," is located at a local free energy minimum and is separated from the real ground state by an energy barrier greater than the thermal energy. As a result, the new phase remains stable (or metastable) there. The total processes of PIPT are conducted in this manner.

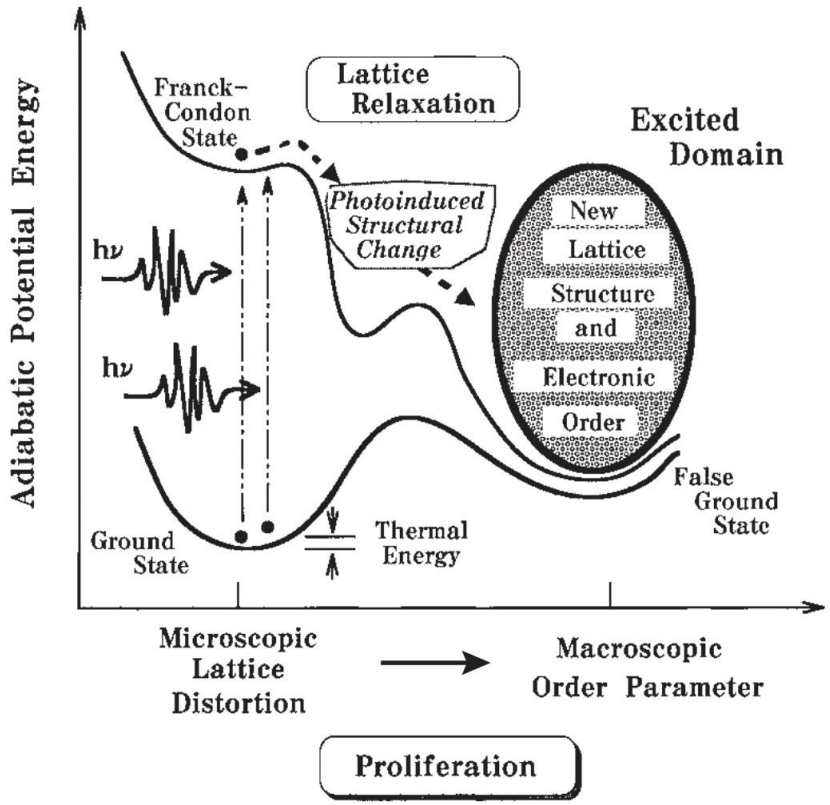

Fig. 1.2: Schematic diagram of PIPT dynamics proposed by Prof. Nasu. [6]

1.1.2 History of PIPT research

PIPT research began with the 1984 report on LIESST (Light Induced Excited Spin State Trapping) in spin-crossover complexes [8]. Starting from 1990 till now, extensive studies on PIPT have been performed. Realistic examples are reported for various materials such as charge transfer (CT) crystals [9-13], π-conjugated polymers [14,15], insulator-to-metal transition in metal-oxides [16-18], spin crossover complexes [19-22], Prussian-blue analogs [23], the quantum structure of diluted magnetic semiconductors [24], low-dimensional transition metal-organic complexes [25] etc. and many more.

Two pioneering studies had the greatest impact on subsequent research in this field. One is about the PIPT of TTF-CA (tetrathiafulvalene-p-chloranil) [11,13], where the photoinduced neutral (N) to ionic (I) phase transition served as the first example of the transitory PIPT from the ground state to a metastable phase. Another one is the $\pi-$conjugated polymer, polydiacetylenes [14,15], which showed a reversible structural phase transition from a metastable phase to its ground state for the first time.

From here, the research for PIPT has been extensively performed and has shown drastic progress. Various metastable phases have been observed in strongly correlated materials, such as transition metal oxides, metal complexes, and low-dimensional organic conductors. For example, insulator−metal phase transitions in organic complex $(EDO\text{-}TTF)_2PF_6$ [26, 27] or in transition metal oxides like VO_2 [18, 28, 29] were reported. For polycrystalline samples of $Pr_{0.5}Ca_{0.5}CoO_3$ (PCCO), the spin-crossover effect and insulator–metal transition in PCCO and its photo-response were also studied [30]. K-TCNQ is a well-known spin Peierls transition system with dimerization of its constituents and magnetic changes. This crystal dimerization melt causes a PIPT from spin Peierls to non-dimerized phases.

Not only has experimental research progressed, but many theoretical studies have also been performed. Several first principle calculations have been conducted on spin-crossover

materials [31, 32]. PIPT was phenomenologically interpreted by Nasu in the early 2000s [6], as described in the previous section. The idea of creating diamond structures from graphite using PIPT was proposed in 2009 [33, 34].

In the next section, with the invention of ultrafast spectroscopy methods, how the PIPT research provides a significant advancement in science and technology is discussed.

1.1.3 Ultrafast spectroscopy in PIPT research

Photoinduced processes are always associated with short-lived reaction intermediates in their dynamical changes (transient or metastable states). To understand the nature of the dynamical processes related to PIPT, the PIPT mechanism has to be understood phenomenologically without considering the detailed processes connecting the true and false ground states. The dynamical processes are usually complicated, the relaxation processes involve lots of electron-electron, electron-lattice, or collective interactions. Electron-electron scattering typically takes place over a time scale of 10 fs (femtosecond), while electron-phonon scattering takes place over a timescale of several 100 fs [35] as shown in Fig. 1.3. Thus, to explore the correlation between the degree of freedom related to spin, and electronic and structural motions in solid-state materials, we need ultrafast spectroscopy based on pump-probe measurement with enough resolution for direct visualization of their dynamics.

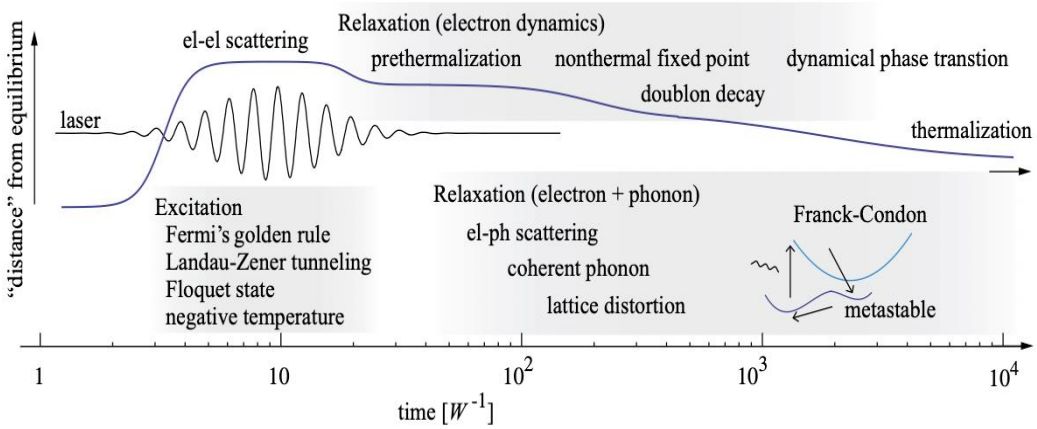

Fig. 1.3: Schematic of the nonequilibrium relaxation dynamics in a pump-probe experiment

was summarized by Aoki et al. [35]. Here, the time scale is rescaled corresponding to the energies of the phenomena. It suggests the time scale for observing electron-electron and electron-phonon interaction lies between 10 to a few 100 fs (femtosecond) time scales. Meanwhile, dynamic phase transition can be observed in ps (picosecond) timescale.

With the advent of ultrashort light pulses and sophisticated spectroscopic techniques, detection and understanding of photoinduced dynamics processes have seen an impetuous growth. The rapid development of femtosecond lasers, pulsed X-rays, and pulsed electron techniques during the last 20 years has enabled the ultrafast classical (incoherent) PIPT research field. New measuring techniques, such as femtosecond time-resolved photoemission spectroscopy and electron diffraction, will also be introduced as potent new instruments in PIPT research.

1.2 Electron donor-acceptor (DA)-type systems

Photo control of the electronic state is one of the key steps for developing light-harvesting processes for energy conversion, photocatalysts, high-speed electronic devices, etc. For this purpose, DA-type (D = donor and A = acceptor) systems are considered to be ideal and expected to be suitable for research and development.

Photoinduced electron transfer is an excited state electron transfer process by which an excited electron is transferred from D to A.

1.2.1 DA-type thermally driven electron-transfer (TDET) systems

In recent two decades, it has become increasingly common to use molecular systems to develop new functional materials, including organic conductors, molecular materials to develop optoelectronics, optical data storage, fast-switching devices, molecular magnets, etc. The possibility of inducing a reversible change in the electronic distribution of a molecular system by varying appropriate external parameters like temperature (T), pressure (P), light ($h\nu$), etc., paves the way for a new research field to discuss at the molecular level. As a class of such

functional materials, electron DA-type thermally driven electron-transfer (TDET) systems [36-44] are an attractive target because such external stimuli can easily trigger their molecular properties.

Quinonoid Metal Complexes

Quinonoid metal complexes [36, 45-47] are highly attractive materials for designing materials with potential technological applications due to their peculiar red-ox active nature. Here, primarily metal-polyoxolene complexes exhibit intramolecular electron transfer processes involving either the ligand and the metal ion or the two di-oxolene moieties of a properly designed ligand, thus inducing electronic bistability. These systems are potentially utilized as molecular switches because they can transition between the two metastable electronic states when exposed to different external stimuli such as temperature, pressure, light, or pH [48,49]. As an example of such system is $Co_2(CTH)_2(DHBQ)(PF_6)_3$ (where CTH = dl-5,7,7,12,14,14-hexamethyl-1,4,8,11-tetraazacyclotetradecane and DHBQ = deprotonated form of 2,5-dihydroxy-1,4-benzoquinone) [36].

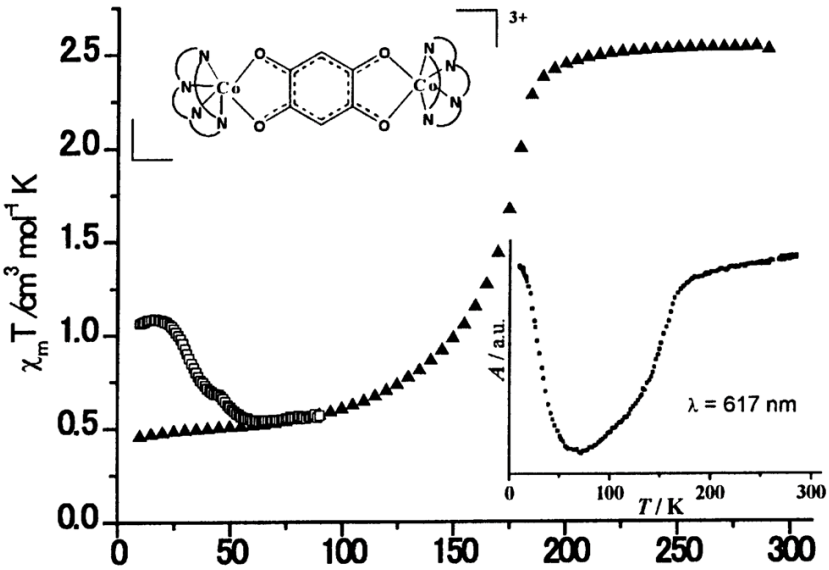

Fig. 1.4: Temperature dependence of $\chi_M T$ of complex $[\{Co(CTH)\}_2(DHBQ)](PF_6)_3$ measured before (▲) and after (□) irradiation at 647 nm. The temperature dependence of the reflectivity

at 617 $\pm$ 5 nm is also reported in the bottom right inset. On the top left inset, a schematic view of the cationic part of the complex is shown [36].

Here, the temperature-dependent magnetic susceptibility measurements showed that a transition between two different species (mixed valence hs-Co^{II}-Co^{III}) occurs below 200 K (Fig. 1.4). The more interesting is that this complex was found to undergo valence tautomerism upon light irradiation. Indeed, if light irradiation at 647.1 - 676.4 nm is applied at low temperatures, the magnetic moment immediately increases up to χ_MT of 1.2 cm^3 K mol^{-1}, as shown in Fig. 1.4.

DA–type neutral-ionic (N-I) phase transition systems

The neutral−ionic (N−I) phase transition in a DA pair, which involves electron transfer between distinct neutral (N: D^0A^0) and ionic (I: D^+A^-) valence states, is an intriguing switching phenomenon that drastically changes the fundamental physical properties of this pair, such as spin states, electronic transport, and electrical polarization. For example, the compound $[Ru_2(2,3,5,6\text{-}F_4PhCO_2)_4(DMDCNQI)]\cdot 2(p\text{-xylene})$ (1;2,3,5,6-$F_4PhCO_2^-$ = 2,3,5,6-tetrafluorobenzoate; DMDCNQI = 2, 5-dimethyl-*N, N*′- dicyanoquinonediimine), showed a definite evidence for the stepwise N-I transitions in the temperature range between 210K (= T_2) and 270K (= T_1) with N phase at $T > T_1$ and I phase at $T < T_2$ [50] caused by contributions from anisotropic interchain Coulomb interactions in a metal-complex-based covalently bonded DA chain. As shown in Fig. 1.5(a), on $DMDCNQI^{\delta-}$, δ was estimated by the Kistenmacher relationship [51], the DMDCNQI moiety has a quinonoid structure around room temperature. In other words, the chain is neutral (N form) when $T > T_1$. Then DMDCNQI converts to a quasi-benzenoid form, meaning the chain becomes ionic (I form) with $\delta \approx 1$ when $T < T_2$. The IM form is a 'stage of charge' with a formal $\delta \sim 0.5$ between T_1 and T_2. The arrangements of the

N and I chain in the I phase (top), IM phase (middle), and N phase (bottom) onto the *bc* plane are shown in Fig. 1.5(b), respectively.

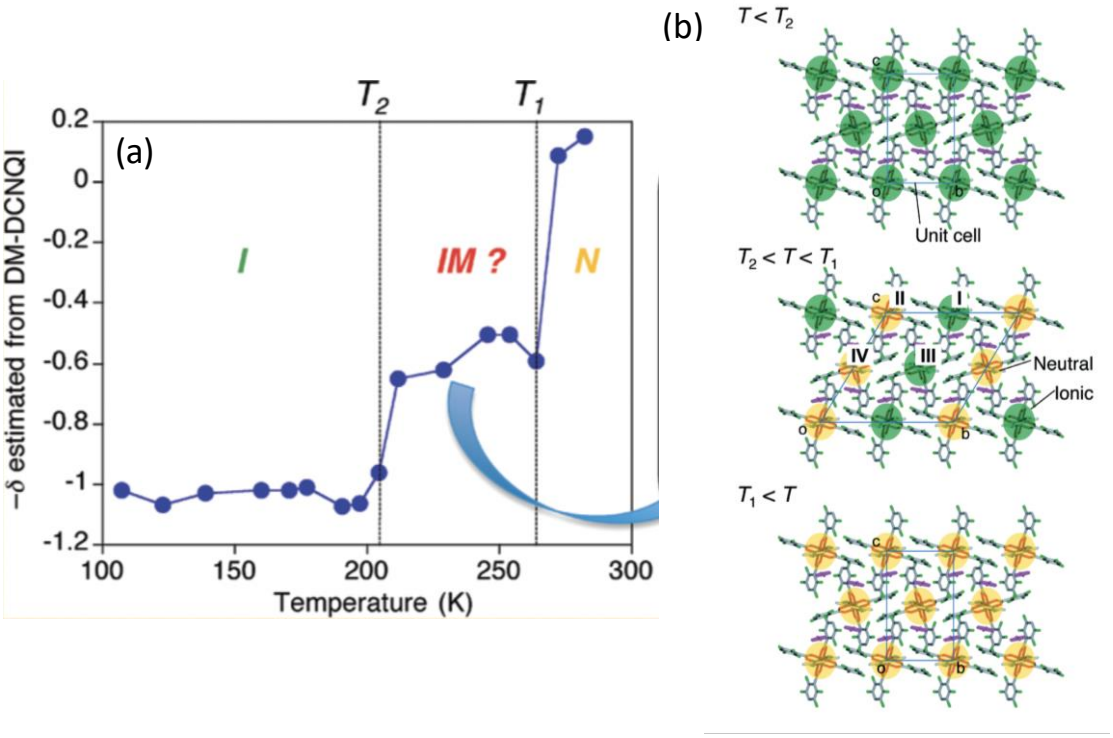

Fig. 1.5: (a) The degree of charge transfer, -δ on the DMDCNQI subunit is estimated using the Kistenmacher relationship. (b) Arrangements of N and I chains in the I phase below T_2 (top), IM phase between T_1 and T_2 (middle), and N phase above T_1 (bottom) projected onto the bc plane. Yellow and green denote the N and I chains, respectively [50].

In the category of organic DA-type systems, one of the famous examples is TTF-CA (where TTF = tetrathiafulvalene and CA = *p*-chloranil), which exhibits a reversible electronic phase transition has been discovered at which organic charge-transfer solid is transformed from neutral to ionic phases under pressure [52 - 55]. On cooling a sublimed film of TTF-CA, the phase transition appears as a distinct, reversible change in color from yellow to red, seen near 77 K. The optical-absorption spectrum at 300 K for such a sublimed film and a powdered sample dispersed in KBr are compared in Fig. 1 with that of a film at ~ 11 K. The absorption

of the sublimed film above and below the N-I phase transition is shown in Fig. 1.6, suggesting the difference in spectral behaviors between the N and I phases. Optical, infrared, and Raman measurements by Torrance et al. (1981) indicate that this is a reversible transition from a nominally N solid to a nominally I salt. since this is the most prototypical compound that shows the N - I transition not only by applying hydrostatic pressure above P_c, (equal to 11 kbar) but by lowering the temperature below T_c.

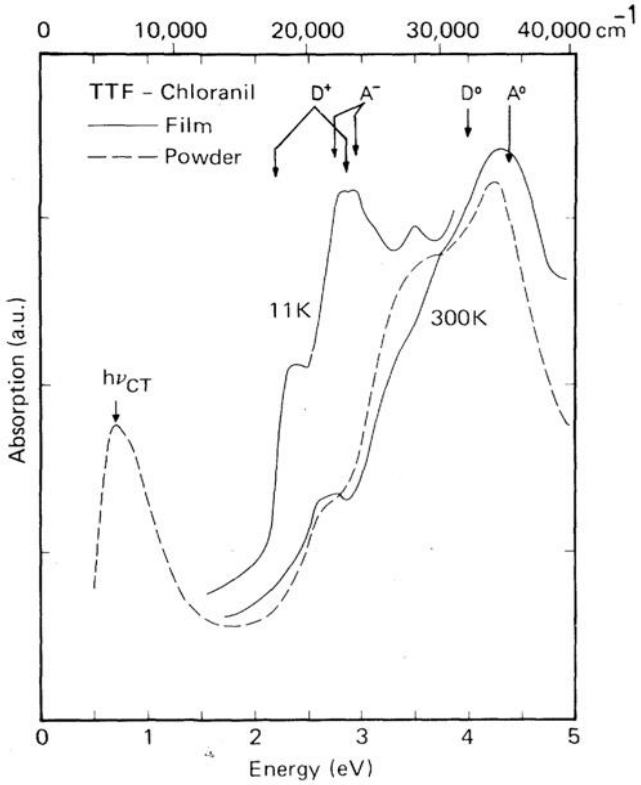

Fig. 1.6: Absorption spectra of sublimed film above and below the N-I phase transition in TTF-CA [53]. Arrows represent absorption peaks of neutral and ionized molecules in solution.

1.2.2 PIPT in DA-type systems

A study of the photo-response of TDET systems will be attractive for achieving fast, non-thermal, and contactless control of crystal functionality. The reason is that a charge-transfer (CT)-type transition—which has the lowest photoexcitation energy in such TDET systems—

can be an efficient mechanism for controlling electron/spin functionality. Such a DA-type TDET system is usually a molecular material with a low-dimensional, electron-correlated lattice, as defined by anisotropically directed electronic correlations or chemical bonds between the constituent molecules/ions. The low dimensionality of such an electron-correlated lattice may induce several kinds of instability associated with the electrons, lattice, and spin. These are critical factors for achieving an efficient photo-response because of the inherently cooperative electron–electron, electron–lattice, and magnetic interactions that are strongly expected.

Most neutral–ionic (N–I) phase-transition systems [50, 52, 56] are one-dimensional (1D) DA-type systems, although some inter-chain Coulombic interactions have been observed [50]. In particular, TTF–CA crystals (where TTF = tetrathiafulvalene and CA = *p*-chloranil) exhibit highly efficient photoinduced N–I phase conversions [57–63]—so-called PIPTs. In 1990, Koshihara et al. [57] found that a local charge-transfer excitation on the DA pair leads to a semi-macroscopic valence change from the quasi-ionic (D^+A^-) to quasineutral (D^0A^0) states in organic molecular-compound TTF-CA with mixed DA stacks. They have done photoirradiation at energies above the CT gap (at 2.0-2.5 eV) utilizing a pulse dye laser (10 ns) or a chopped light (400 Hz) from a CW Argon laser. The anomalous photoconductivity properties can be attributed to photogenerated N to I domain walls. Fig. 1.7 shows the reflectance spectra of TTF-CA for the neutral and ionic phases taken on the (001) surface at 90 and 77 K, respectively.

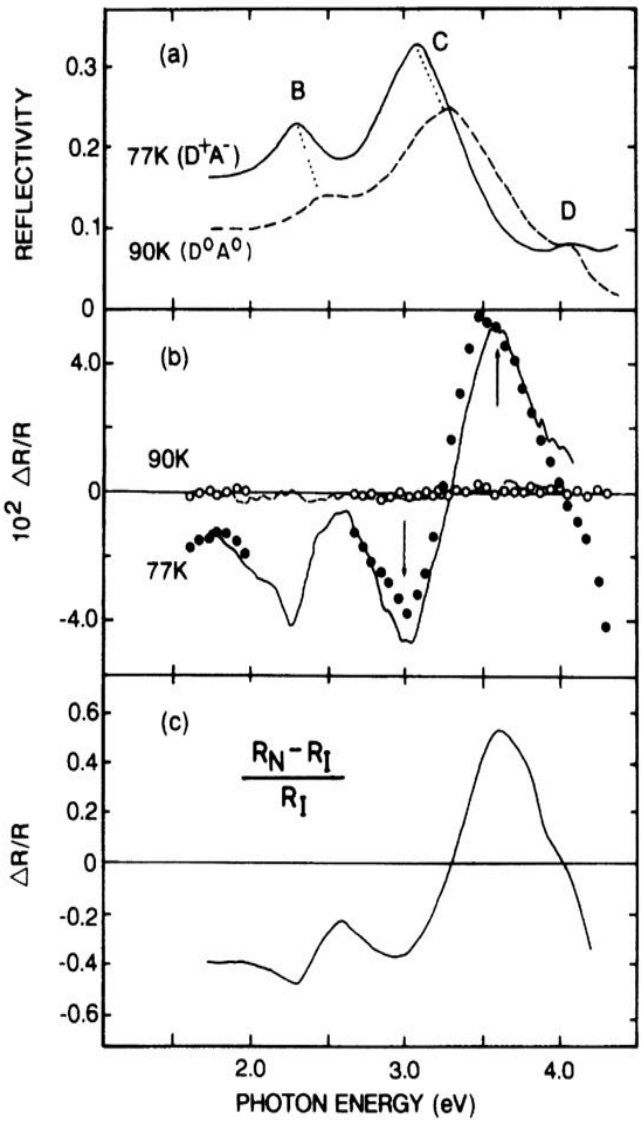

Fig. 1.7: (a) reflectance spectra and (b) photo reflectance $\Delta R/R$ spectra for molecular excitations (E^a) at 77 K (ionic phase) and 90 K (neutral phase) in TTF-CA crystal. The ordinate scale for $\Delta R/R$ (b) is for the results of pulse excitation shown by open (90 K) and solid (77 K) circles. Solid and broken lines represent the result of CW laser excitation. The spectrum (c) is the calculated differential spectra using the respective ionic phase (R_I) and neutral phase (R_N) spectra shown in (a) [57].

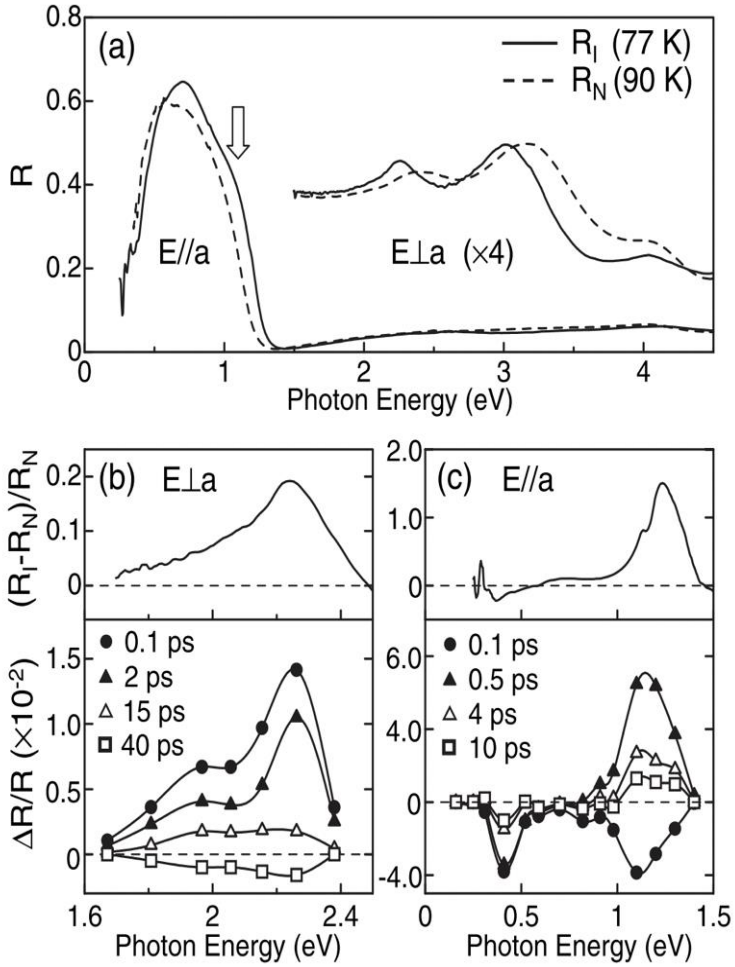

Fig. 1.8: (a) Polarized reflectivity spectra of TTF-CA in the I phase at 77 K (R_I) and in the N phase at 90 K (R_N). (b), (c) Photoinduced $\Delta R/R$ at 90 K for the IMT band (b) and the CT band (c) for the 1.55 eV excitation with E∥a [64].

Whereas in Fig. 1.7(b), photoinduced changes of reflectivity ($\Delta R/R$) are plotted in the neutral and ionic phases, measured at 90 and 77 K, respectively. The photoinduced $\Delta R/R$ spectra were recorded as a relative difference ($\Delta R/R$) between the spectra with and without photoirradiation. Thus, photo-induced I to N phase transition can be achieved. In contrast, N to I photo-induced phase transition cannot be observed at that time due to the limitation of time resolution of the time-resolved optical setup.

Then, in 2006, Iwai et al. [64] successfully reported cooperative coherent control of this lattice

phonon coupled with charge in the dynamical process of the photoinduced N-I transition in TTF-CA, as shown in Fig 1.8. To measure the photoinduced $\Delta R/R$ spectrum, they used a Ti: sapphire regenerative amplifier operating at 1 kHz as a light source. Output from the amplifier was 800 nm (1.55 eV) with a pulse width of 130 fs. In Figure 1.8, the experimental result clearly illustrates the observation of a photoinduced N to I phase transition in TTF-CA [64].

In summary, PIPTs provide a distinctive platform for studying non-adiabatic transitions. As a result of the technological breakthroughs provided by ultrafast lasers, they have arisen as a thriving research topic in recent decades. The initial state that appears immediately after photoexcitation and from which order recovers is far from equilibrium during these transitions. Because of the discovery of this property, liquid crystals and their applications, such as optical devices and photo-controlled molecular motors, can now be aligned rapidly. Photo-control of the neutral-ionic phase transition in CT complexes has been established, and various characteristics (including ultrafast electronic and lattice dynamics) have been thoroughly investigated. The photo-controls of charge density wave, charge ordering, and spin Peierls systems have also been investigated. In addition, a wide range of photoinduced M-to-I phase transitions have been studied. Here, the primary goal of my research is to demonstrate the occurrence of the ultrafast light field (including THz, IR, and visible regions) induced phase switching (PIPT).

The realistic target of my research for the PIPT study is a DA-type metal-organic framework (MOF) system. Then, a short overview of MOFs and their properties and applications are described in the net section.

1.3 An Overview of Metal-organic Frameworks (MOFs)

Here, DA - the type MOF system is chosen as our target material to study photoinduced dynamics in molecular crystal systems. We employed time-resolved spectroscopy to examine the ultrafast photoinduced dynamics of DA-type MOF material primarily. Therefore, it is essential to comprehend the underlying idea behind MOF materials and some of their fundamental characteristics, such as classification, application, and photoinduced responses. So, the key information in this section is to provide the fundamental physiochemical properties of MOF systems.

1.3.1 Introduction

Metal-organic frameworks (MOFs) are made when organic ligands act as linkers and metal ions act as nodes in chemical bonds. This process results in periodic network crystalline structures with high porosities and significant surface areas, which support their potential use in a variety of scientific and technological fields, particularly for gas storage [65], separation [66, 67], and catalysis [68–70]. Scientists at the time were interested in Tomic's initial article about MOFs and porous materials, published in 1965 [71]. Material importance is determined by the role they play in human life and the impact they have on technological fields in the future. The functionalization of MOF systems has been developed significantly during the past two decades and has opened a new avenue in molecular materials science, especially because of their porous nature. The potential applications of these materials have motivated many chemists to design new types of porous molecular materials, particularly for gas storage, separation, and catalysis. A materializing competitor to traditional porous materials like activated carbons and zeolites, MOFs have a typical broad inner surface area (often 500–7000 m^2/g), structural flexibility, programmable porosity, changeable organic functionality, and physical/thermal stability. Late in the 1990s, Omar Yaghi of UC Berkeley invented the rapidly

expanding field of research known as MOFs [72]. There have been claims that there are more than 90000 MOF structures, and the number keeps rising. MOFs are made by coordinatively enmeshing a metal ion with organic linkers (Fig. 1.9), resulting in unfolded frameworks with a vast surface area, a big pore volume, and a central vision of limitless porosity.

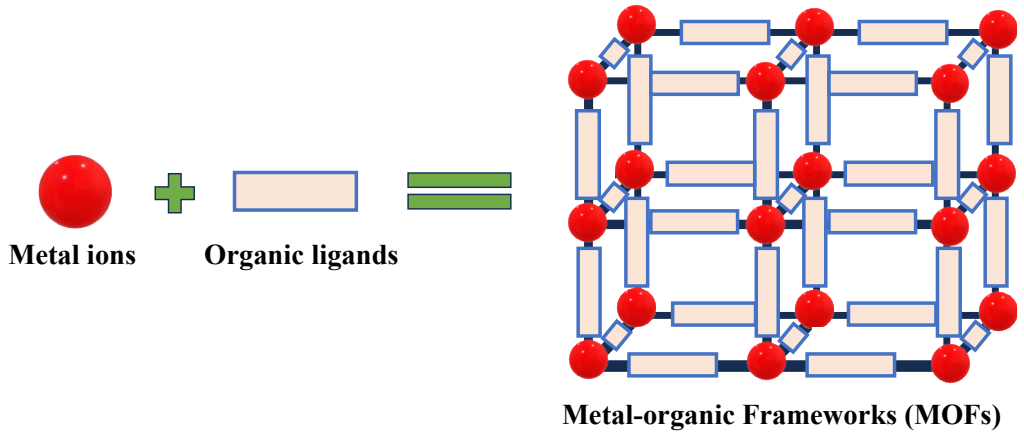

Fig. 1.9: Schematic representation of the formation of MOF structures by forming chemical bonds between the metal ions as nodes and the organic molecule as a linker.

1.3.2 Classification of MOFs

"MOFs" is the abbreviation of metal-organic frameworks, which is usually used as a general name for the group of compounds. Depending on their component units, MOFs could be divided into various groupings. A few examples are represented below, and some are shown in Fig. 1.10. Several review papers on MOFs have more detailed descriptions [73].

(a) Isoreticular MOFs: Isoreticular MOFs are synthesized by $[Zn_4O]^{6+}$ secondary building units and a series of aromatic carboxylates [74, 75]. These MOFs are octahedral microporous crystalline materials. (b) Zeolitic Imidazolate Frameworks (ZIFs): They are zeolite topological structured materials. ZIFs comprise ZIF-8, ZIF-90, ZIF-L, ZIF-71, ZIF-67, ZIF-7, etc. [76]. ZIFs are employed as a network to create innovative MOF composites because they have huge

pores and high chemical and thermal durability.

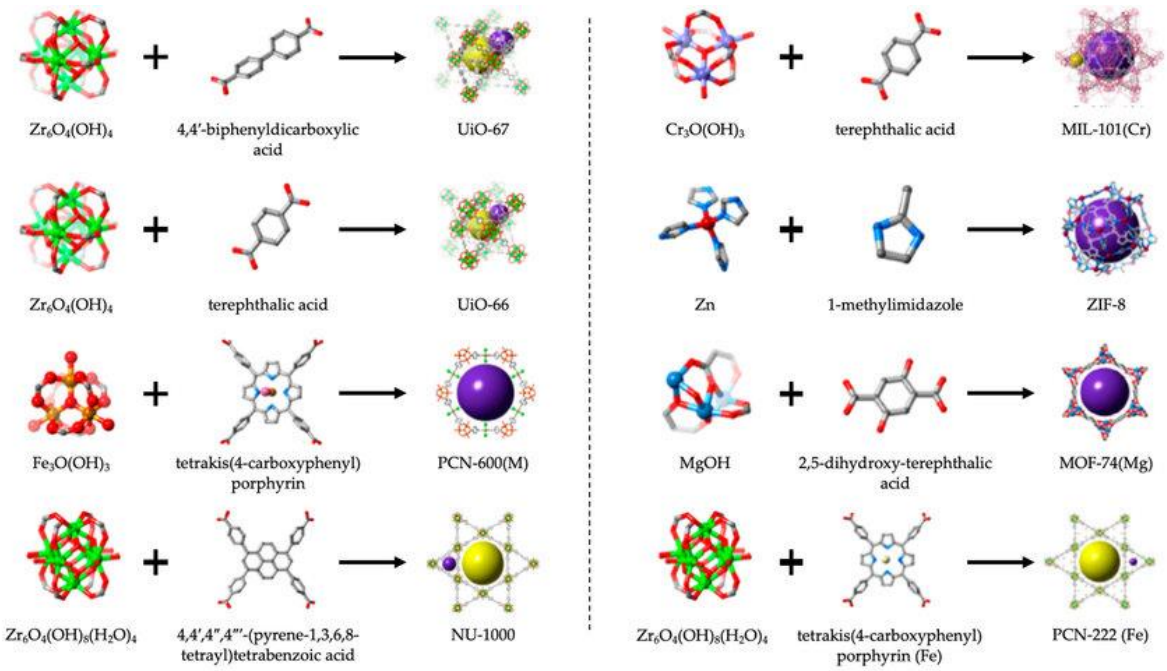

Fig. 1.10: Examples of different metal–organic framework structures with their corresponding metallic clusters and organic linkers. The figure is adapted from ref. [82].

(c) Porous Coordination Networks (PCNs): PCNs are stereo-octahedron materials having a hole-cage-hole topology and a three-dimensional structure. Some of the PCNs are PCN-333, PCN-224, PCN-222, and PCN-57. [76], (d) Materials Institute Lavoisier (MIL) MOFs: MIL MOFs are synthesized using various elements that have valence electrons and an organic compound containing two carboxylic functional groups. MIL MOFs contain MIL-101, MIL-100, MIL-53, MIL-88, MIL-125, etc. [76, 77, 78]. (e) Porous Coordination Polymers (PCPs): PCP materials are synthesized by carboxylic acid, pyridine, and its derivative as the primary building units and transition metal ions as the secondary building units [76]. PCPs exhibit magnificent characteristics in biomacromolecule separation and heterogeneous catalysis [79, 80]. (f) University of Oslo (UiO) MOFs: A University of Oslo MOF based on dicarboxylic acid as the primary building unit and $Zr_6(\mu_3\text{-}O)_4(\mu_3\text{-}OH)$ as the secondary building units was first

synthesized by Lillerud and coworkers [81]. The abovementioned varieties are the most popular and common MOFs synthesized and employed in various applications.

1.3.3 Applications of MOF systems

Because of a unique combination of these three main properties—crystallinity, porosity, and the existence of strong metal–ligand interactions—MOFs are a distinct class of materials. MOFs are useful in a wide range of intended applications, including gas storage and delivery, drug delivery, rechargeable batteries, super-capacitors, separation membranes, catalysis, sensing, etc., thanks to their high surface area, small density, structural flexibility, and tunable pore functionality. Fig. 1.11 shows the schematic or pictorial representation of a wide range of applications of MOFs [83]. Among them, some major fields of applications are discussed here. For details, MOFs are widely discussed in review articles, such as ref [72, 84], which emphasizes their real-world applications.

(a) Gas Storage: Because of the distinctive structure of MOFs, their primary function is for gas storage due to their substantial surface area. Although zeolites and activated carbons are widely used, they have poor CO_2 absorption capacities and selective separation. Due to their high surface area, adjustable pore sizes, and customizable and programmable framework architectures and topologies, MOFs are ideal for collecting and separating CO_2. The perfect potential of this behavior in carrying out both CO_2/N_2 and CO_2/CH_4 separations was confirmed by an actual breakthrough test [85]. In a study by Yoon et al., the reduction was carried out using Na_2SO_3 as a reducing agent after Cu(I) ions were added to a mesoporous MOF using a simple technique employing $CuCl_2$ loading. Large C_3H_6 working capacity (1.3 mmoL/g) at 10e100 kPa and C_3H_6/C_3H_8 selectivity four times higher than the parent MOF were the results of the Cu(I) incorporation [86].

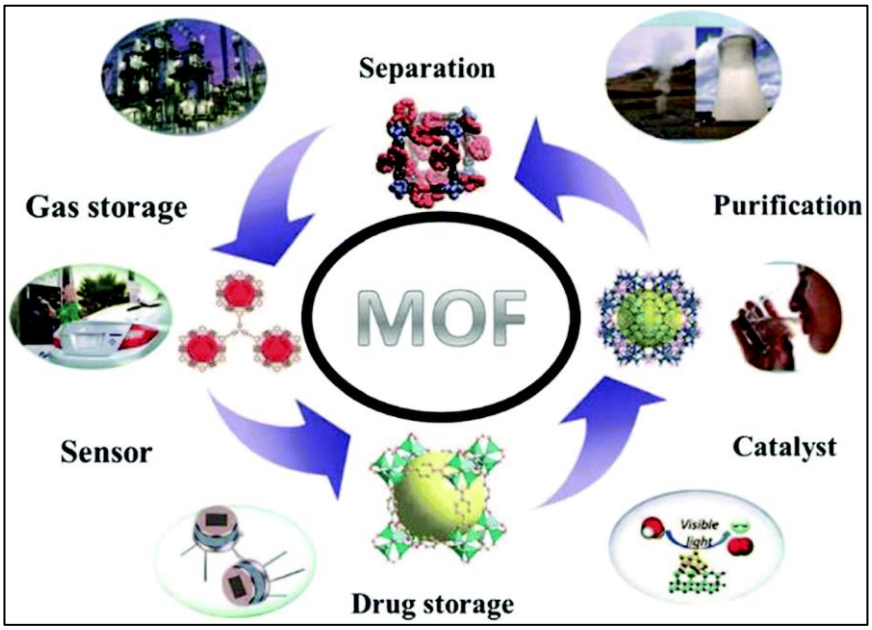

Fig. 1.11: A schematic representation of the different applications of MOF systems, adopted from ref. [83],

(b) Catalysis: MOFs have many properties that commend them as catalysts: High catalytic reaction rates per unit volume require high interior surface areas and active site density. (i) Possibilities for complementing catalytic group addition during and after MOF production. (ii) Possibilities to modify MOF pore architectures to enable pores big enough for quick transit, shape-selective catalysis, confinement effects to stabilize encapsulated catalytic species, and positioning several catalytic groups in close proximity conditions. The application of MOFs to catalysis is described in ref. [87 - 90] (c) Sensors: A few instances are described concerning the beginning materials, the integration of the MOF as a sensor component, the biosensor, and the fabrication process. Ru et al. synthesized a MIL-101-NH_2-SO_3H as an inorganic nano-filler that exhibited the best sensing features by the organic-inorganic humidity sensor based on the composite material (SPEEK/MNS-30%) [91]. Detection of both UO_2^{2+} and Cu^{2+} with the application of a luminescent europium organic framework, $[Eu_2(MTBC)(OH)_2(DMF)_3(H_2O)_4].2DMF.7H_2O$ was assessed by Liu et al. [92]. (d) Biomedical applications: Due

to its incredible size, composition, and functionalized pore surface, MOFs are being researched as vehicles for delivering loaded goods to targeted places. The following are the unique benefits of MOFs as potential drug delivery materials: (i) highly adjustable characteristics and pore size, (ii) increased drug loading capacity, and (iii) manageable multifunction [93-96].

1.3.4 DA-type MOF systems

The development of MOFs is a highly promising platform for constructing DA-type systems. Developing a new DA system in MOFs has also become a valuable method for the applications of MOF systems in optics, electronics, magnets, catalysis, and anti-counterfeiting research fields [97-103]. These materials lay the foundation for charge transfer (CT) and energy transfer (ET) based properties. This fact implies a significant benefit for our research since it can be easily tuned through photoexcitation. In the following sections, we summarize the technical development of D-A MOFs and their design, construction, and property advantages.

1.3.4.1 Construction of DA-type MOF systems

DA MOFs can be constructed using the donor and acceptor units as part of the frame or as guests - a typical configuration for organic DA cocrystal stacking. The DA MOFs can generally be classified according to their structural feature. In general, DA MOFs could be classified according to their structural features [104], such as (1) DA MOFs based on host–guest structures (Fig. 2.4 (a)) [105,106], (2) DA MOFs based on donor–acceptor type ligands (Fig. 1.12 (b)) [107], (3) DA MOFs based on metal ion connected DA systems (Fig. 1.12 (c)) [108] and (4) DA MOFs featuring interlocked structures (Fig. 2.4 (d)) [109].

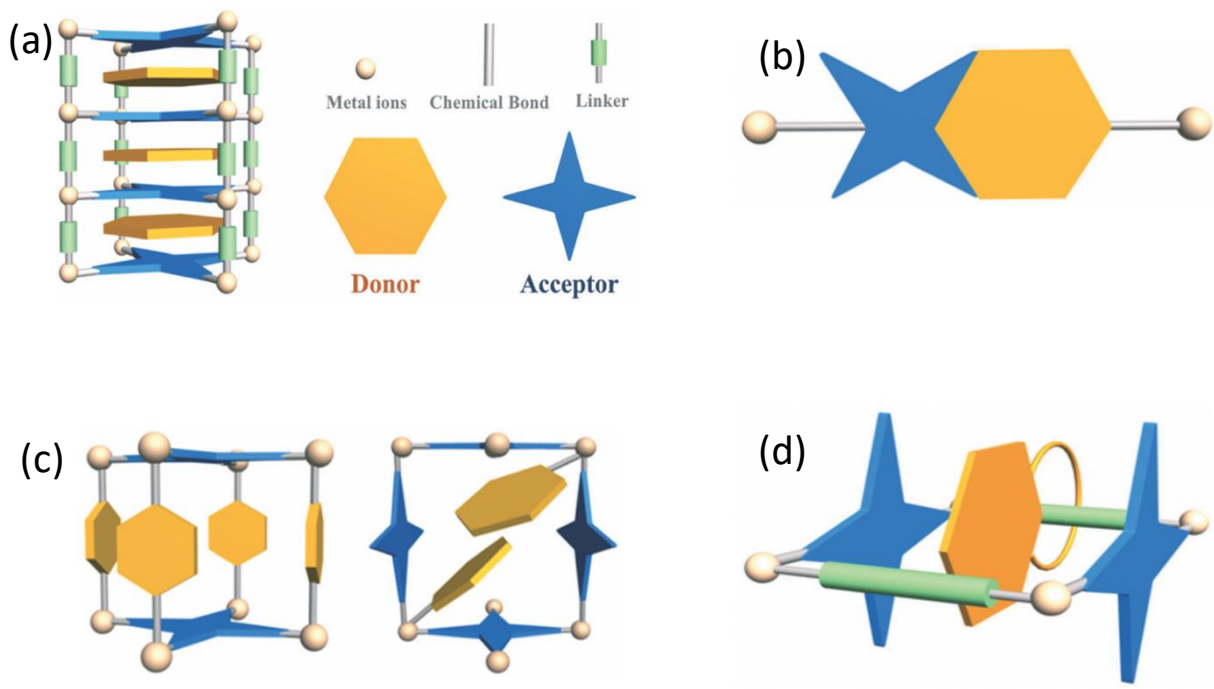

Fig. 1.12: (a) DA-based MOF with the host framework as the acceptor and guest as the donor. (b) DA system in MOFs with ligands containing donor and acceptor moieties. (c) Two different forms of DA MOF with donors and acceptors connected by metal ions. (d) DA MOF with A as the main framework and D as an interlocked moiety [104].

1.3.4.2 Properties of DA-type MOFs

The interaction between the donor and acceptor results in CT and ET, determining materials' optical and electrical properties. Renewal of optical and electrical properties is also essential to developing industrial optical and electrical devices; therefore, studying the interaction between the donor and acceptor is crucial. It will also help us progress in our research as we are interested in exploring the ultrafast CT dynamics of DA-type MOF systems.

Optical properties of DA-type MOFs: As previously mentioned, in the DA system, the precise distance between the donor and acceptor and the proper degree of electron cloud overlap between the donor and acceptor may promote charge transfer and energy transfer. Reviews and

articles have discussed the energy transfer mechanism and occurrence conditions [110,111]. Energy transfer can result in luminescence enhancement or quenching [112,113], which is useful for detection and optical switching.

Electrical properties of DA-based MOFs: Charge separation from the charge-localization effect of the donor or acceptor in the ground state and the CT interaction between the donor and acceptor moieties provide the foundation for DA-based MOFs to accomplish the electrical characteristics. The arrangement of the components is essential to the charge transport properties of DA MOFs because the donor and acceptor components in the DA system can form charge transport channels under radiation. Electrons and holes flow through the channels and ligands, which could provide the electric current path and unfold various semiconductor material properties. The merits of using DA MOFs to obtain electrical properties are repotted by many research groups [114,115].

In addition to the optical and electrical properties described above, DA MOFs with CT or ET interaction may exhibit properties such as magnetism [116] and photothermal conversion [117].

1.3.5 Short description of flexible MOFs

The MOFs can be classified into two categories; one is rigid MOF, and the other is flexible MOF. Rigid MOFs are just regular MOFs with porous frames and stiff backbones that are comparably stable and strong. Whereas flexible MOFs combine cooperative structural transformability with the crystalline order of the underlying coordination network. These materials have adjustable molecular design responses to various physical and chemical stimuli, which is not true for any known solid-state materials (such as rigid MOFs). Here, an easy-to-understand example of a rigid and flexible MOF—MIL-101(Cr) [rigid] and MIL-53(Cr) [flexible]—is addressed to show how these two MOFs differ when compared to one another in terms of their chemical and physical characteristics [118, 119]. In this article, their absorption behavior with clofibric acid and carbamazepine, which are contaminants in an aqueous medium, was considered. The experimental results (Powder-XRD pattern) showed that these two exhibit distinct adsorption behaviors due to structural variations. The result suggests that flexible MOFs are more effective than rigid MOFs in adsorption [120]. This idea tells us that the preparation and development of flexible MOFs can be a suitable candidate for application fields such as separation, catalyst, sensing, and biomedicine compared to rigid MOFs.

1.3.6 Photoinduced dynamics in MOFs with time-resolved spectroscopy

Time-resolved spectroscopy plays an essential role in fundamental and applied chemical research. On-time scales ranging from femtoseconds to microseconds, these techniques can access light-initiated dynamics. As for my research topic, I am interested in observing the photoinduced dynamics of MOF material using femtosecond time-resolved spectroscopy, which will be discussed later. Hence, it will be necessary to know about the photoinduced dynamics of reported MOF systems. The main idea of these studies is to illustrate how light irradiation influences the electronic structure of MOF systems. Several primary research related to exciton transport in the framework via energy transfer, photoinduced dynamics, charge transfer, localization, photoconductivity, and structural dynamics are reported using time-resolved spectroscopy [121]. Some examples for studying MOF properties using time-resolved spectroscopy are discussed here.

1) In the research field of exciton transport via energy transfer, Morris and Lin groups have extensively studied energy transfer in Ru-chromophore doped zirconium(IV)-based metal−organic framework (Zr-MOF), UIO-67 [122,123]. They reported that When Ru-dcbpy (bipyridine dicarboxylate) is used as a linker in UIO-67, an energy transfer pathway takes precedence over a charge transfer pathway. Upon photoexcitation, the Ru-dcbpy structural units of UIO-67 interact with one another and undergo self-quenching via a resonance energy transfer mechanism [124]. Fluorescence quenching was detected using a time-correlated single photon counting approach in which Ru-dcbpy doped UIO-67 was suspended and agitated in DMF before being excited selectively with 510 nm. The energy transfer was impacted by where chromophores are positioned within the MOF. With increasing chromophore dopant concentration, the emission lifetime and maxima size decrease, as shown in Fig. 1.13. Laser photolysis experiments were conducted to measure the performance of Ru-dcbpy-UIO-67 MOF in DMF when excited at 355 nm. The results revealed a difference in emission lifetime

between low loading (20−30 μs) and high loading (100 μs), which can be attributed to energy transfer occurring among the neighboring Ru-dcbpy chromophores within the octahedral cavity of the MOF (Fig. 1.13). This suggests the importance of time-resolved spectroscopy in the field of energy transfer processes in MOFs.

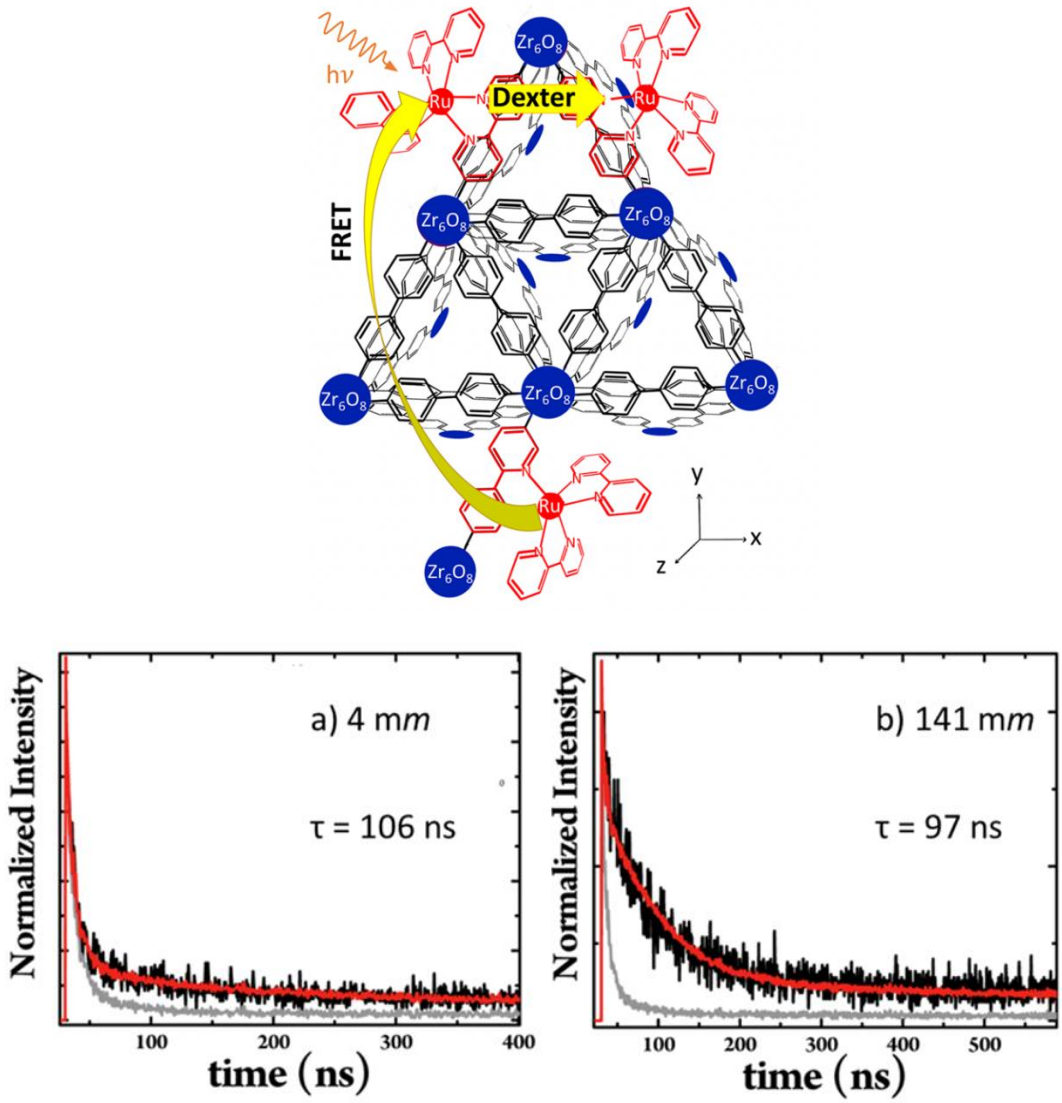

Fig. 1.13: (upper panel) Tris(bipyridine)ruthenium (II) ($Ru(bpy)_3$) incorporated into 3D MOF, (lower panel) Emission lifetime decays (black) of Ru-dcbpy-UIO-67 samples at (a) 4 mm (millimole of Ru-dcbpy per kilogram of MOF) and (b) 141 mm and photoexcited with a pulsed LED at 510 nm and measured by time-correlated single photon counting. Corresponding

exponential fits (red) are done by a deconvolution/convolution of the instrument response function (gray). The deviation from mono-exponential at higher Ru-dcbpy concentration is indicative of two populations of Ru-dcbpy forming. The long-lifetime component of Ru-dcbpy-UIO-67 at both chromophore loadings above was attributed to the Ru-dcbpy incorporated into the backbone of the material. In contrast, the short-lifetime component at high loading was attributed to encapsulated Ru-dcbpy chromophores [124].

2) Photocatalysis is a process in which photons serve as the source of energy, or voltage, to facilitate a chemical reaction. Out of multiple reports, the following example illustrates a comprehensive compilation of MOFs, where time-resolved spectroscopy has contributed to a clearer understanding of their photocatalytic mechanism. Xu and colleagues studied PCN-222, a free-base porphyrin-based MOF containing Zr nodes [125]. Their research demonstrated that this material is effective for photocatalytic CO_2 reduction in acetonitrile, using triethanolamine as a sacrificial electron donor. The photocatalytic efficacy was investigated for PCN-222 (PCN: porous coordination network) using time-resolved spectroscopy with the MOF suspended in DMF (Dimethylformamide). From the time-resolved photoluminescence dynamics (Fig. 1.14(b)), the fs- transient absorption spectrum (Fig. 1.14(c)) and the kinetics of ground state bleach feature (Fig. 1.14(d)) agree with that the observation of long-lived components with a lifetime of >> 1 ns which the authors assign as a non-emissive electron trap state. The trap state is most likely centered on the structure's Zr nodes, which are involved in photocatalytic CO_2 reduction.

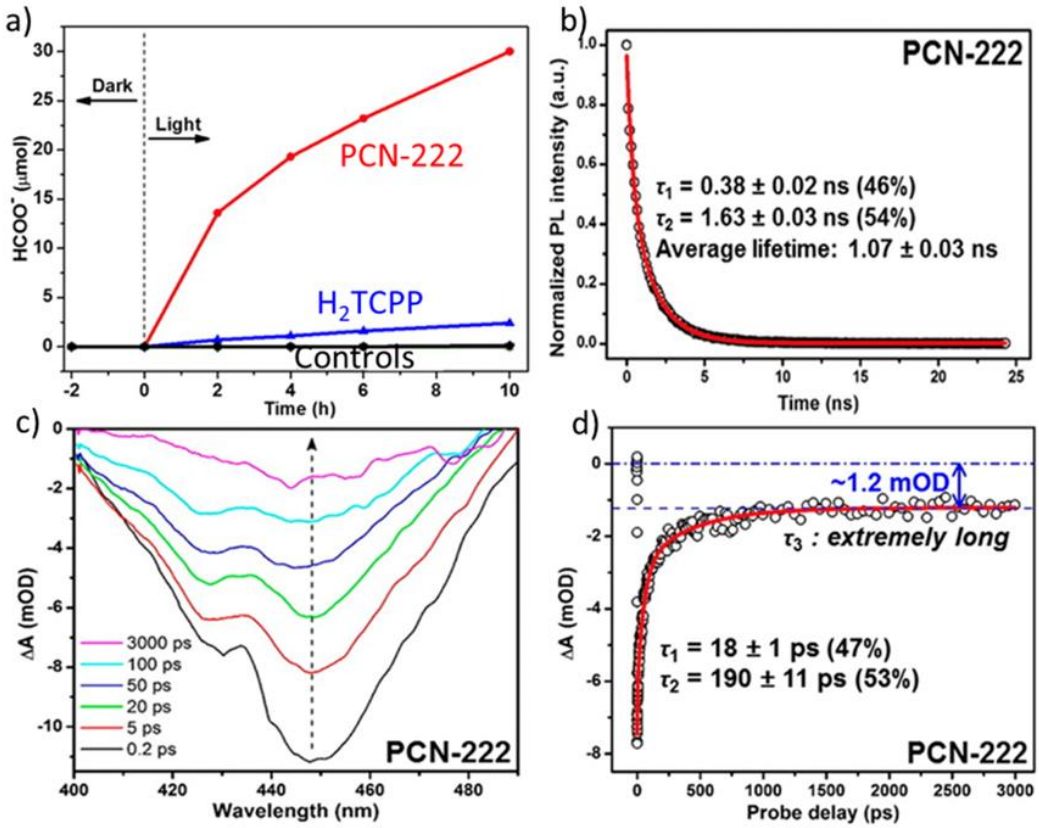

Fig. 1.14: (a) Photocatalytic experiments with PCN-222 MOF or H_2TCPP ligand in ACN/TEOA. Controls excluded either PCN-222, TEOA, or CO_2. (b) Time-resolved photoluminescence of PCN-222 in DMF at 712 nm under 515 nm photoexcitation with biexponential fit. (c) fs-TA spectra of PCN-222 under 500 nm excitation. (d) fs-TA kinetics of the ground-state bleach feature in (c) and triexponential fit [125].

3) The structure of MOF materials can be deformable or altered by thermal fluctuations and external pressure. Thus, another important application of time-resolved techniques is to study the photoinduced dynamics of structural information in MOFs. One example is Nishida et al., who conducted the first time-resolved 2D-IR studies to investigate structural dynamics in the Zr-based UiO-66 MOF.

Indeed, photoexcitation can lead to various fascinating situations, such as simultaneously photoinduced local energy and charge transfer between D and A ions, photoconductive phenomena, and the photothermal effect on relatively slow timescales. Regrettably, ultrafast photocontrol of physical properties based on the cooperative interactions in MOF systems has rarely been reported. Nevertheless, since DA-type MOFs exhibiting CT-type phase transitions have recently become much more popular, some MOFs may be ideal for observing fast photo-responses of the electronic states. This is the main reason for starting the ultrafast dynamics study of MOF research reported in this thesis.

1.4 Motivation of the present study

The research backgrounds and exciting concepts of PIPT in ultrafast timescales always influenced my mind to pursue my research career in the ultrafast science of phase transition. Ultrafast science and its development are also fascinating from an application perspective, such as high-speed memory devices and storage systems, which create high-speed and efficient supercomputers. Meanwhile, CT-type DA systems are usually a molecular material with a low-dimensional, electron-correlated lattice, as defined by anisotropically directed electronic correlations or chemical bonds between the constituent molecules/ions. The low dimensionality of such an electron-correlated lattice may induce several kinds of instability associated with the electrons, lattice, and spin. These are key factors for achieving an efficient photo-response because of the inherently cooperative electron–electron, electron–lattice, and magnetic interactions that are strongly expected. In a general sense, studying the photo response of such systems is important for the application and development of optical functional devices or materials. Due to their inherent complexity, excited states or relaxation dynamics are still unclear, although they provide information essential to understanding switching (and PIPT).

The present study aimed to perform ultrafast photoinduced dynamics for a 2D layered system since no detailed and extensive photophysical study has been achieved yet at ultrafast timescale. Therefore, this study will introduce a new class of photo-switching material to PIPT science and enhance science and technology fundamentals.

We focused/chose a DA-type layered MOF (Metal-organic Framework) system $(NPr_4)_2[Fe_2(Cl_2An)_3]$ (where NPr_4^+ = tetra-*n*-propylammonium and Cl_2An^{2-} = 2,5-dichloro-3,6-dihydroxo-1,4-benzoquinonate) [126] to satisfy our intention. Interestingly, this compound shows a two-step CT-type phase transition, with the steps occurring at 317 K [$T_{1/2(1)}$] and 354 K [$T_{1/2(2)}$]. The driving mechanism for these phase transitions has been discussed from the viewpoint of multi-stability, reflecting the balance between the valence change and the Coulomb interaction, as in an N–I phase-transition system [113, 127] However, a robust framework structure without appreciable lattice deformation—like the dimerization in TTF–CA—even at each $T_{1/2}$ is quite fascinating for investigating ultrafast photoinduced CT-type phase changes.

Chapter 2

2. Target Material: $(NPr_4)_2[Fe_2(Cl_2An)_3]$

Few molecular compounds can alter their charge states multiple times in response to external stimuli. In the present study, I primarily focused on the DA-type layered MOF $(NPr_4)_2[Fe_2(Cl_2An)_3]$ (where NPr_4^+ = tetra-*n*-propylammonium and Cl_2An^{2-} = 2,5-dichloro-3,6-dihydroxo-1,4-benzoquinonate [126], Which shows two-types of phases switching in its own thermally driven electron transfer (TDET) process, and considered to be the first material to exhibit such behavior. During my doctoral course research, I am interested in observing the ultrafast photoinduced response from this material. In this context, the material synthesis, crystallographic structure, and physiochemical properties will be discussed in the following sections.

2.1 Sample preparation

The target material is synthesized in Prof. Miyasaka's Laboratory at Tohoku University. The material is prepared from the pristine solvated compound $(NPr_4)_2[Fe_2(Cl_2An)_3].2(acetone).H2O$. Prof. Miyasaka and coworkers reported the detailed preparation methods for this solvated sample [127]. The single crystal samples of $(NPr_4)_2[Fe_2(Cl_2An)_3].2(acetone).H2O$ were made by slowly diffusing the material in a glass tube with a narrow inner diameter ($\phi = 8$ mm). Water (2 mL) containing $FeCl_2 \cdot 4H_2O$ (7.95 mg, 0.04 mmol), NPr_4Br (42.60 mg, 0.16 mmol) and CH_3COOLi (10.56 mg, 0.04 mmol) was placed in the tube (bottom layer), then a mixture of acetone (0.5 mL) and water (0.5 mL) was carefully placed on the water layer (buffer layer). Finally, acetone (2 mL) of chloranilic acid (12.54 mg, 0.06 mmol) was placed on the top (top layer). After 3 weeks, the black hexagonal prismatic crystals were collected from the mother

liquid at a 37% yield. For the present sample, we synthesized crystals of solvent-free $(NPr_4)_2[Fe_2(Cl_2An)_3]$ by following the method reported in ref. [63]. However, the as-synthesized pristine samples contained some crystallization solvents, such as $(NPr_4)_2[Fe_2(Cl_2An)_3]\cdot 2(acetone)\cdot H_2O$ [127]. We removed these crystallization solvents by evacuating the crystal samples for 12 hours at room temperature to produce the solvent-free compound $(NPr_4)_2[Fe_2(Cl_2An)_3]$.

2.2 Structural overview

Single-crystal X-ray diffraction (SC-XRD) result at 103 K revealed a 2D honeycomb-layered structure similar to previous solvated material, $(NPr_4)_2[Fe_2(Cl_2An)_3].2(acetone).H_2O$. The material crystallized in space group $P2_1/n$ with z =2, half of the formula unit is an asymmetric unit of ($1 \times Fe^{n+}$, $1.5 \times Cl_2An^{m-}$ ($L_A \times 1$, $L_B \times 0.5$), and $1 \times NPr_4^+$; as shown in Fig. 2.1 (a) with two-fold axes through the Fe^{n+} and the midpoint of the L_B Cl_2An^{m-} ligand.

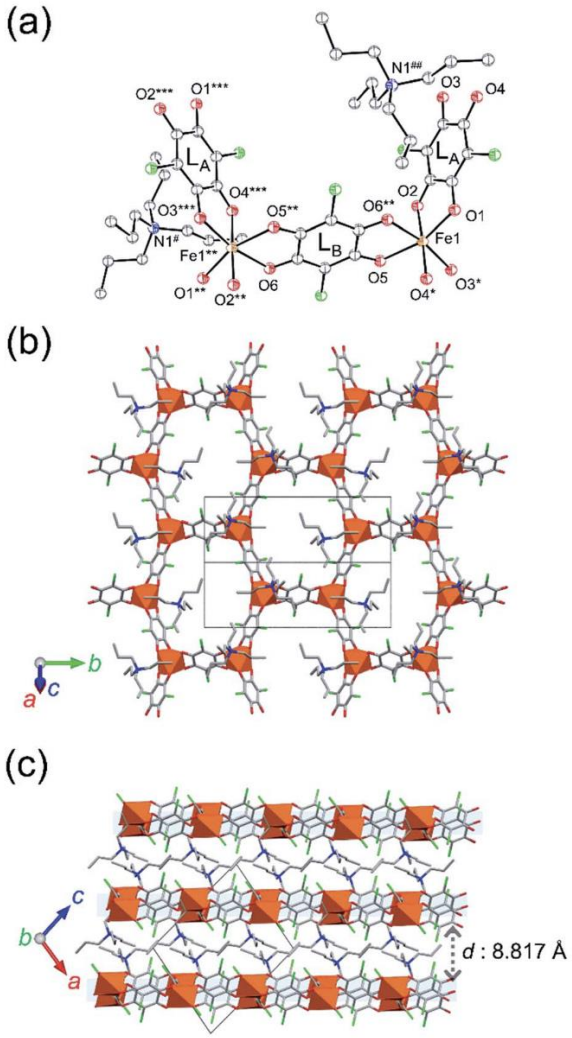

Fig. 2.1: Crystal structure of 1-d at 103 K. (a) Structure of the formula unit $[Fe_2(Cl_2An)_3]$. (b) Projection of hexagonal honeycomb networks along the (10-1) direction, where Fe, C, N, O, and Cl atoms are colored in orange octahedra, grey, blue, red, and green, respectively, and hydrogen atoms are omitted for clarity. (c) Projection of layer structures along the b-axis [126].

For simplicity, here, Fig. 2.2(a) is shown, which represents a schematic illustration of the structure of the 2D honeycomb layer of $[Fe_2(Cl_2An)_3]^{2-}$. The NPr_4^+ cations are placed between the 2D honeycomb layers but omitted from this figure for clarity.

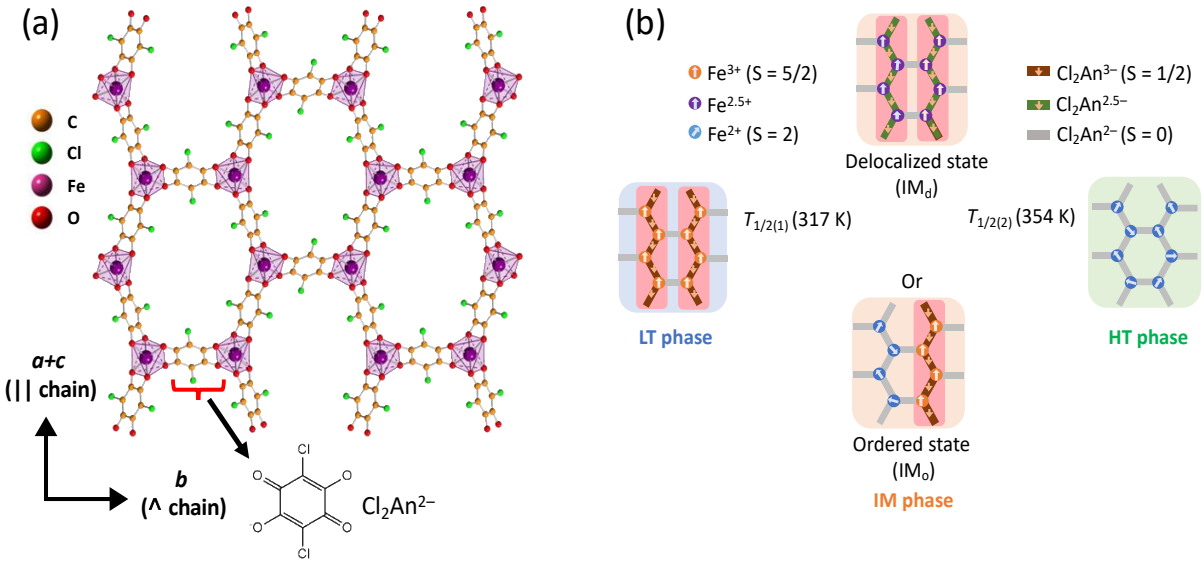

Fig. 2.2: (a) Structure of the D_2A_3-type honeycomb layer in $(NPr_4)_2[Fe_2(Cl_2An)_3]$ (where D = donor and A = acceptor). The portion surrounded by the thick dashed line is schematically illustrated in panel b. (b) Schematic charge and spin patterns in the low-temperature (LT), intermediate-temperature (IM), and high-temperature (HT) phases. Two possibilities are proposed for the IM phase, a delocalized state (IM_d) and an ordered state (IM_o).[126] The Fe ions are depicted as colored circles, and thick colored lines represent the Cl2An ions. The arrows inside the circles and lines represent the spins [128].

2.3 Charge transfer (CT) type phase transition

Interestingly, this compound shows a two-step CT-type phase transition, with the steps occurring at 317 K [$T_{1/2(1)}$] and 354 K [$T_{1/2(2)}$]. The phases distinguished by $T_{1/2(1)}$ and $T_{1/2(2)}$ are named the low-temperature phase (LT phase), an intermediate phase (IM phase), and the high-temperature phase (HT phase) (Fig. 2.2 (b)). The IM phase may take the form of either a charge-disproportionate ordered state (IM_o) or a delocalized state (IM_d), as shown in Fig. 2.2 (b). The charge and spin patterns in the honeycomb layer of each phase have been confirmed by magnetic, structural, and Mössbauer spectroscopic measurements. This suggests the charge distribution of three charge-ordered states are LT phase: $[(Fe^{3+})_2(Cl_2An^{2-})(Cl_2An^{\cdot 3-})_2]^{2-}$; IM phase: $[(Fe^{2.5+})_2(Cl_2An^{2-})(Cl_2An^{2.5-})_2]^{2-}$; and HT phase: $[(Fe^{2+})_2(Cl_2An^{2-})_3]^{2-}$ that varies according to temperature. The temperature dependence of Mm of 1-d was investigated for the HT region of 300–400 K.

From magnetic investigation, the χ_m vs. T curve clearly shows two steps as the temperature is varied, as shown in Fig. 2.3 (left panel). The ^{57}Fe Mössbauer spectra for the respective phases

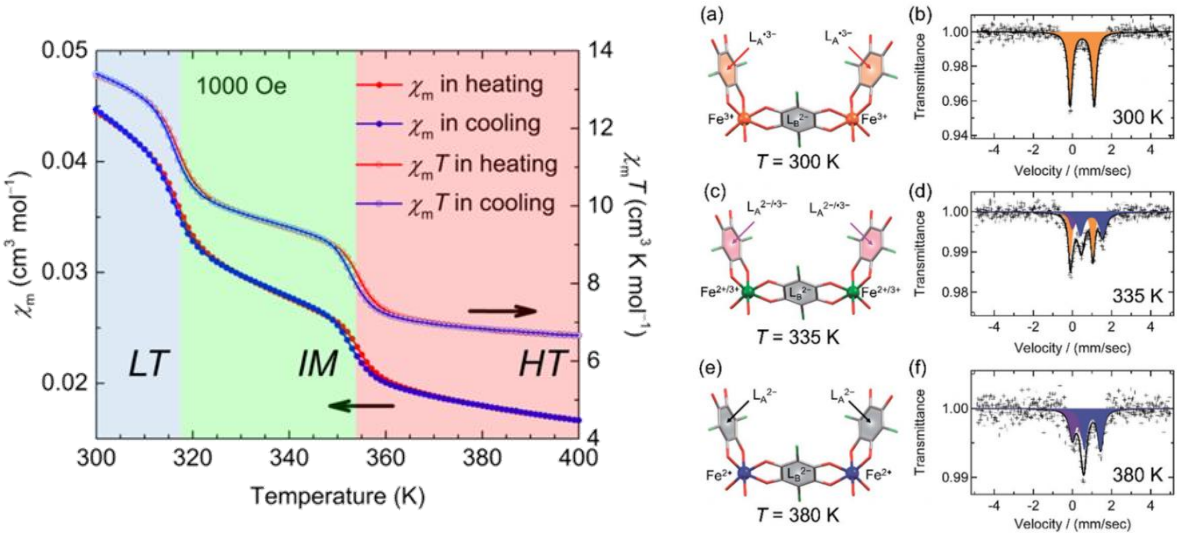

Fig. 2.3: (left figure) Temperature dependence of χ_mT and χ_m for $(NPr_4)_2[Fe_2(Cl_2An)_3]$ measured at H_{dc} = 1 kOe continuously between 300 K and 400 K in initial heating (red) and post-cooling (blue) processes, where the LT, IM, and HT phases are displayed as red, green,

and blue areas, respectively. (Right figure) Charge variations of the core unit and ^{57}Fe Mössbauer spectra of 1-d in LT at 300 K (a and b), IM_o at 335 K (c and d), and HT at 380 K (e and f) [126].

are represented in Fig. 2.4 (right panel). These suggest the two-step phase transition with charge and spin pattern in this material.

Despite its honeycomb layer structure, the charge alignment of the LT phase consists of quasi-1D chains of Fe^{3+} and Cl_2An^{3-} along the a+c direction, which are connected with neighboring chains by the diamagnetic Cl_2An^{2-} (S = 0) ions. Since the Fe^{3+} (S = 5/2) and Cl_2An^{3-} (S = 1/2) ions are antiferromagnetically coupled along the chain, these ferrimagnetic chains are magnetically isolated; this magnetic structure in the LT phase is confirmed to be a single-chain magnet (SCM).[40,41] The IM phase appears upon increasing the temperature above $T_{1/2(1)}$, and the HT phase appears above $T_{1/2(2)}$ (Fig. 2.2 (b)). The IM phase may take the form of either a charge-disproportionate ordered state (IM_o) or a delocalized state (IM_d), with a 1:1 ratio of Fe^{2+} to Fe^{3+} and a 1:1 ratio of Cl_2An^{2-} to Cl_2An^{3-} in the chain. In contrast, the HT phase consists solely of a set of Fe^{2+} and Cl_2An^{2-} ions, i.e., it is a paramagnetic phase. The CT-type phase transition thus corresponds to a phase transition from an SCM-related charge alignment to a paramagnetic charge alignment. The driving mechanism for these phase transitions has been discussed from the viewpoint of multi-stability, reflecting the balance between the valence change and the Coulomb interaction, as in an N–I phase-transition system. However, a robust framework structure without appreciable lattice deformation—like the dimerization in TTF–CA—even at each $T_{1/2}$ is quite fascinating for investigating ultrafast photoinduced CT-type phase changes.

In short, the first half of this chapter represents a brief understanding of MOF systems from structural, physical, and application points of view. Then we discuss the essential information for our target material, $(NPr_4)_2[Fe_2(Cl_2An)_3]$. The present material is the first case of TDET materials to show multiple phases of switching in its own TDET process. The transformation between these accessible states, composed of three distinct charge-ordered states (LT, IMo, and HT), was successfully realized. In this research, we will utilize this material to perform time-resolve measurements in fs-timescale to achieve fast and effective photo-switching.

2.4 Research objective and expected outcomes

As a primary target material for this research, $(NPr_4)_2[Fe_2(Cl_2An)_3]$, a promising material that exhibits a two-step charge-transfer (CT) phase transition (T_c = 317 and 354 K) at which the valence of Fe and Cl_2An changes. It should be noted that there is no apparent structural change at each $T_{c,}$ probably due to the rigid bond nature between Fe and Cl_2An molecules. Therefore, the phase transition of this system can be viewed as purely electronic. Then, an efficient photoinduced CT phase transition can be expected without lattice structural deformation by weak photoexcitation. To make our imagination real, we decided to perform the Photoinduced dynamics in the charge transfer type phase transition system, $(NPr_4)_2[Fe_2(Cl_2An)_3]$, using fs-time-resolved spectroscopy. First, we decided to perform experiments at room temperature (RT), allowing us to excite the LT phase. Then, we will try to excite the system at high temperatures over the $T_{1/2(2)}$: 354 K.

As an expected outcome, we can expect to observe:

1. An efficient photo-induced CT ($Cl_2An^{3-} \rightarrow Fe^{3+}$) can be expected when we excite LT phase.
2. Photo induced reverse CT ($Fe^{2+} \rightarrow Cl_2An^{2-}$) $^{+}$) can be expected when we excite HT phase.

To study PIPT in $(NPr_4)_2[Fe_2(Cl_2An)_3]$, we began our experimental journey with these two specific motivations.

Chapter 3

3. Experimental Methods

The experimental methods we employed to fulfill our research motivation are discussed in this chapter. Initially, we spoke about how to choose a sample for measurements. Next, we demonstrated the main instruments and equipment for detecting static optical spectra. We also discussed the overview of time-resolved pump-probe spectroscopy, which was used to follow the moment-to-moment changes in electronic states upon photoexcitation. Pump-probe spectroscopy is a technique to measure the optical properties (reflectance, transmittance, and polarizability) of a material induced by excitation (pump) light irradiation.

3.1 Sample selection and method of fixation

A single crystal sample of $(NPr_4)_2[Fe_2(Cl_2An)_3]$, which was provided by Prof. Miyasaka's Laboratory at Tohoku University, is used as our target material for this research. The hexagonal shape of the crystals is the most desirable and flawless. Also, clean, shiny surface samples are required to measure reflection from the sample surface precisely. Steady-state optical measurement, especially reflectance measurement, was performed to determine electronic structures quickly and precisely. Unfortunately, most samples are broken, tiny, and have a dull or cracked surface. To use the samples for reflectance measurement,

(1) The crystal size must be sufficiently larger than the measurement light irradiation size of the microscope device used (at least one side is 100 μm or more).

(2) The crystal surface must be smooth and reflective without cracks or chips. The light mustn't be scattered. In addition, since the crystal is fragile and small, it is impossible to polish it to a mirror surface. So, measuring the reflectance using the crystal growth plane is necessary.

(3) To distinguish a good sample, it is necessary that the anisotropy of reflectance due to polarization can be observed and that the spectrum's shape is reproducible.

First, we chose the sample visually using a stereomicroscope, and the picture of some selected samples is shown in Fig. 3.2. We fixed the samples on silver paste and used FT-IR spectroscopy to measure their reflectivity spectrum.

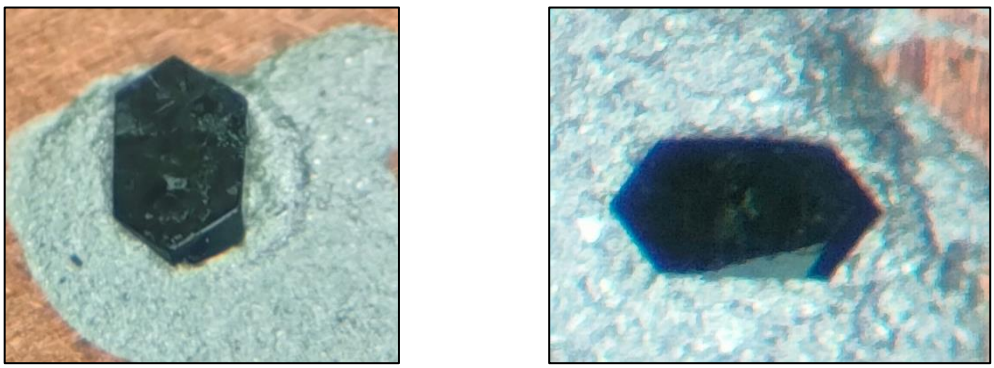

Fig. 3.1: The picture of the samples we choose visually using a stereomicroscope. It shows the hexagonal shape of the single crystal.

The main idea for such experiments is to identify the anisotropy of the samples. We took many crystals, measured them, and then, after confirming that the results were repeatable, we chose the best samples.

The single crystal sample was fixed to a copper plate with silver paste for optical measurements. Fig. 3.2 (right) shows a schematic diagram of how to fix the sample. To perform optical spectrum measurement using linearly polarized light, the relationship between the optical axis direction of the sample and the polarization of measurement light and excitation light is important. Because the crystals are so small, it is difficult to visually determine the orientation of the sample and align it with the direction of polarized light during measurement. Therefore, the sample was first fixed on a small square copper plate (approximately 5 mm × 5 mm) so that the orientation of the sample could be determined visually.

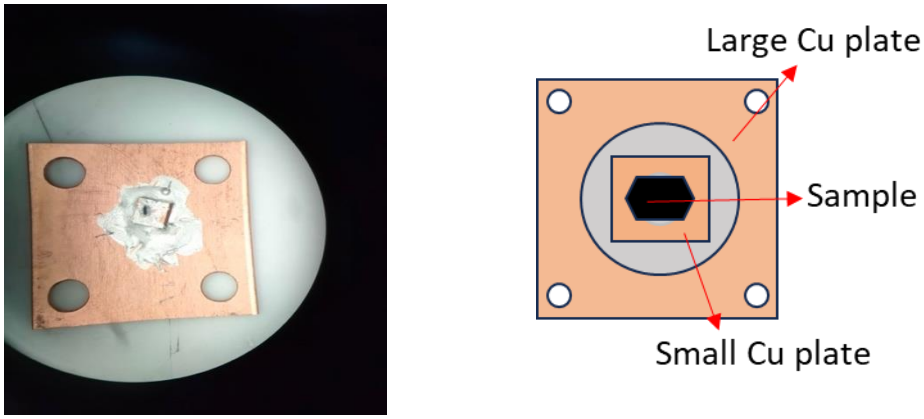

Fig. 3.2: (left)The picture of the selected fixed sample over a large copper plate (20 mm × 20 mm). (right) schematics of the sample fixation process.

Then, the crystal, whose orientation was determined in this way, was fixed together with a small copper plate to a large copper plate (20 mm × 20 mm) (Fig. 3.3) for attaching the sample holder of the cryostat, taking into consideration the polarization direction during measurement. Silver paste and copper plates are used to fix the sample to achieve sufficient thermal equilibrium with the cryostat, whose temperature is controlled by a temperature regulator when measuring temperature dependence, and to align the sample temperature with the temperature of the sample holder. This is because high thermal conductivity is required. In particular, since the measurements were to be conducted at temperatures higher than room temperature, we chose silver paste because it is an adhesive that can withstand high temperatures. These samples were used for static optical spectra and time-resolved pump-probe measurements.

3.2 Determination of crystal anisotropy and optic axis

A detailed description of the actual method of determining crystal anisotropy and optic axis is given in this section. The typical shape of a single crystal sample of $(NPr_4)_2[Fe_2(Cl_2An)_3]$ is a

hexagonal prism. The hexagonal portion of the sample is used for reflectance measurement. The shape of the hexagonal prism corresponds to the microscopic crystal structure shown in Fig. 3.3, which was obtained by X-ray crystal structure analysis. Fig. 3.3 shows the structure of the crystal plane that appears in the hexagonal part, which is a plane containing a two-dimensional network of $Fe_2(Cl_2An)_3$. Therefore, this plane is the most suitable for studying the electronic structure in the two-dimensional network. The solid red line in the figure shows the macroscopic outline of the sample.

The mirror index of each plane is also shown in Fig. 3.3, and the plane used for this measurement has a mirror index of (10-1) or (-101). In other words, this surface contains the b-axis and the direction of the sum of the unit lattice vectors of the a-axis and b-axis. The intersection direction between this plane and the (0-10) (010) plane, which is the side of the hexagonal prism, is the chain direction of the one-dimensional chain magnet that appears in the low-temperature phase described above. As the crystal orientation is shown in the figure, the direction of this one-dimensional chain magnet is orthogonal to the b-axis. Therefore, the suitable direction for measuring the anisotropy of the optical spectrum is the direction of the one-dimensional chain magnet and the b-axis are orthogonal to the one-dimensional chain magnet.

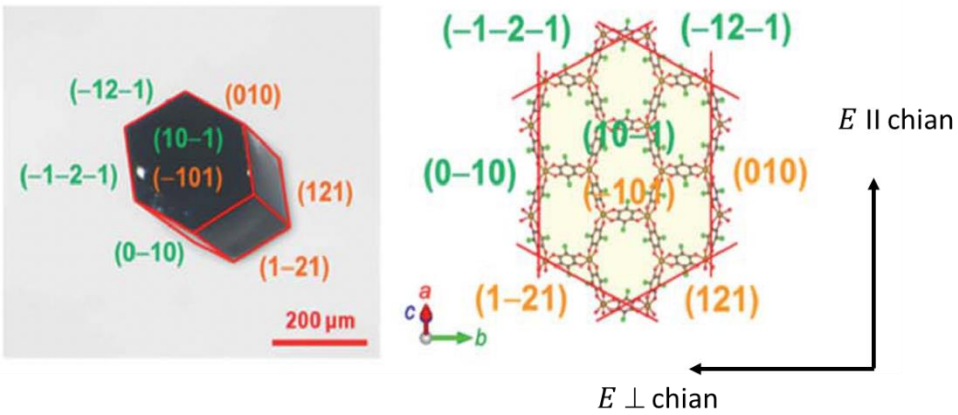

Fig. 3.3: $(NPr_4)_2[Fe_2(Cl_2An)_3]$ Microstructure outline and Miller index of the crystal growth

plane used for the reflectance measurement of crystal. The macroscopic crystal outline reflects this microstructure and is shown by the red line in the figure [126].

The measurement plane is hexagonal. The four crystal structures (1-21), (-12-1), (121), and (-1-2-1) planes, and the two planes (0-10) and (010) are equivalent to each other. On the other hand, the (10-1) plane, the hexagonal plane, has three different edges in three different directions. Therefore, when linearly polarized light is applied parallel to the direction of the sides of the hexagonal plane and the spectrum is measured in three directions, optical anisotropy should be observed in the two directions of intersection between the (1-21), (-12-1), (121), and (-1-2-1) planes and in one direction of intersection between the (0-10) and (010) planes.

It gives the idea that the axis that will show a different reflectance spectrum from the other two axes is the chain direction of the one-dimensional chain magnet. In Fig. 3.3, if we use the direction of an electric field, E, and denote it as $E \parallel \mathrm{chain}$ or same as $E \perp \mathrm{b}$.

Here, it should be noted that when the solvent remains in the crystal of this sample, the phase transition temperature decreases significantly, and a low-temperature phase does not appear at room temperature but an intermediate phase in which the one-dimensional magnetic chains disappear [9]. Therefore, before all measurements were performed in this study, we first measured and evaluated the infrared spectra of the crystals used for confirmation. Crystals with small spectral anisotropy were found to be due to poor crystallinity of the sample or the presence of solvents. Since it remained in the sample, it was not used because it did not have a low-temperature phase at room temperature, and only crystals with remarkable anisotropy were selected and used for optical measurements.

3.3 Static reflectivity spectra measurement

3.3.1 The principle and types of reflection of light

For solid-state material, a sample's reflectance is determined by shining light on it and measuring the light reflected. There are two types of reflected light: specular reflected light and diffuse reflected light, referred to as the total reflected light when combined (specular reflected light plus diffuse reflected light). A diagram of all types of light is shown in Fig. 3.4. An incident light shines on a sample, and an angle formed between it and the sample is an incidence angle (θ). The incident angle for our reflectance spectra measurements is assumed to be close to zero as shown in Fig. 3.4.

Relative or absolute reflectance is measured in reflectance measurements. Relative reflectance measurements determine how much light is reflected from a sample surface concerning how much light is reflected from a reference plate, such as a mirror or barium sulfate. We assume the reference plate has a 100% reflectance to determine the relative reflectance.

$$\text{Relative reflectance (\%)} = \frac{\text{Amount of Light Reflected from the sample}}{\text{Amount of Light Reflected from the reference plate}} \times 100$$

Instead of utilizing a reference plate-like barium sulfate or a mirror, absolute reflectance measurements determine the proportionate quantity of reflected light compared to the amount of light measured directly from a light source.

$$\text{Absolute reflectance (\%)} = \frac{\text{Amount of Light Reflected from the sample}}{\text{Amount of Light used}} \times 100$$

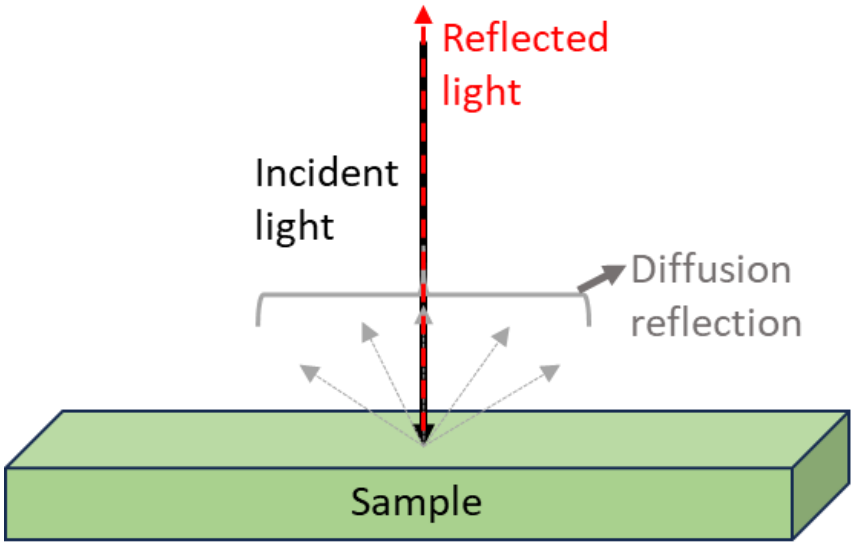

Fig. 3.4: The illustration of different types of reflection phenomena from sample.

Here, we measured the relative reflectance of our target material using a gold (Au) mirror as a reference. The sample preparation and experimental procedure are discussed below.

3.3.2 Instruments used for static reflectivity measurements

We measured static optical-reflectivity spectra of our sample, $(NPr_4)_2[Fe_2(Cl_2An)_3]$, using a commercial Fourier-type infrared (FT-IR) spectrometer (Thermo 6700) with a Cassegrain microscope for the mid-IR range (0.08–1.0 eV). We measured the reflectivity spectra in the near-IR to the visible range (0.9–3.0 eV) using a homemade microscope-spectroscopy system with a diffraction-type monochromator (Bunkokeiki M25) and adequate photodiode detectors. We measured the temperature-dependent static reflectivity spectra using a commercial cryostat with BaF_2 or quartz windows, Microstat He (Oxford Instrument).

3.4 Raman spectra measurement

3.4.1 Principle of Raman spectroscopy

The Raman Spectroscopy technique is a non-destructive method for analyzing the chemical structure of a sample that provides detailed information about the sample's phase and polymorphism, crystallinity, and molecular interactions. An interaction between light and chemical bonds within a material is the basis of this process. Raman spectra show Raman scattered light's intensity and wavelength position through a number of peaks. It shows the vibration of molecular bonds and their various modes, such as C-C, C=C, N-O, and C-H, and the breathing mode of the benzene ring (for example), polymer chain vibrations, or lattice vibrations.

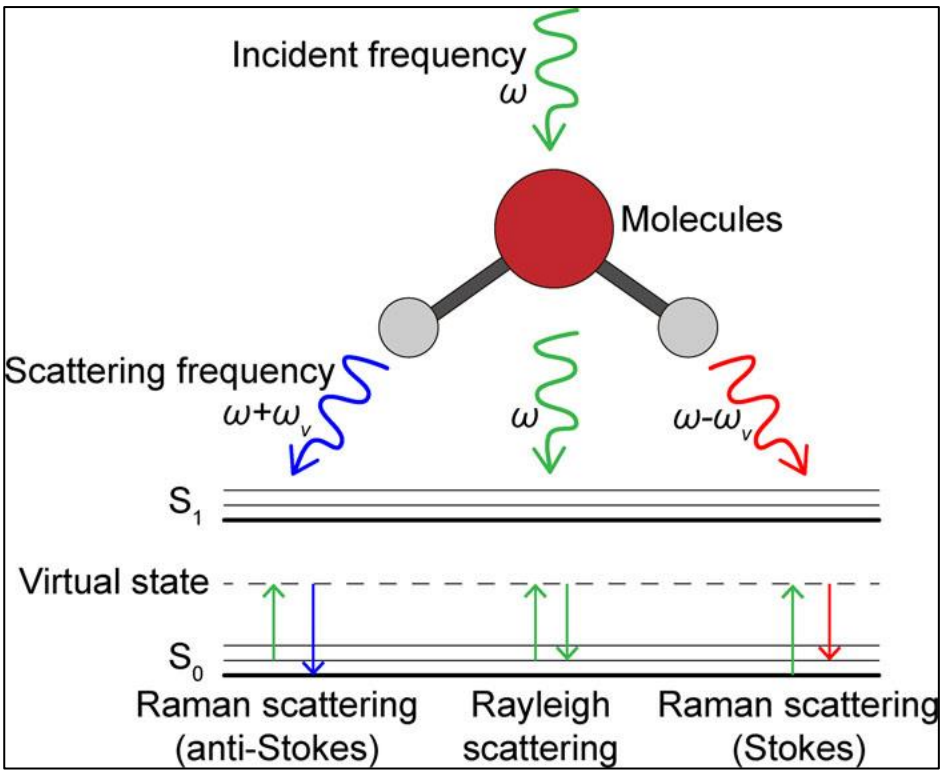

Fig. 3.5: Scheme and Jablonski diagram illustrating Raman scattering and Rayleigh scattering [129].

The inelastic component of light scattering produced when incoming light interacts with molecules is known as Raman spectroscopy. It can be separated from Rayleigh-type elastic scattering as shown in Fig. 3.5. The energy intake or give-off produced by the photon's contact with molecules is represented by the changing frequency between incident (ω) and scattered photons (ω_{υ}) in Raman scattering. The molecules' internal energy is modified due to these interactions (usually due to vibrational transitions). When it comes to photon energy loss during the scattering process, the red-shifted frequency ($\omega - \omega_{\upsilon}$) is described as the Stokes shift, whereas the blue-shifted frequency ($\omega + \omega_{\upsilon}$) is characterized as the anti-Stokes shift and correlates to a photon energy gain. Because most molecules at ambient temperature are in the ground electronic and vibrational states, the Stokes shift often dominates Raman scattering.

3.4.2 Instrument used for Raman spectra measurement

We measured the Raman spectra using a JASCO NRS-4500. To perform the experiment, the single-crystal sample, $(NPr_4)_2[Fe_2(Cl_2An)_3]$, was placed on a copper plate, and a film heater under it controlled its temperature. The sample was irradiated with a 532 nm Raman excitation laser. We measured the Raman spectra with the polarization directions of the analyzer oriented in the x- and y-directions of the incident and scattered light.

3.5 Ultrafast time-resolved spectroscopy

3.5.1 Background: Overview of the timescale for various molecular processes

To fully understand any physical or chemical process during phase transition, it is essential that we observe not only the static states but also the evolution of intermediate structures along reaction coordinates. However, due to the generic timescale of molecular processes, it is difficult to trap and identify the dynamical processes during phase transitions (for example, PIPT). Fig. 3.6 shows an overview of the timescales for various molecular processes. Now, the primary focus of our study is on the lattice-phono interaction, charge transfer, structural modulations, atomic configuration changes that underlie bond creation and breaking, etc., all of which take place between 10^{-9} (nanosecond) and 10^{-15} s (femtosecond) time scales. Thus, capturing those dynamic processes seems extremely difficult and even impossible in normal circumstances. The advent of femtosecond laser systems and ultrafast optical spectroscopy has made it easier to capture these dynamical processes.

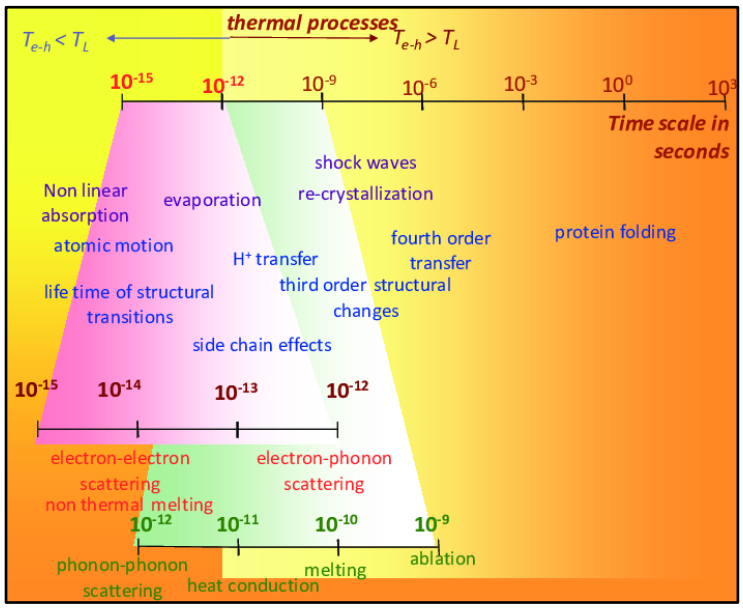

Fig. 3.6: Typical time scales for structural and electronic processes in solids [130].

3.5.2 Time-resolved pump-probe spectroscopy

Pump-probe spectroscopy is the most useful and widely used experimental method for research and development in ultrafast science. This method involves splitting an ultrashort laser pulse into two beams: a weaker beam (probe) is used to track changes in the sample's optical constants (like transmission or reflectivity) caused by the pump, and a more robust beam (pump) is used to excite the material and create a non-equilibrium state. Information regarding the relaxation of electronic states in the sample may be obtained by measuring the changes in the optical constants as a function of the time delay ($\Delta\tau$) between the arrival of the pump and probe pulses. Fig. 3.7 shows the schematic representation of pump-probe spectroscopy.

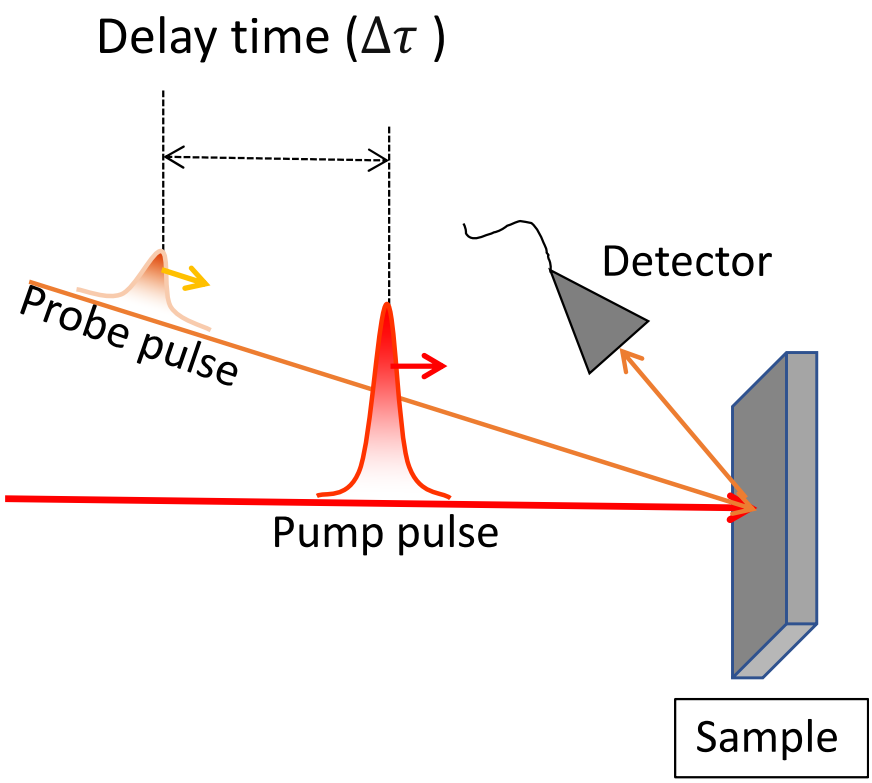

Fig. 3.7: Schematic diagram of reflection pump-probe spectroscopy.

This study performed time-resolved spectroscopy reflectivity measurements using the following two types of light sources.

i) Wavelength-tunable 90 fs pulse in the wide energy range (0.1 – 3.0 eV)

ii) A near-infrared 6 fs ultrashort pulse with a central wavelength of 1.7 μm that lasts only 1.3 cycles of electric field oscillation.

3.5.2.1 Optical setup for pump-probe spectroscopy with 90 fs pulse

Optical path for intramolecular transition and CT energy range: We measured the transient reflectivity change ($\Delta R/R$) using a pump–probe technique. We used a Ti: sapphire regenerative amplifier system (center wavelength, 792 nm; pulse width, 90 fs; repetition rate, 1 kHz; Spectra-Physics Solstice Ace) as the light source. We divided the optical-pulse output from the amplifier system into pump and probe pulses using a beam-splitter plate. The pump pulse delivered from the optical parametric amplifier (OPA: Light conversion, TOPAS) was either 0.73 or 0.8 eV, and we tuned the repetition rate to half of the fundamental frequency (500 Hz) using an optical chopper (New focus 3501). Using frequency-mixing processes, we converted the probe pulse into the 0.4–3.0 eV energy range to cover intramolecular transition and CT energy range of our target material, $(NPr_4)_2[Fe_2(Cl_2An)_3]$. Here, we used the OPA either in the range 0.5–0.7 eV (idler light) or the range 0.8–1.0 eV (signal light). We employed second-harmonic generation of the idler light in the range 1.1–1.5 eV, signal light in the range 1.6–2.1 eV, and fourth-harmonic generation of the idler light in the range 2.2–3.0 eV. The average widths of the pump and probe pulses depend on their energies; a typical probe-pulse width was 150 fs.

The schematic representation of the almost realistic pump-probe setup which we used in our laboratory to measure photoinduced reflectivity change ($\Delta R/R$) is shown in Fig. 3.8. Here, the output of the source pulsed laser is divided into two parts and enters into the OPA 1 and OPA 2. For our case, we use the OPA 2 as a pump (a fixed photon energies of 0.7 and 0.8 eV) that

passes through a chopper, to tune the repetition rate to half of the fundamental frequency, followed by a delay stage to hit the sample. At the same time, the probe light comes out from OPA 1, for several probe photon energies within the range from 0.4 – 3.0 eV, hits the sample. Then, the reflected light (pump-probe response) was detected by detectors. By using the translational stage, we can measure time–resolved data. The results for this measurement are discussed in detail in chapter 5.

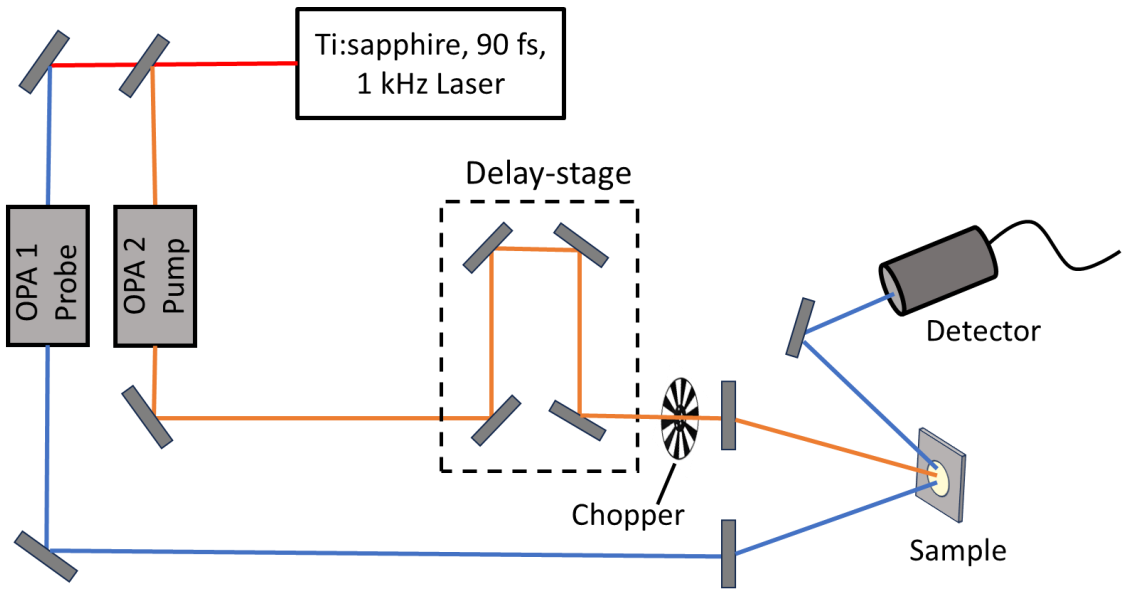

Fig. 3.8: Optical setup for reflection/transmission pump-probe spectroscopy using 90 fs pulses.

Experimental and optical setup for mid-IR energy range

The measurement in mid-IR range has been performed in two different ways:

1. **Low energy resolved spectra (rough scan):** For measurement in the low energy resolved spectra (photoinduced $\Delta R/R$ spectra) in mid-IR range (0.1- 0.4 eV) we employed the same optical set up as like in CT and intramolecular transition energy range. During this measurement the wavelength resolution is about 150 cm^{-1}. The results for this measurement are discussed in chapter 5.

2. **High energy resolved spectra (precise scan):** Here, we measured the $\Delta R/R$ spectra much more precisely to obtain better insight into the spectral nature of the photoinduced state in this range. The optical setup we used for the measurement in the mid-IR range is bit different from the measurement during measuring low energy resolved spectra. The schematic optical set is shown in Fig. 3.9. To measure time-resolved mid-IR $\Delta R/R$ (1200–2000 cm^{-1}), we detected the probe light reflected from the sample using the MCT detectors after passing it through a monochromator (Bunkokeiki M10, the only difference from our previously described setup) to obtain high-energy-resolution spectra with a wavelength resolution of ~6 cm^{-1}, so that the intramolecular vibration modes can be distinguished, even at the expense of a temporal resolution degraded to the order of 1 ps. For the measurement We employed differential frequency generation (DFG) between the signal and idler light in the range 0.12–0.4 eV, which comes out from OPA 1 and used as a probe and the OPA 2 (specific photon energy of 0.8 eV) as a pump that passes through a chopper followed by a delay stage to hit the sample. Now, to measure a wide energy range of mid-IR $\Delta R/R$ (1200–2000 cm^{-1}) spectra, we first select a specific probe energy in DFG energy range (0.1 – 0.4 eV) and measure the broad band pump-probe response from the sample using the monochromator. Then we repeated the same method as discussed above by only changing probe energies to cover such a wide energy range of photoinduced $\Delta R/R$ spectra.

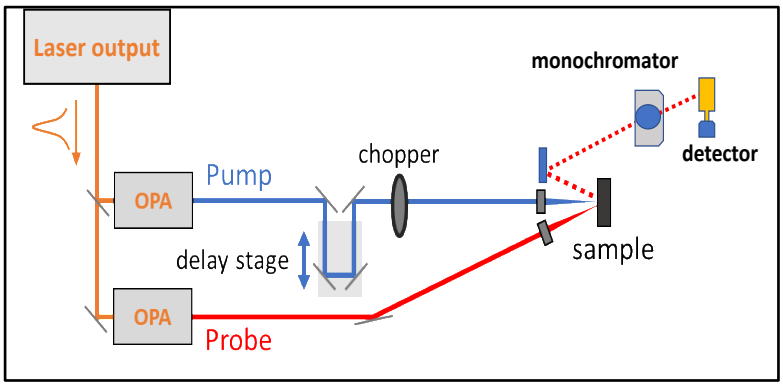

Fig. 3.9: Optical setup for reflection pump-probe measurement in mid-IR energy range.

Detection of pump-probe signal: We measured $\Delta R/R$ using MCT (HgCdTe) (0.1–0.5 eV), InGaAs (0.51–1.1 eV), Si (1.1–2.5 eV), and GaP (2.5–3.0 eV) detectors in the photon-energy ranges of the probe light. We collected the signals from the detectors using a gated integrator (Stanford research, SR250) and an analog-to-digital converter (NI, NI-6143), which we synchronized with the frequencies of the optical chopper and the Ti: sapphire regenerative amplifier. The samples were maintained at RT, with both pump and probe pulses entering the sample at near-normal incidence. To measure time-resolved mid-IR $\Delta R/R$ (1200–2000 cm^{-1}), we detected the probe light reflected from the sample using the MCT detectors after passing it through a monochromator (Bunkokeiki M10). The energy resolution of this system was approximately 6 cm^{-1}.

The raw signal detected is the reflection/transmission intensity of the probe light. The conversion from the detected signal to reflectance change (ΔR/R) is performed as follows. Let R and R' denote the reflectance without and with excitation light, respectively. Then,

$$R = \frac{I_R}{I_0}$$

$$R' = R + \Delta R = \frac{I'_R}{I_0}$$

where I_0 represents the intensity of the incoming probe light, and I_R and I'_R are the reflected intensity of the probe light without and with excitation light, respectively. The change in reflectance ΔR due to photoexcitation is expressed by the following equation.

$$\Delta R = R' - R = \frac{I'_R - I_R}{I_0} = \frac{\Delta I_R}{I_0}$$

Hence, as a whole from the above equations, we can write the value of relative reflectivity change ($\Delta R/R$) as,

$$\frac{\Delta R}{R} = \frac{\frac{\Delta I_R}{I_0}}{\frac{I_R}{I_0}} = \frac{\Delta I_R}{I_R}$$

The excitation light is irradiated to the sample at 500 Hz and thinned by a chopper synchronized with the trigger signal from the regenerative amplifier's Pockels driver. Since the probe light is irradiated to the sample at 1 kHz, the detected intensity of the probe light is I'_R, I_R, I'_R, I_R ⋯. From here, the operation (I'_R - I_R)/I_R is performed in PC and converted to $\Delta R/R$. By recording this $\Delta R/R$ value together with τ_d obtained from the position information of the automatic translation stage controlled by the PC, $\Delta R/R(\tau_d)$ is obtained. Here, the determination of whether the detected probe light is I_R or I'_R is made by detecting a portion of the excitation light pulse after it is thinned by the chopper. The schematic representations for detecting and measuring relative change in reflectance are shown in Fig. 3.10.

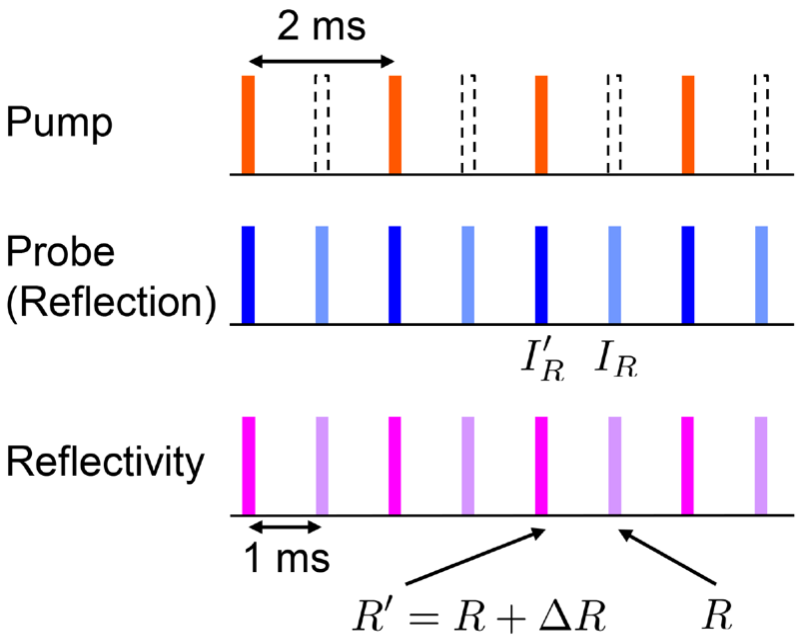

Fig. 3.10: Schematic diagram of detection signal processing in pump-probe spectroscopy using 90 fs pulse.

3.5.2.2 Near-infrared 6 fs pulse generation method and optical setup

6 fs pulse generation method

The time waveform and spectrum of an optical pulse are related to each other by a Fourier transform, and an uncertainty relation ($\Delta t \cdot \Delta\omega \geq K$, where K is a constant that depends on the pulse shape) holds for pulse width (Δt) and spectrum width ($\Delta\omega$ ω). Therefore, it is essential (a necessary condition) that the spectrum be broadband ($\Delta\omega$ is large) to generate extremely short pulses on the time axis (Δt is small). The generation of near-infrared 6 fs ultrashort pulses is performed by the following procedure [126].

(a) Generation of a broadband pulse in the near-infrared region (broadening of the spectrum)

(b) Compression of the broadband pulse (correction of the group delay time)

Figure 3.11 shows the optical system for generating the near-infrared 6 fs pulse. In (a), surrounded by the blue dotted line, the spectrum is broadband; in (b), surrounded by the green dotted line, the spectrum is compressed.

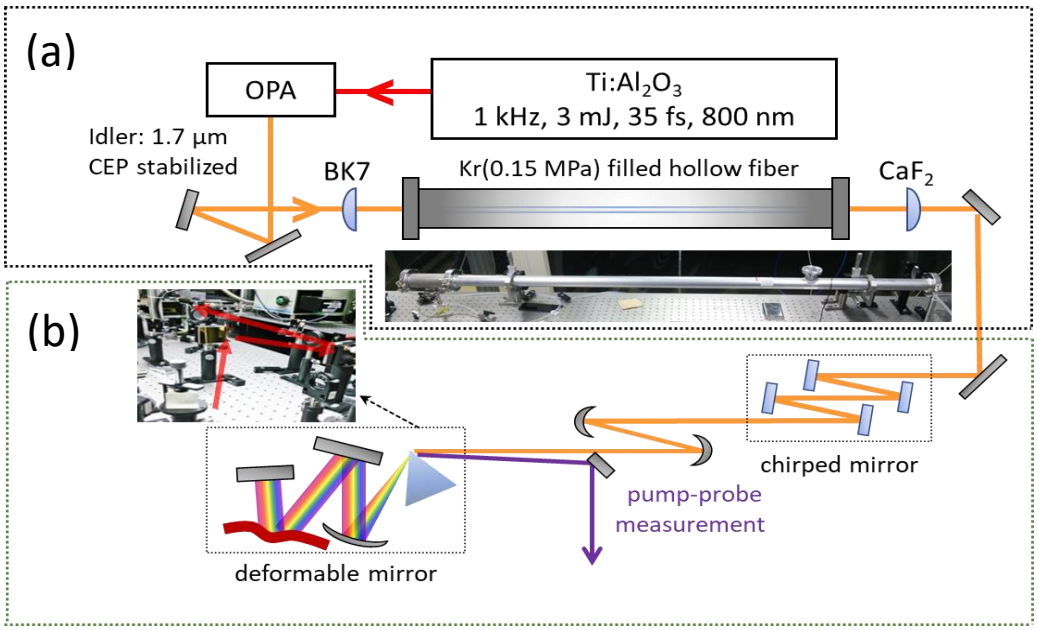

Fig. 3.11: Schematic and photograph of the optical system for 6 fs pulse generation: (a) broadening of the spectrum, (b) pulse compression technique [131, 132].

The details of the 6-fs pulse generation technique and method are reported in Ref [131]

Measurement of pulse width by autocorrelation method

Figure 3.11 shows the autocorrelation (AC) waveforms of (a) the idler light immediately after OPA emission and (b) the light pulse after pulse compression. The autocorrelation waveform was measured by splitting the optical pulse into two, adding a delay time τ to one of them, and observing the second harmonic generated by superposition on a β-BBO crystal (thickness of 10 μm). The intensity waveform of the optical pulse, I, was measured with the full width at half maximum (pulse width) as Δt:

$$I(t) = I_0 \exp\left[-4\, ln\, 2\left(\frac{t}{\Delta t}\right)\right]$$

Assume a Gaussian function like. The autocorrelation waveform G_2 is expressed as a function of delay time τ

$$G_2(\tau) = \int_{-\infty}^{\infty} I(t)\, I(t-\tau) dt$$

The full width at half maximum $\Delta\tau$ of $G_2(\tau)$ is $\sqrt{2}$ times the pulse width Δt of the original optical pulse. From this relationship, the pulse width $\Delta\tau$ of the optical pulse can be estimated

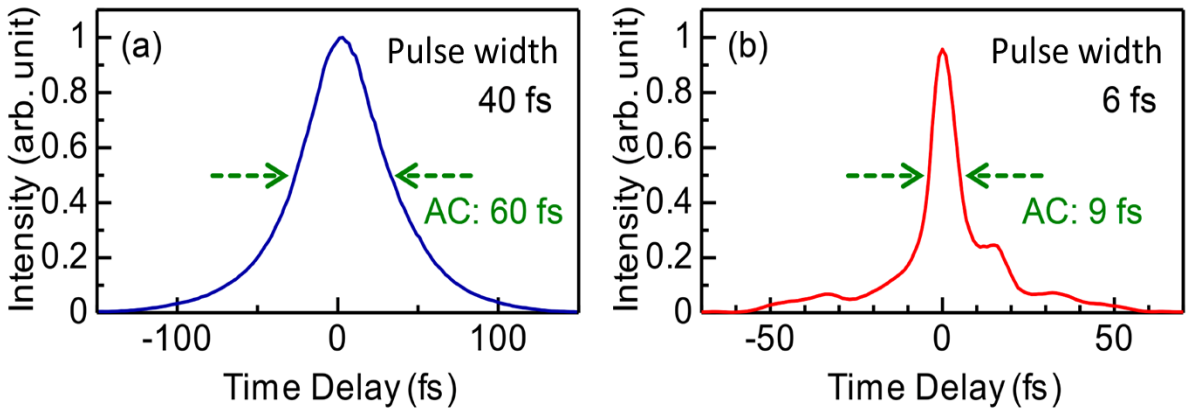

Fig. 3.12: Autocorrelation waveforms of (a) idler light immediately after OPA output and (b) optical pulse after pulse compression.

by measuring the autocorrelation waveform. The autocorrelation waveform Fig. 3.12(a) of the idler light immediately after OPA emission was $\Delta\tau \sim 60$ fs, but the autocorrelation waveform after pulse compression was $\Delta\tau = 9$ fs (Fig. 3.12(b)). From this, it can be confirmed that the pulse width Δt of the optical pulse after compression is 6 fs.

Optical setup of pump-probe spectroscopy with 6 fs pulse

Fig. 3.13 shows the optics of reflective pump-probe spectroscopy using a 6-fs pulse. After afterpulse compression using a chirped mirror and a shape-variable mirror as described in the previous section, the pulse is divided into excitation (red line) and probe (blue line) beams using a 2-μm-thick pellicle beam splitter (BP145B3 from Thorlabs) to avoid pulse stretching due to transmission through a dispersive medium. The excitation light is modulated by a chopper operating at 500 Hz and then given a delay time by a translation auto stage (KST(GS)-50X from Sigma Koki). The light intensity and polarization are then controlled by a wire-grid polarizer pair (see below for details), and the light is focused onto the sample in the cryostat by a 90° off-axis parabolic mirror ($f = 200$ mm). The window material of the cryostat is a 0.4-

10 μm broadband, transparent BaF_2 crystal (3 mm thick). As with the excitation light, the probe light is focused onto the sample by a 90° off-axis parabolic mirror (f = 200 mm) after controlling the light intensity and polarization with a wire grid polarizer pair. The light reflected from the sample is collimated by a lens and detected by an InGaAs detector (New Focus Model 2034) through a monochromator (Spectrometer M10). The detected signal is integrated by a Boxcar integrator (Stanford Research Systems Model SR250) and collected by a PC via an AD converter (National Instruments PCI-6036).

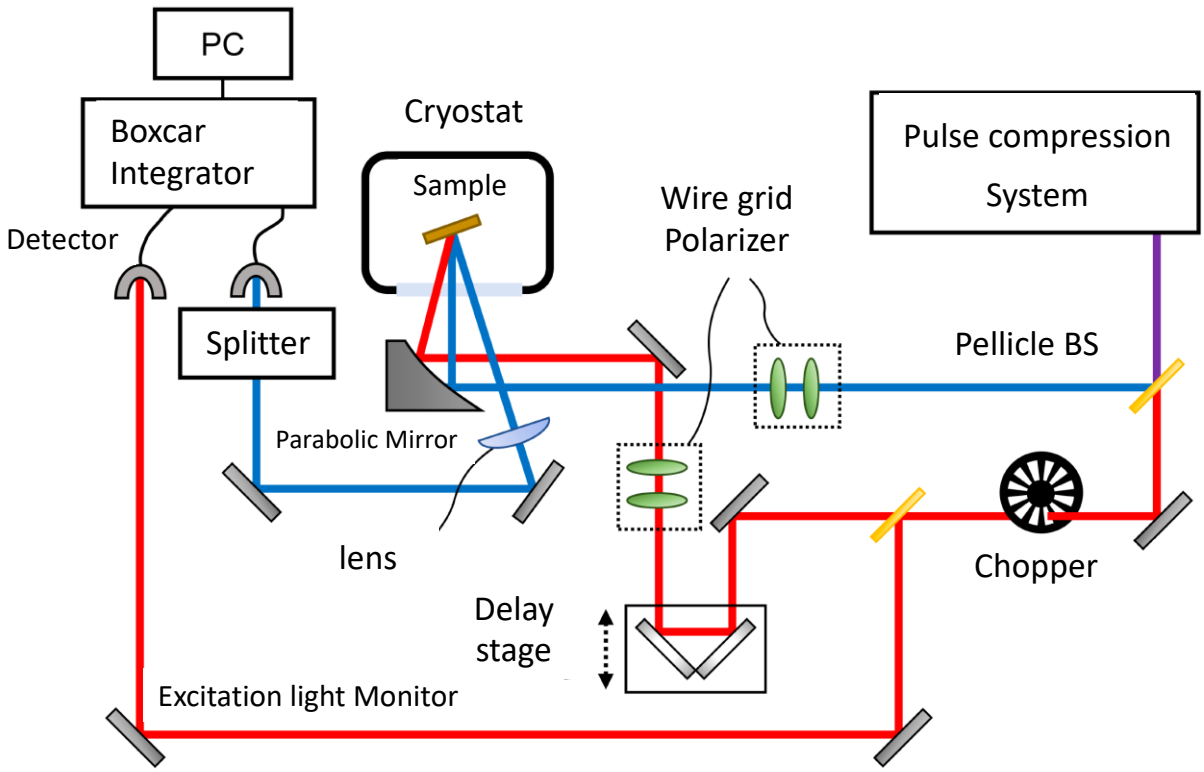

Fig. 3.13: Optical setup for reflection pump-probe spectroscopy with 6 fs pulse

Chapter 4

4. Static Optical spectra of a single crystal of $(NPr_4)_2[Fe_2(Cl_2An)_3]$

In this chapter, we described the results of static optical spectra measurements for our target material, $(NPr_4)_2[Fe_2(Cl_2An)_3]$. The topics of this chapter include the results of anisotropic reflectivity spectra measurement. Also, we reported the results of temperature-dependent reflectivity, optical conductivity, and Raman spectra measurements for both E ∥ chain and $E \perp$ chain directions.

4.1 Objective and Motivation of this experiment

In this research topic, our main target is to observe the photo-response from our target material DA-type MOF system, $(NPr_4)_2[Fe_2(Cl_2An)_3]$. For DA-type systems, a charge-transfer (CT)-type transition—which has the lowest energy of photoexcitation in the electron transfer process—can be an efficient mechanism for controlling electron/spin functionality. Hence, before performing the time-resolved experiment, we need to understand/know the energy gap of CT transition between D and A in our system, the nature of intramolecular vibration peaks (which are considered sensitive towards charge transfer), intramolecular transitions, etc. Here, the purpose of this work is to find an answer to the above requirements.

Hence, we decided to measure static reflectivity and Raman spectra. In Chapter 3, we discuss the details of the experimental methods and the necessary instruments used for these experiments. The results will be discussed in this chapter.

4.2 Result and Discussion

4.2.1 Steady State Reflectivity spectra: Determination of crystal anisotropy and optic axis

Fig. 4.1(a) shows the picture of the sample crystal used for reflectivity measurement (for example, we selected visually using a stereomicroscope). Here, we can observe three visible planes in the hexagonal single crystal. We performed reflectivity measurements in three directions of our chosen hexagonal crystal to determine the proper direction of a one-dimensional chain magnet.

Here, we measured the sample's reflectivity using linearly polarized light in the mid-IR range (0.08–1.0 eV) parallel to the A, B, and C axes, as shown in the image for the sample at RT. The result of the measurement in the range (1000 – 2000 cm^{-1}) suggests that the spectra for $E \parallel$ A and C (electric field direction is denoted as E) are similar results, whereas the spectrum along $E \parallel$ B is different, as shown in Fig 4.1 (b).

From our expectation, as discussed in Chapter 3 (section 3.2), we indeed observed a clear and distinguishable reflectivity spectrum for the different directions of the single crystal for the chosen sample. Hence, we can say that $E \parallel$ A and C must be $E \perp$ chain or $E \parallel$ b axis direction. Whereas $E \parallel$ B must be along the E $\parallel$ chain or $E \perp$ b axis of the crystal. A large anisotropic result can be observed. It suggests we can successfully determine the optic axis and the chain direction of the one-dimensional chain magnet by reflectivity measurements. In other word words, we can be able to distinguish the direction of the $E \parallel$ chain and $E \perp$ chain in the single crystal by optical reflectivity measurement.

Fig. 4.1 (c) and (d) show the reflectivity spectra for the $E \parallel$ chain and $E \perp$ chain in the single crystal in the range of 1000 – 2000 cm^{-1} and 1000 – 9000 $cm^{-1,}$ respectively.

To successfully control the material properties of $(NPr_4)_2[Fe_2(Cl_2An)_3]$ by light, we must select a sample with large anisotropy like the demonstrated sample.

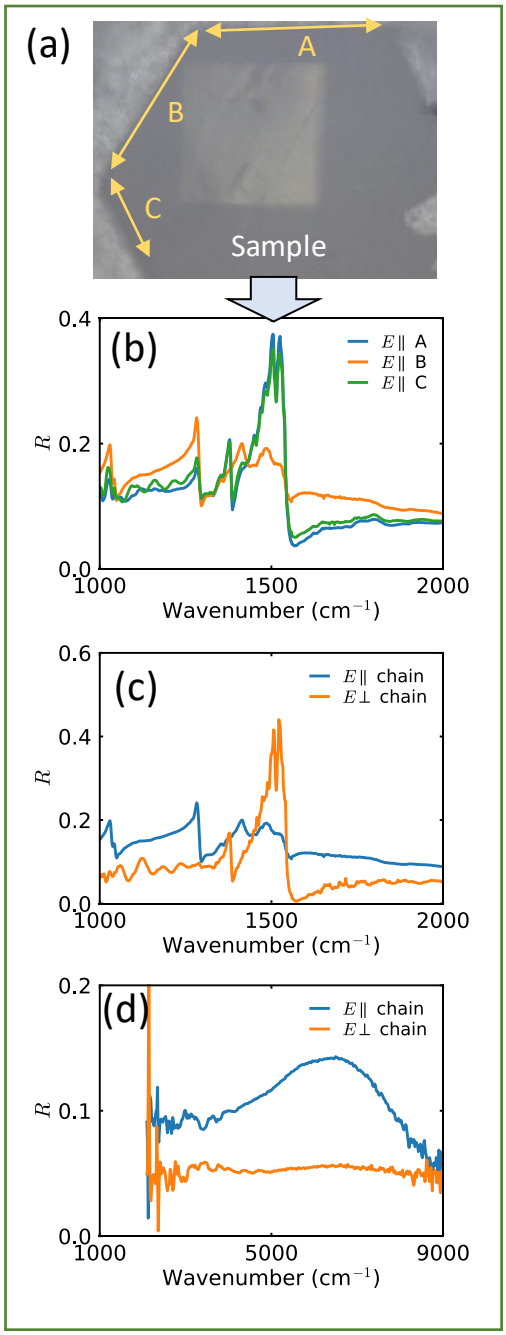

Fig. 4.1: Crystal with pronounced spectral anisotropy (a) picture of the single crystal of the selected sample. The silver area is the silver paste used to fix the sample. The bright square in the center indicates the measurement range of infrared micro-spectroscopy. (b) IR reflectivity spectra measured with polarizations parallel to the A, B, and C axes of (a). (c) and (d) Anisotropy spectra between E ∥ chain and E ⊥ chain direction in the range of 1000 – 2000 cm^{-1} and 1000 – 9000 cm$^{-1,}$ respectively.

4.2.2 Anisotropy of optical spectra at room temperature (RT)

Anisotropy of reflectance spectra at RT

We obtained anisotropic reflectivity spectra of a single crystal of $(NPr_4)_2[Fe_2(Cl_2An)_3]$ at RT (LT phase) using linearly polarized light in a wide energy range (0.1 - 3.0 eV), which are plotted in Fig. 4.2(a). The spectra reflect the anisotropic electronic structure of this crystal. We observed a large difference between the spectrum with the polarization parallel to the 1D chain (the *a*+*c* axis, blue line) and perpendicular to the chain (the *b* axis, orange line).

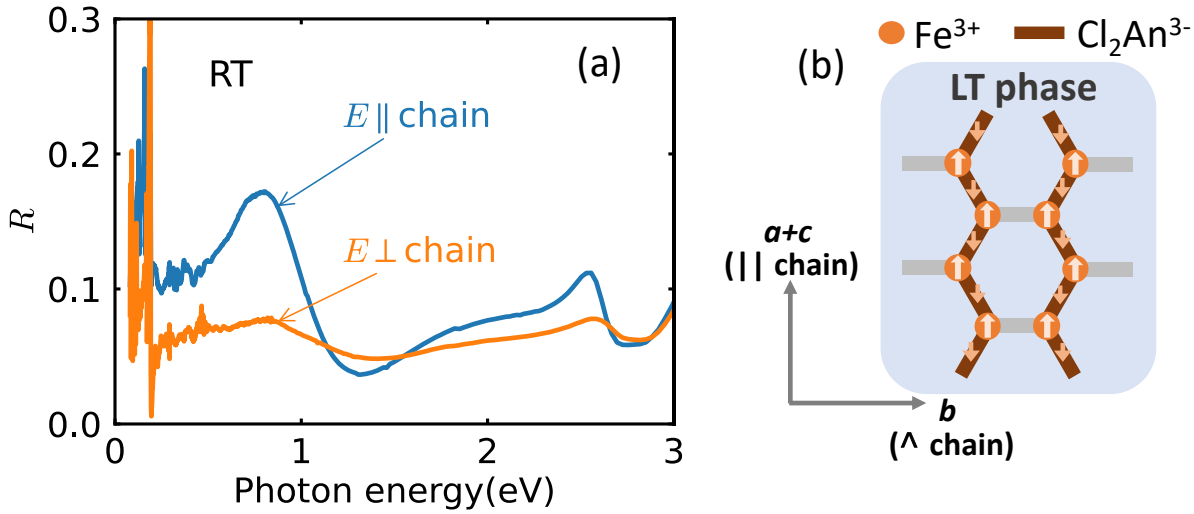

Fig. 4.2: (a) Steady-state reflectivity (*R*) spectra of a single crystal of $(NPr_4)_2[Fe_2(Cl_2An)_3]$ polarized with $E \parallel$ chain (blue line) and $E \perp$ chain (orange line) at room temperature (300 K: RT). (b) Schematic charge and spin patterns in the low-temperature (LT) phase.

Anisotropy of optical conductivity spectra at RT

Reflectance spectrum measurement is suitable for evaluating the physical properties of single-crystal samples because it is non-contact and requires relatively little sample preparation if the crystal surface has a mirror surface. However, obtaining physical property parameters directly from the spectra is difficult. The most commonly used analysis methods are either fitting analysis using Lorentz oscillator or calculation of complex reflectance spectrum using Kramers

Kronig transform, converted into intuitively easy-to-understand spectrum such as optical conductivity spectrum representing light absorption. Here, we examine the latter method.

The details of the Kramers-Kronig transform method are written in Appendix A. However, it is essential to note that the actual calculation requires reflectance spectra for the entire energy range from 0 to infinity (∞). As a practical matter, it is impossible to prepare such a spectrum experimentally, so a simple function extrapolation is used to replace the spectrum outside the measurement range. Since the material is an insulator in the entire temperature range according to the results of electrical resistivity measurements, etc., extrapolation on the low-energy side was performed by extrapolating the lowest energy value of the measured reflectance spectrum to 0 eV as a constant. In contrast, extrapolation at high energies is not straightforward. Usually, extrapolation is done as a power of photon energy (ω^{-n}). Here, the power value n is usually an arbitrary integer less than or equal to 4. This is because, according to the Lorentz oscillator model often used in reflectance spectral analysis, the functional form of reflectance at energies sufficiently higher than the resonance frequency is proportional to ω^{-4}.

Fig. 4.3 shows the optical-conductivity [σ(ω)] spectra obtained from a Kramers–Kronig (KK) transformation of the reflectivity. We observed two absorption peaks at around 0.8 and 2.6 eV. Assignment for these two optical transitions is discussed based on Quantum-chemical calculations in the next section.

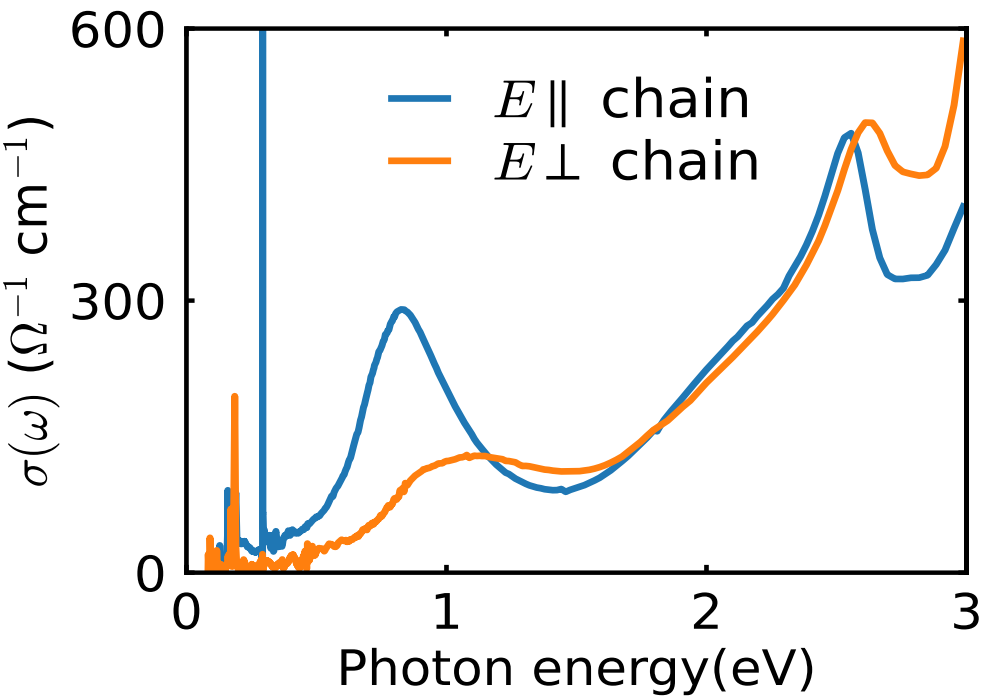

Fig. 4.3: Optical conductivity [σ(ω)] spectra of the single crystal with $E \parallel$ chain (blue line) and $E \perp$ chain (orange line) at RT.

The calculation of absorption spectra using time-dependent density functional theory (TD-DFT)

We performed the DFT calculations using Gaussian16 [133] with the B3LYP functional and employing the LANL2DZ basis set for the Fe atoms and the 6-31G(d) basis set for the C, Cl, and O atoms.

For the calculation of absorption spectra using time-dependent density functional theory (TD-DFT), we utilized the structure of the D_2A_3-type honeycomb layer, $Fe_2(Cl_2An)_3$, as shown in Fig. 4.4(a). The portion surrounded by the tick dashed line is magnified in Fig. 4.4(b) and used to obtain the absorption spectra by quantum chemical calculation. The XYZ coordinates of the atoms in the cluster are from the crystallographic information file (CIF) for the target compound $(NPr_4)_2[Fe_2(Cl_2An)_3]$ at 300K in Ref. [126] (Table in Appendix B). The time-

dependent density functional theory (TD-DFT) calculation with B3LYP functional and LANL2DZ for Fe atom, and 6-31G(d), for C, Cl, and O atoms, basis sets have been performed using Gaussian 16 [133] without optimization of the structure of the cluster. Peak positions are well reproduced when comparing the experimental absorption spectrum shown in Fig. 4.4(c) and the calculated spectrum in Fig. 4.4(d). It should be noted that the ratio between the number of Fe and Cl_2An ions in this cluster is 2:5, which is different from 2:3 in the target material. Then, the ratio of the oscillator strength among each transition must be different from the actual result. Only the peak energy should be discussed to assign the absorption peaks. The schematic representation for the assignment of absorption peaks is shown in Fig.4.5(d) and (e). XYZ coordinates of the cluster in Fig. 4.4(b) for TD-DFT calculation are provided in Appendix B. Regrettably, the absorption spectrum for the HT phase could not be reproduced with the same level of theoretical calculation. Therefore, to understand the change of spectral weight of the intra-molecular transition by valence changes at $T_{1/2(1)}$ and $T_{1/2(2)}$, the absorption spectra for single molecules Cl_2An^{3-} and Cl_2An^{2-} (with B3LYP functional and 6-31G basis set) has been calculated. The peak positions of the Cl_2An^{3-} and the Cl_2An^{2-} ions are almost the same as those in the target material, as shown in Fig. 4.4(e). The spectral weight of the intra-molecular absorption peak of the single ions shows the same tendency to the valence change of the Cl_2An ions in the spectral weight in the experimental absorption spectra of the target material.

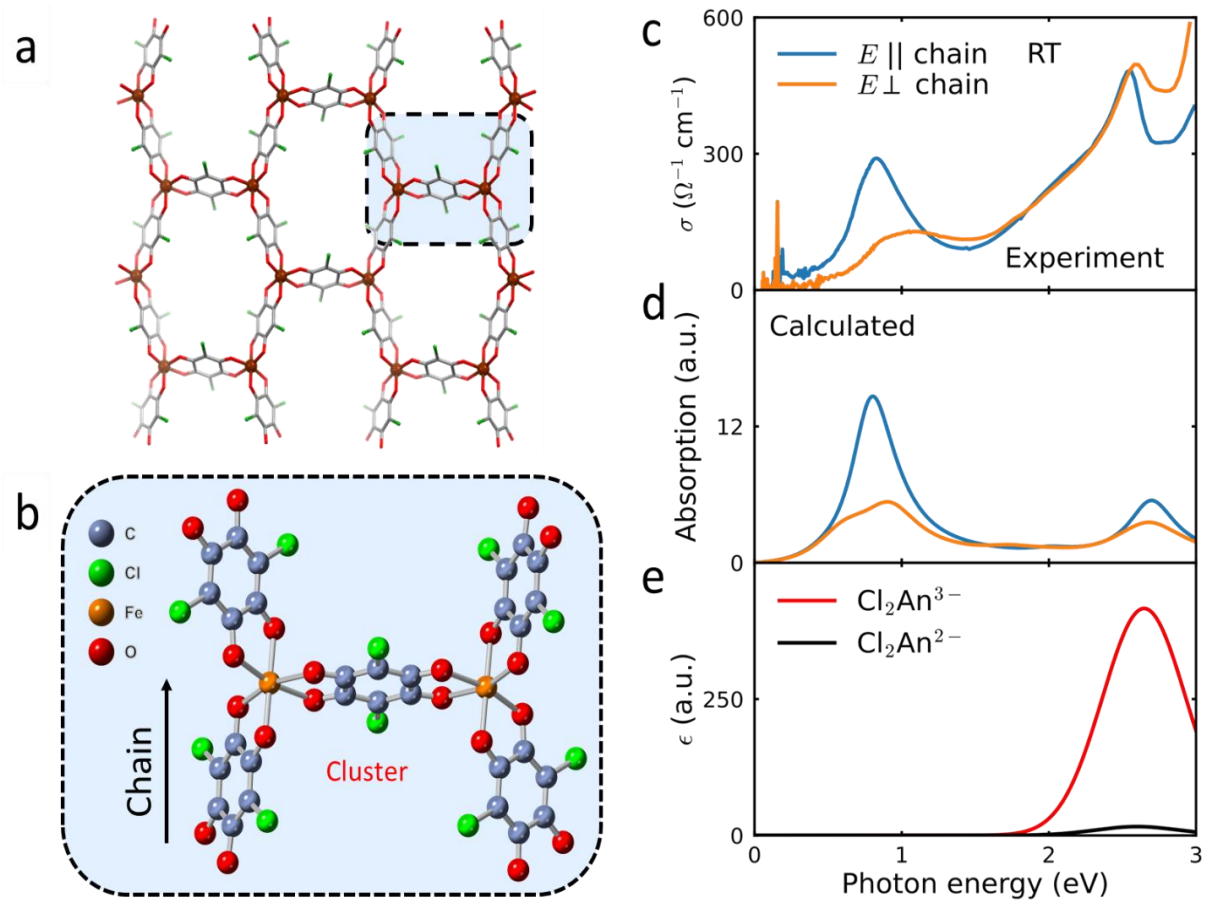

Fig. 4.4: (a) Structure of D_2A_3-type honeycomb-layer, $Fe_2(Cl_2An)_3$. (b) The molecular cluster is used for density functional theory (TD-DFT) calculation. (c) and (d) The comparison between the LT phase's theoretical and experimental absorption spectra. (e) The theoretical absorption spectra for the isolated Cl_2An^{3-} and Cl_2An^{2-} ions.

Suppose we closely observe the electronic transition nature of ~ 0.8 eV peak (molecular orbital (MO) representation). In that case, the absorption peak assigns the CT transition between D and A, as shown in Fig. 4.5(a), (b), and (c). Those three transitions are the major contributions to the CT transition. However, among all the major transitions in the 0.8 eV peak, the transition for HOMO – 1 (highest occupied MO) to LUMO + 1 (lowest unoccupied MO) (Fig. 4.5(b)) is the primary one. The transition is not purely CT type; rather, we consider this transition as a combination of ligand to metal (LMCT), band-like, or d-d type. Overall, the peak at around 0.8

eV has the character of a CT transition between the Fe and Cl_2An ions (Fig. 4.5(d)), while the peak at around 2.6 eV is attributed to an intramolecular transition in the Cl_2An ions (Fig. 4.5(e)).

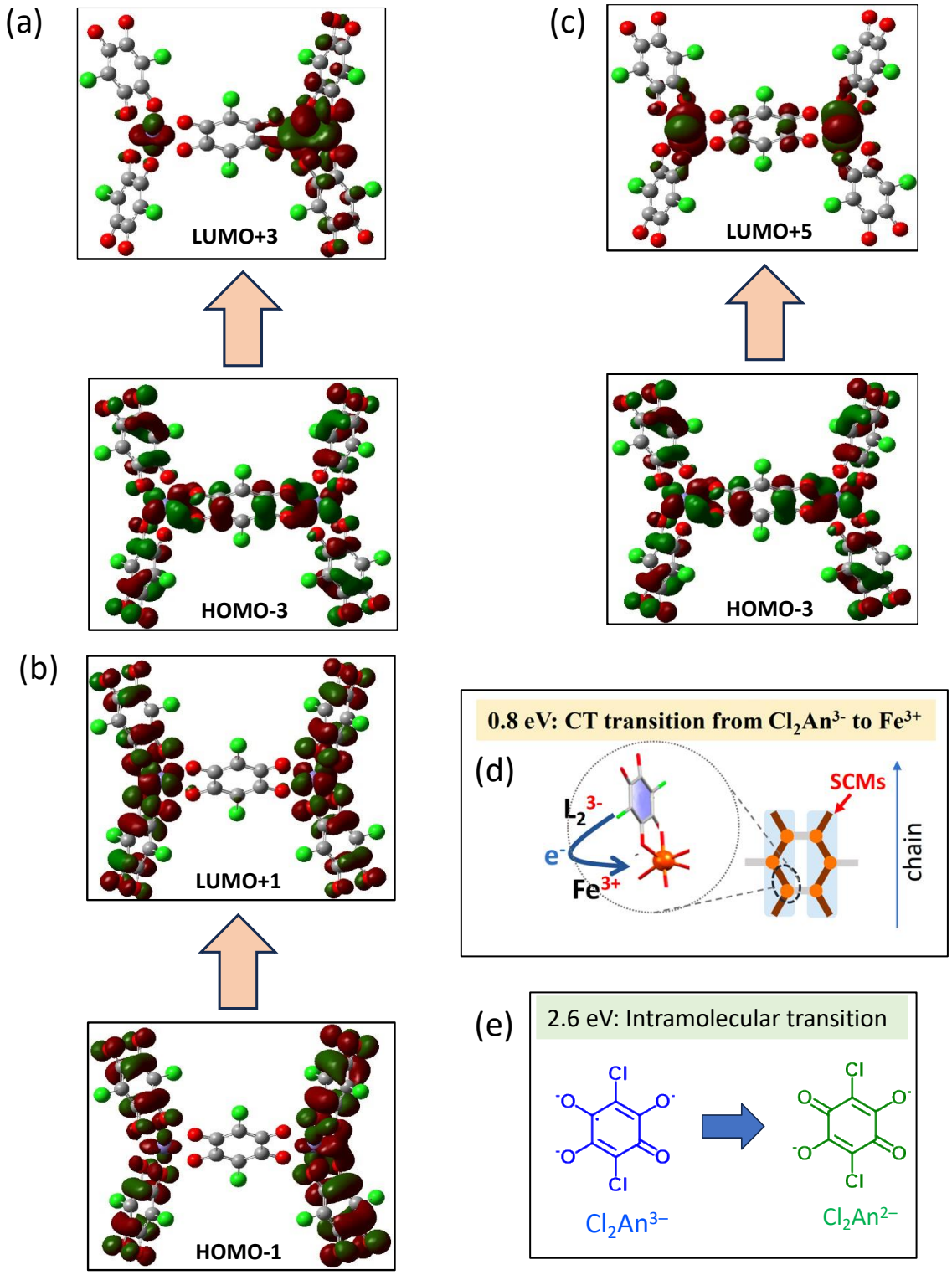

Fig. 4.5: (a), (b), and (c) are the MO diagrams of major electronic transitions for ~ 0.8 eV peak

in the optical spectrum along the *E* || chain in molecular clusters. (d) The schematic representation of CT transition between D and A. (e) The intramolecular transition between Cl_2An ions.

4.2.3 Temperature-dependent optical spectra along E ||chain

The reflectance spectra of E || chain polarization were measured from 296 to 380 K over the entire measurable energy range. The results are shown in Fig. 4.6. Significant temperature variations were observed.

We reported the σ(ω) spectra with *E* || chain at 296, 340, and 380 K depicted in Fig. 4.7(a) are typical of the LT, IM, and HT phases, respectively. We integrated the σ(ω) spectra with *E* || chain at each temperature in the photon-energy range 0.7–0.9 eV and 2.5–2.7 eV to determine the spectral weights of the CT and intramolecular transitions, as shown in Fig.4.7(b) and Fig. 4.7(c), respectively. The spectral weight of each peak shows a steep drop at around each $T_{1/2}$ due to the LT–IM and IM–HT phase transitions [the vertical dashed lines in panels (b) and (c)]. The variations of the spectral weights are consistent with the expected valence changes of the Fe and Cl_2An ions that accompany the two-step phase transition [126]. These integrated intensities can, therefore, be utilized as suitable probes for detecting the degree of CT between the Fe and Cl_2An ions.

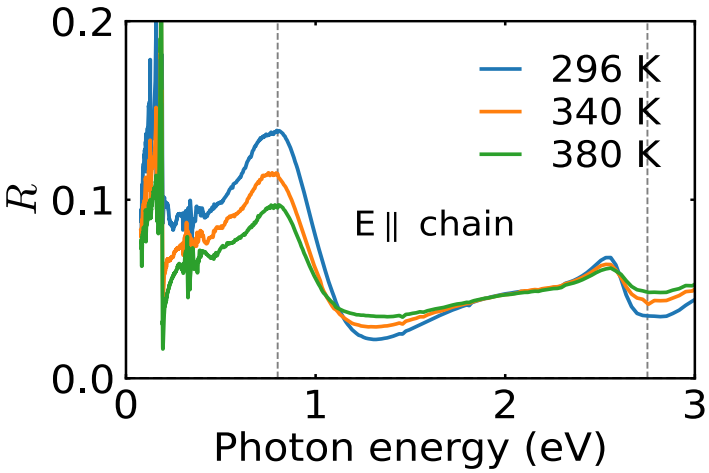

Fig. 4.6: Temperature dependence of the reflectivity spectra at 296 (blue line), 340 (orange line), and 380 K (green line) with $E \parallel$ chain.

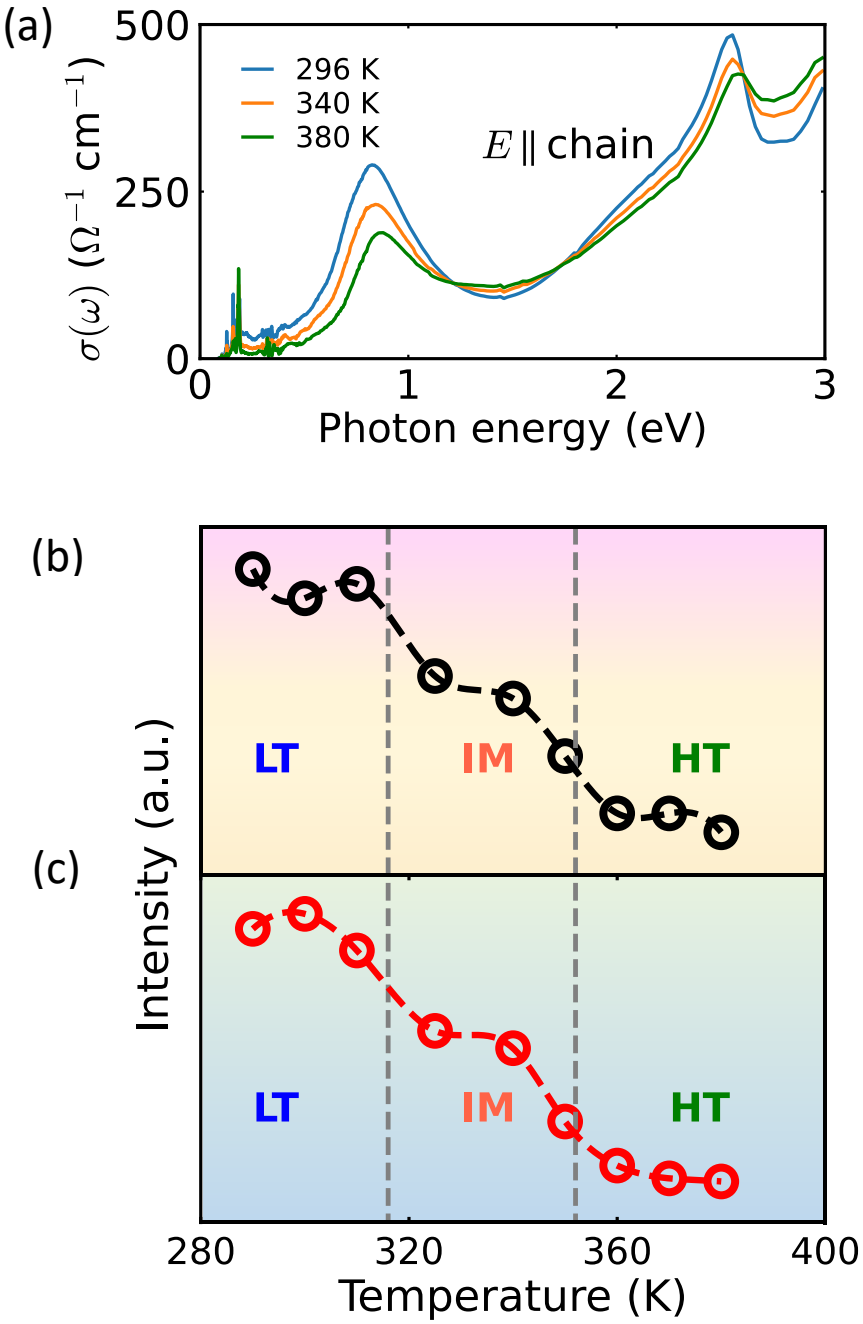

Fig. 4.7: (a) Temperature dependence of the σ(ω) spectra with E || chain. (b) Temperature dependence of the integrated σ(ω) between 0.7 and 0.9 eV. (c) Temperature Dependence of the integrated σ(ω) between 2.5 and 2.7 eV. The dashed lines represent the transition temperatures $T_{1/2(1)}$ (317 K) and $T_{1/2(2)}$ (354 K) of the charge-transfer (CT)-type phase transitions based on previous magnetic and structural studies [126].

4.2.4 Temperature-dependent optical spectra along E ⊥ chain

The reflectance spectra of E ⊥ chain polarization were measured from RT to 380 K within the energy range of 0.08 – 1.4 eV. The results are shown in Figure 4 8. The difference changes along the E⊥ chain are very small, but explaining the ultrafast photo-induced responses along the E ⊥ chain is useful, which will be discussed later.

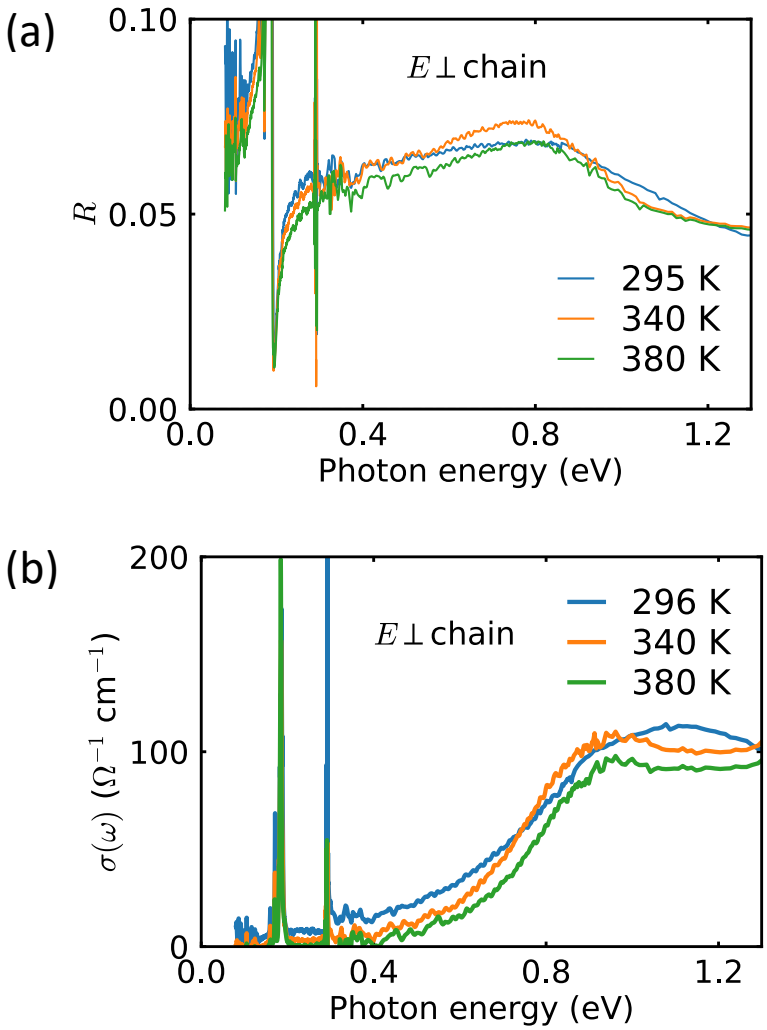

Fig. 4.8: Temperature dependence of (a) the reflectivity spectra and (b) σ(ω) spectra along the *E* ⊥ chain.

4.2.5 Temperature dependent Raman spectra for both *E* || chain and E ⊥chain directions

Raman spectra of $(NPr_4)_2[Fe_2(Cl_2An)_3]$ were collected over the temperature range 293 – 380 K for both *E* || chain and E ⊥ chain directions. The result of Raman spectra without using an analyzer of polarization is shown in Fig. 4.9 (a) and (b).

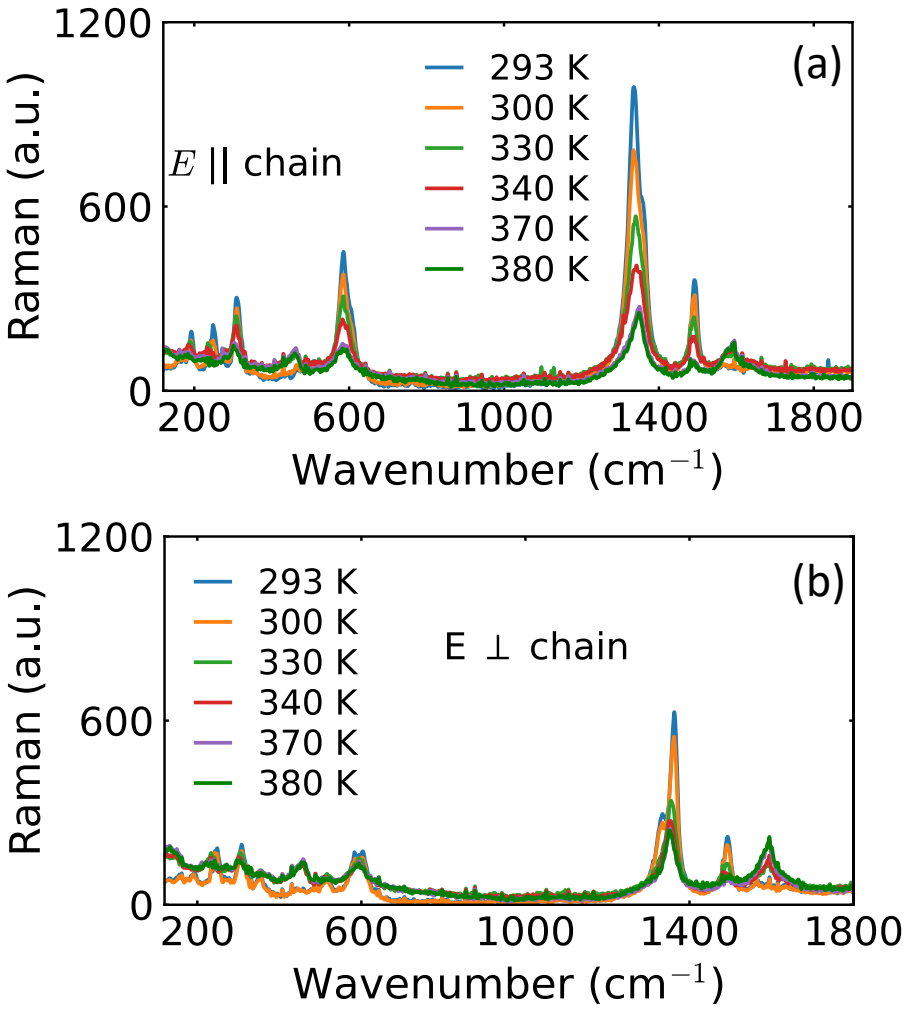

Fig. 4.9: Temperature-dependent Raman spectra along (a) *E* || chain and (b) E ⊥ chain directions.

Also, we measured the Raman spectra over the temperature range 293 – 380 K using the analyzer of polarization, in which 'xx' and 'xy' mean that the polarization directions of the analyzer are respectively parallel and perpendicular to the polarization of the input light (E || chain or E ⊥ chain). The Raman spectra at 293 K (LT phase), 340 K (IM phase), and 380 K (HT phase) are shown in Fig. 4.10.

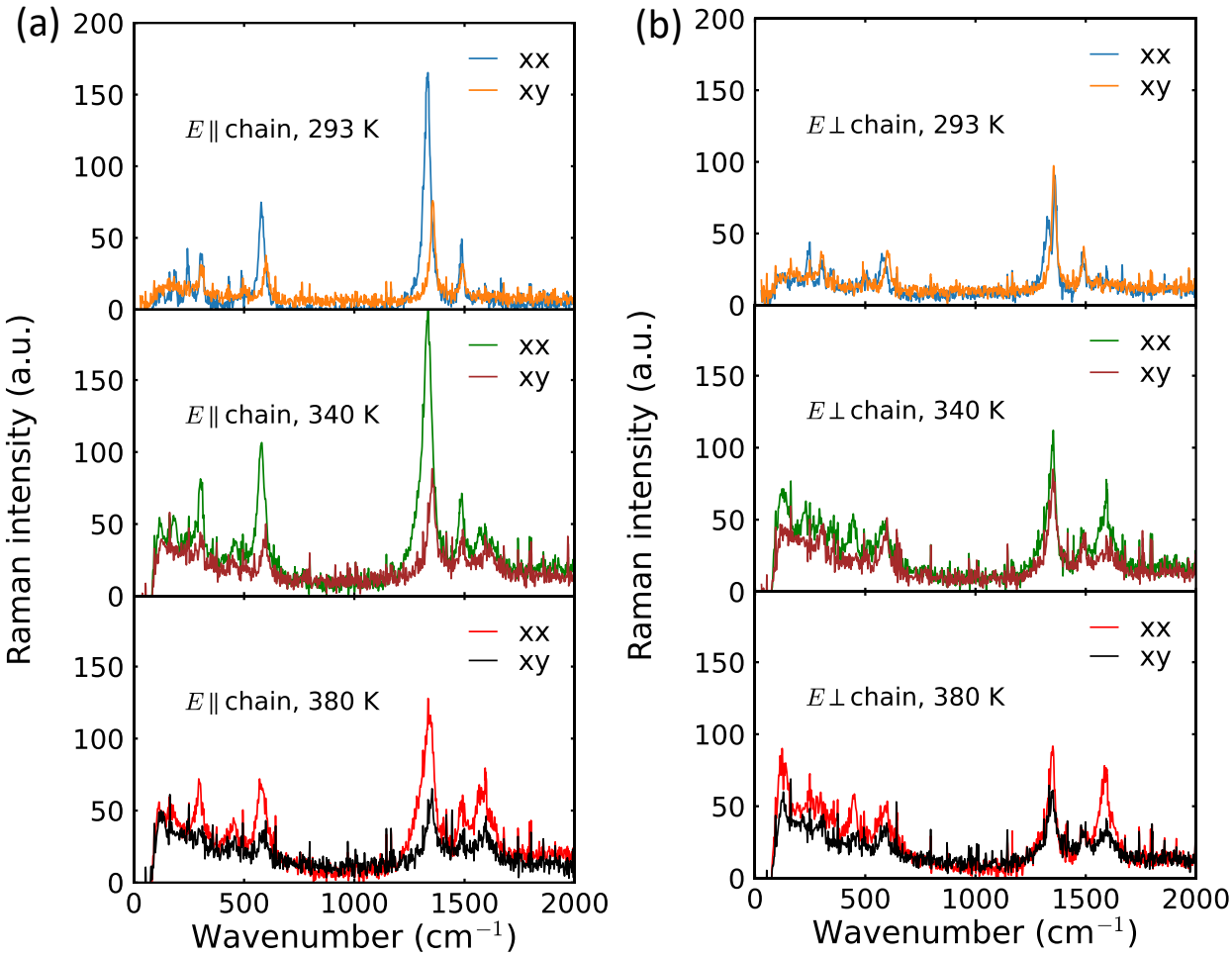

Fig. 4.10: Raman spectra at 293 K, 340 K, and 380 K with 'xx' and 'xy' polarization geometries along (a) E || chain and (b) E ⊥ chain directions.

4.3 Summary

The results and observations from the static optical spectroscopy measurement are summarized in this chapter. The CT transition between Fe and Cl_2An ions and intramolecular transitions are well clarified using static optical conductivity spectrum along the E ‖ chain, located at 0.8 eV and 2.6 eV, respectively. On the other hand, the LT–IM and IM–HT phase transitions cause a sharp decline in the temperature-dependent optical conductivity spectrum throughout the E ‖ chain at about every $T_{1/2}$ for the temperature ranges from RT to 380 K. This suggests that static optical spectroscopic measurement can be an excellent probe for observing CT-type phase transition in our sample, $(NPr_4)_2[Fe_2(Cl_2An)_3]$. The temperature-dependent Raman spectrum we recorded here will also assist in explaining the intriguing results of ultrafast time-resolved spectroscopy (pulse width, 90 fs, and 6 fs), which will be covered in the upcoming chapters.

Chapter 5

5. Time-resolved spectroscopic study of $(NPr_4)_2[Fe_2(Cl_2An)_3]$: Exciting LT phase using 90 fs pulses

In this chapter, we discussed the ultrafast photoinduced dynamics in a DA-type layered MOF that exhibits a charge-transfer (CT)-type phase transition: $(NPr_4)_2[Fe_2(Cl_2An)_3]$ at room temperature (RT: 300K). We measured photoinduced transient spectra in intramolecular transition, CT, and mid-IR energy range. Moreover, the ultrafast formation of new spectral structures in the CT transition and the mid-IR energy ranges demonstrates, for the first time, the appearance of a new, transient electronic state in the present MOF system, with a unique lattice structure that is different from the one observed in thermal equilibrium, i.e., a photoinduced hidden state.

5.1 Objective and Motivation of this experiment

From the published article in 2020 by Prof. Miyasaka's group, it is evident that our selected sample, $(NPr_4)_2[Fe_2(Cl_2An)_3]$, exhibits a two-step CT type phase transition, T_c at around 317 and 354 K. The primary goal of this research is to control crystal functionality– based on the electronic structural change using external stimuli, such as light. Commonly, after photoexcitation processes, such as a charge transfer, chemical reaction, or photovoltaic, it often exhibits subsequent dynamics within the attosecond (10^{-18}) to picosecond (10^{-12}) timescale.

Here, our motivation is to observe the dynamics related to CT-type phase transition using ultrafast femtosecond pump-probe spectroscopy with a time resolution of 90 fs. The detailed procedure of measurement and experimental setup is discussed in Chapter 3 (section 3.5.2.1). The result, analysis method, and discussion will be presented in this chapter.

5.2 Experimental condition, result, and discussion

5.2.1 Experimental condition for time-resolved experiment for $(NPr_4)_2[Fe_2(Cl_2An)_3]$ at RT

We performed time-resolved reflectivity measurements using an optical pump–probe technique to confirm the occurrence of a photoinduced CT-type phase transition in this MOF system. We used a pump light with a photon energy of either 0.73 or 0.8 eV (E || chain) (considering CT transition peak excitation) and a 90 fs pulse width. We monitored the relative reflectivity change ($\Delta R/R$) induced by photoexcitation of the CT band over a wide range of probe-photon energies (0.1–3.0 eV) at RT, as shown in Fig. 5.1, i.e., in the LT phase. We maintained the pump fluence of 1.0 mJ/cm^2 during all the measurements.

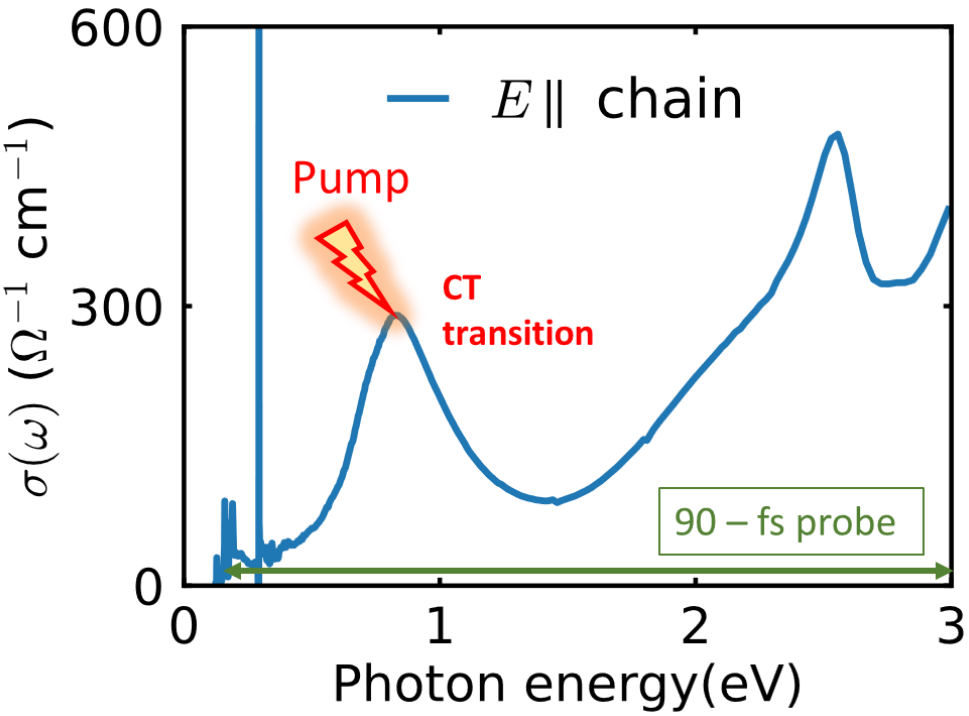

Fig. 5.1: Optical conductivity [σ(ω)] spectra of the single crystal with E || chain at RT. Here, we excited CT transition and monitored photoinduced $\Delta R/R$ over a wide range of probe-photon energies (0.1–3.0 eV).

Result and discussion

5.2.2 Photoinduced transient Δ*R/R* spectrum along *E* || chain at RT

The photoexcitation conditions must be the same during the measurement to obtain the ΔR/R spectra of the photoinduced transient state. However, we had to choose two different photon energies, 0.73 and 0.8 eV, as the pump light to make the Δ*R/R* spectra around the CT peak. The reason for two different photon energies is the lack of suitable optical filters to cut the pump light scattered from the crystal surface effectively. The energies of the pump lights are denoted as red (0.73 eV) and black (0.8 eV) dashed lines in Fig. 5.2(a) with the initial state σ(ω) spectrum, at 296 K using *E* || chain. In Fig. 5.2(b), the Δ*R/R* spectrum plotted by red circles is measured using 0.73 eV excitation at 0 ps, and that plotted by black circles is measured using 0.8 eV excitation at 0 ps. The red and black circles seem to be connected smoothly. Fig. 5.2(c) shows the temporal profiles of Δ*R/R* for probe energy of 1.46 eV, using 0.73 (red circles) and 0.8 (black circles) eV excitations. The similarity of the amplitude and the temporal dependence of Δ*R/R* assures the observation of the same photoinduced dynamics. Based on these results, the validity of using two different photon energies to make the Δ*R/R* spectrum by CT excitation in the wide energy range must be approved.

Compare photoinduced and thermal-induced Δ*R/R* spectra

Fig. 5.3(a) shows the isothermal static reflectivity spectra measured at the temperatures 296, 340, and 380 K—corresponding to the LT, IM, and HT phases, respectively—and with *E* || chain. The broad photon-energy range covers the range of intramolecular transitions (2.0–3.0 eV), the CT transition (0.5–1.5 eV), and molecular vibrations (mid-IR, 0.15–0.25 eV). These three photon-energy ranges are labeled as green-, brown-, and yellow-shaded regions, respectively. The differences (Δ*R/R*) in the isothermal reflectivity spectra between 296 K and 340 K and between 296 K and 380 K are shown as orange and green lines, respectively, in Fig. 5.3(b).

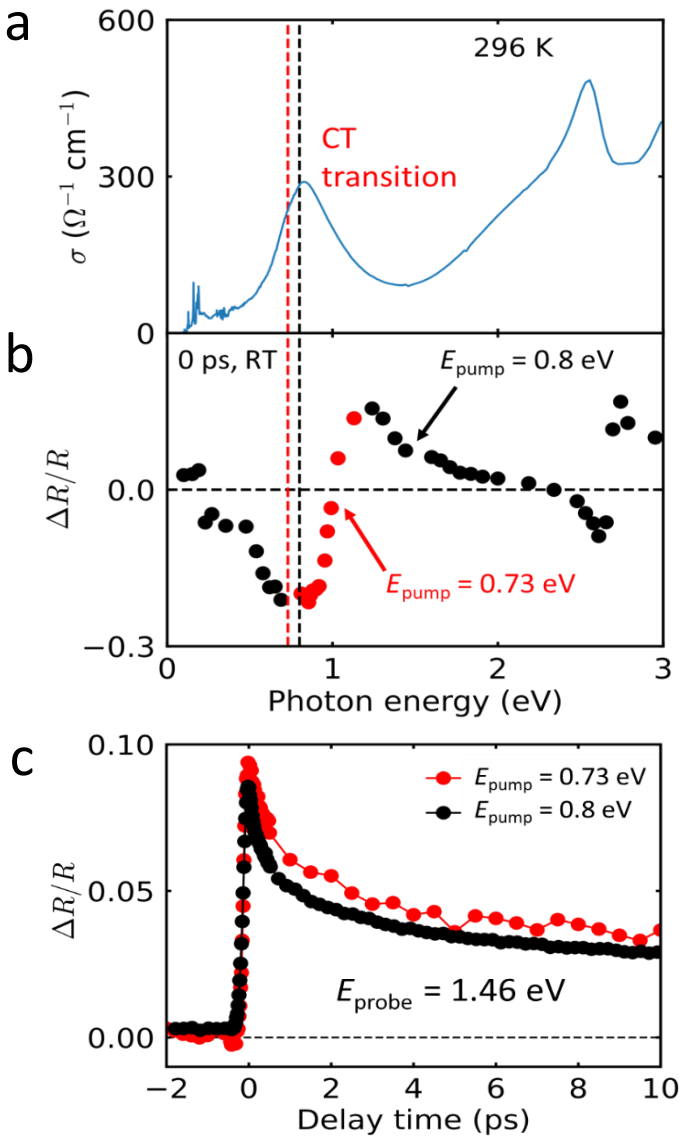

Fig. 5.2: (a) The σ(ω) spectra with $E \parallel$ chain at 296 K. The dashed red (0.73 eV) and black (0.8 eV) lines are the positions of the photon energies of the pump lights. (b) The transient reflectivity change ($\Delta R/R$) spectra at 0 ps. Red and black circles were $\Delta R/R$ with the excitation of 0.73 and 0.8 eV, respectively. (c) The typical temporal profiles of $\Delta R/R$ at a probe energy of 1.46 eV and pump energies of 0.73 (red circles) and 0.8 eV (black circles) [128].

They correspond to the $\Delta R/R$ spectra expected in thermally induced phase changes from the LT to the IM and HT phases. The $\Delta R/R$ spectra observed just after photoexcitation (0 ps, open black circles) and at 10 ps (open pink circles) with a pump fluence of 1.0 mJ/cm^2 are also plotted in Fig. 5.3(b). We observed considerable differences between the spectral shapes of the photoinduced $\Delta R/R$ (open black and red circles) and the thermally induced values (the orange and green lines) both in the region of the CT transition (the brown-shaded area) and in the mid-IR region (the yellow-shaded area). For simplicity, we next consider the transient reflectivity spectra in these three energy ranges separately and hereafter discuss in detail what we observed in each energy range to obtain further insight into the effect of photoexcitation in the present MOF.

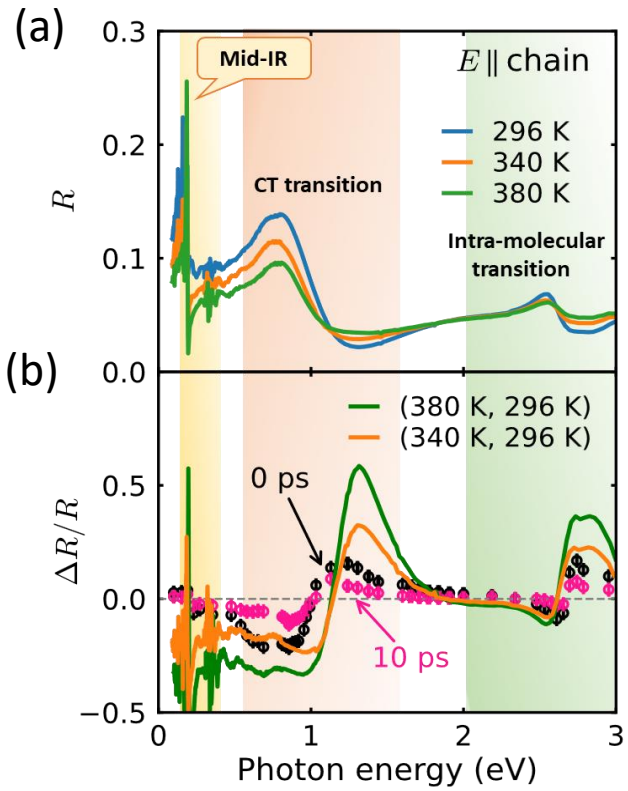

Fig. 5.3: (a) Temperature-dependent R spectra of a single crystal of $(NPr_4)_2[Fe_2(Cl_2An)_3]$ with $E \parallel$ chain. (b) Transient reflectivity ($\Delta R/R$) spectra with $E \parallel$ chain for pump and probe pulses at $\Delta t = 0$ (black circles) and 10 ps (pink circles) at RT (LT phase). The fluency of the pump pulse is $I_{ex} = 1.0$ mJ/cm^2. The $\Delta R/R$ spectrum with the $E \parallel$ chain between 296 K (the LT phase) and

380 K (the HT phase) is shown as a green line, and that between 296 K and 340 K (the IM phase) is shown as an orange line. The energy ranges corresponding to intramolecular transitions (2.0–3.0 eV), the CT transition (0.5–1.5 eV), and molecular vibrations (mid-IR, 0.15–0.25 eV) are designated by green-, brown-, and yellow-shaded regions, respectively [128].

Time evolution of reflectance change (ΔR/R)

Fig. 5.4 shows a few examples of the time profile of the reflectance change after the time origin correction. Excitation was performed with E || chain polarized light at 0.73 or 0.8 eV, and the energy in the legend represents the photon energy of the Probe light (E || chain). The time evolution of ΔR/R in the mid-IR, CT-transition, and intramolecular transition energy range are shown from left to right. The reflectance change is significant immediately after light irradiation at all wavelengths, followed by more than one relaxation process. From preliminary observation, the relaxation process has three components: (i) a fast relaxation component immediately after excitation (red arrow), (ii) a slow relaxation component (green arrow), and (ii) a long-lived constant component (blue arrow). Next, we attempted to understand the phenomena associated with photoexcitation by fitting analysis of the temporal profiles in a few probe energies.

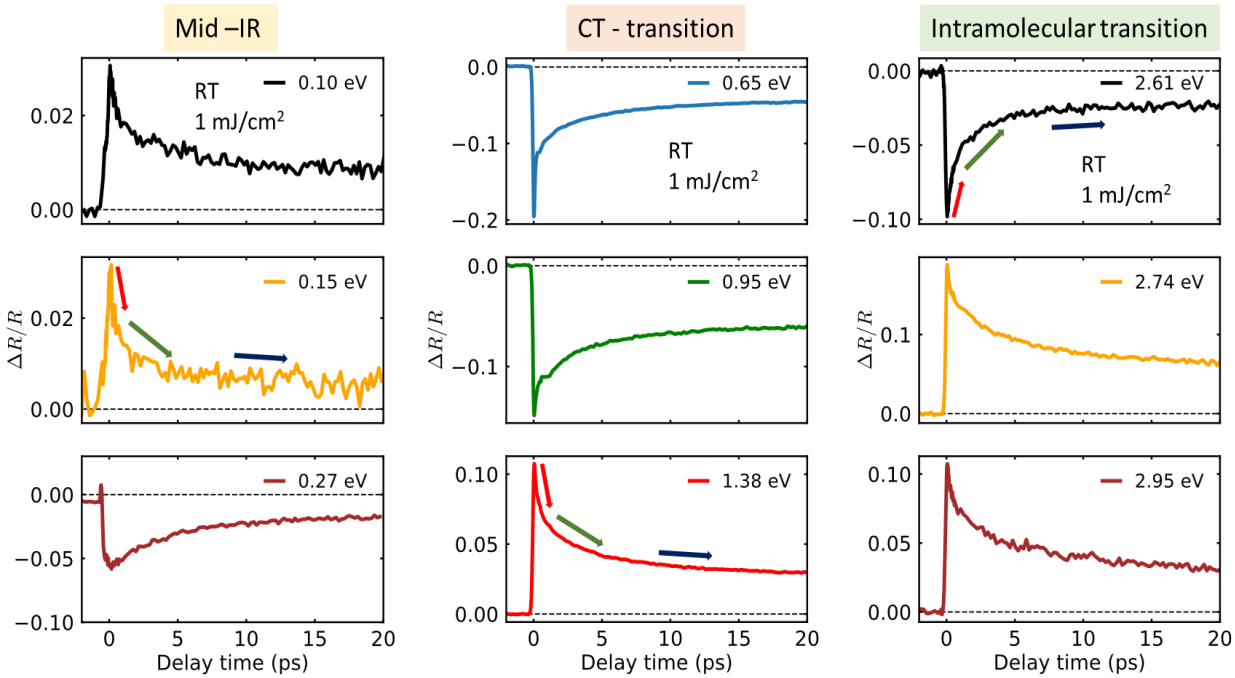

Fig. 5.4: A few examples of the time profile of the reflectance change ($\Delta R/R$) spectra for different probe energy ranges (Mid-IR, CT, and intramolecular transition).

Excitation intensity dependence of ΔR/R

Fig. 5.5 shows the time evolution of the reflectance change at each excitation intensity (measurement temperature RT, probe energy 0.65 (Fig. 5.5(a)) and 2.74 eV (Fig. 5.5(b))) in the time region from up to 20 ps. We measured time evolution for the excitation intensity of 0.2 - 1.0 mJ/cm^2. For both the probe energies, the shape of the graph does not depend on the excitation intensity and is the same for all excitation intensities. Fig. 5.5(a) and (b), lower panel, shows the plot of $\Delta R/R$ concerning the excitation intensity. The result shows the linear dependence of $\Delta R/R$ on I_{ex}. Hence, it follows the second law of photochemistry, the Stark-Einstein law, which states that for each photon of light absorbed by each molecule, only one molecule is activated for subsequent photoexcitation.

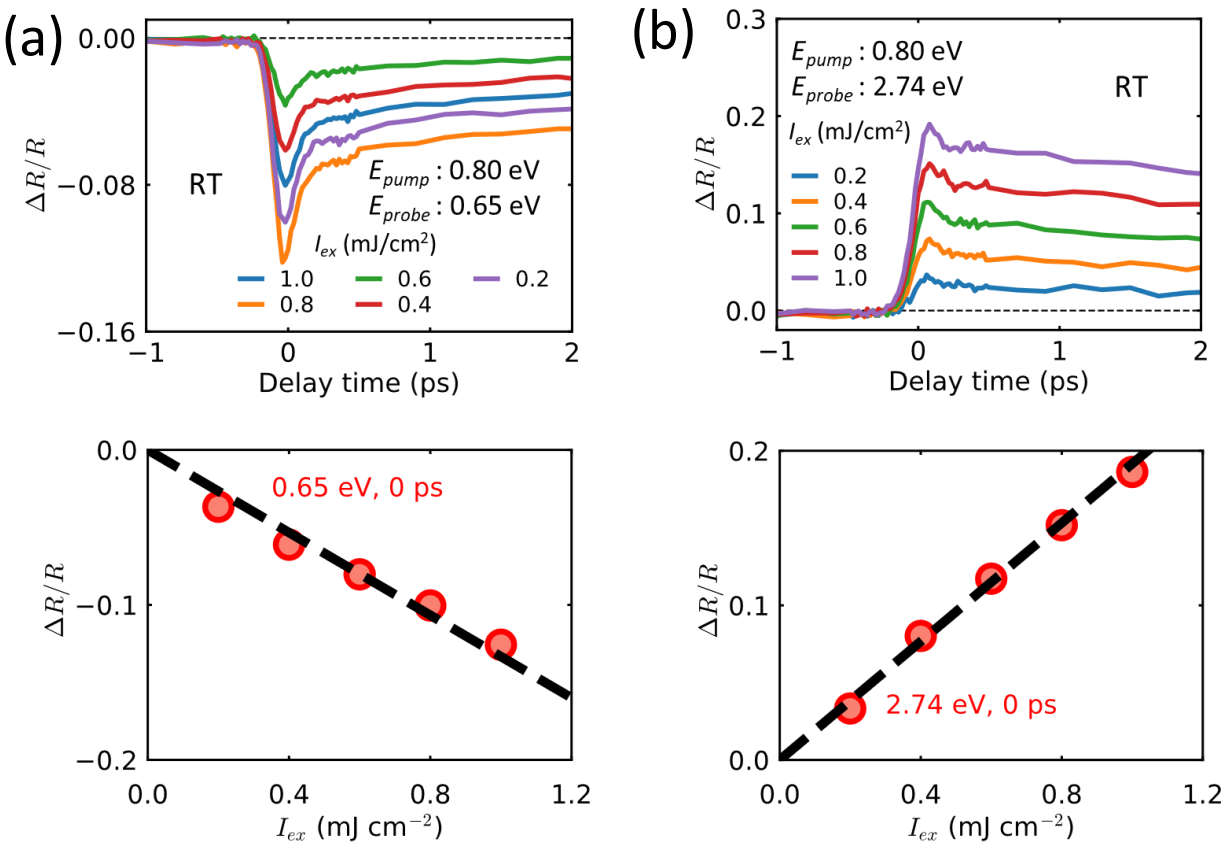

Fig. 5.5: The time evolution of $\Delta R/R$ for each excitation intensity of pump light and the plot of $\Delta R/R$ with respect to the excitation intensity for (a) 0.65 and (b) 2.74 eV probe energies.

Fitting of time evolution of *ΔR/R*

Fig. 5.6(a), Fig. 5.6(b), and Fig. 5.6(c) show typical temporal profiles of *ΔR/R*. The fitting analysis has been performed using equation (5.1) with the convolution of the Gauss function, which represents the time resolution determined by the pulse width of the pump and the probe lights. Due to the convolution of the Gauss function, the full width at half maximum (FWHM) of the Gauss function is added as a fitting parameter.

$$f(t) = a_1 \exp\left(-\frac{t}{\tau_1}\right) + a_2 \exp\left(-\frac{t}{\tau_2}\right) + a_3. \tag{5.1}$$

The experimental curves are well-fitted, as shown in Fig. 5.6(a), Fig. 5.6(b), and Fig. 5.6(c). Then, the photoinduced dynamics by CT excitation have at least three kinds of relaxation processes. The obtained parameters are summarized in Table S1.

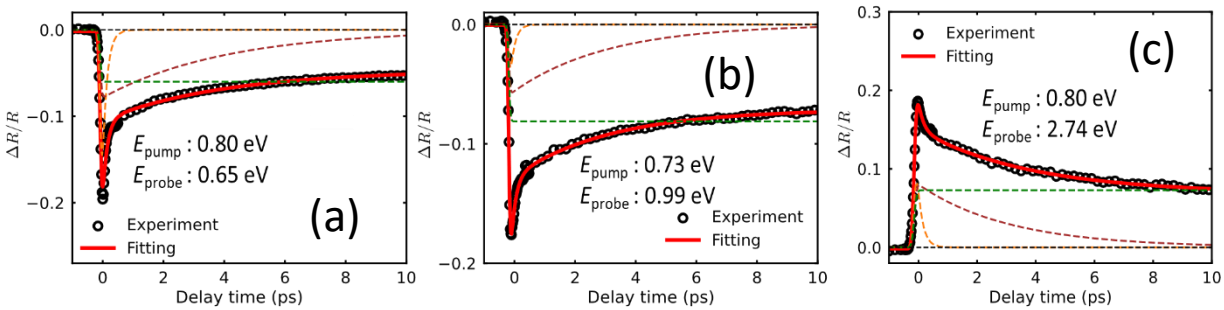

Fig. 5.6: The typical temporal profiles of Δ*R/R* with fitting results at a probe energy of (a) 0.65 eV, (b) 0.99 eV, and (c) 2.74 eV.

Table 5.1. The values of fitting parameters for fitting analysis of temporal profiles of Δ*R/R* at the probe energies of 0.65, 0.99, and 2.74 eV.

	0.65 eV	0.99 eV	2.74 eV
FWHM	123 ± 6 fs	110 ± 3 fs	162 ± 4 fs
τ_1	160 ± 9 fs	160 ± 8 fs	150 ± 10 fs
τ_2	3.1 ± 0.26 ps	3.17 ± 0.25ps	3.3 ± 0.2 ps

The spectral shape of the photoinduced transient state just after the photoexcitation at which the Δ*R/R* shows the maximum amplitude in the temporal profile curve is discussed in this work. The obtained fitting result for the probe photon energies suggests that the time resolution is around 110 fs, as shown in Table 5.1. Thus, the generation speed of the photoinduced state (just after photoexcitation) is within the time scale of 110 fs.

5.2.2.1 Transient *ΔR/R* spectrum in the intramolecular transition energy range (2.0 – 3.0 eV)

Fig. 5.7(a) shows the isothermal static reflectivity spectra measured at the temperatures 296, 340, and 380 K with *E* || chain, and the differences (Δ*R/R*) in the isothermal reflectivity spectra between 296 K and 380 K are shown as the green line in Fig. 5.7(b) in the energy range of 2.0–3.0 eV. The open black, orange, and pink circles show the Δ*R/R* spectrum with a time delay of 0, 1, and 10 ps at RT, respectively. The photoinduced *ΔR/R* spectra are very similar to the thermal induced *ΔR/R* spectrum. It suggests photoinduced conversion of the LT phase to the HT phase. A quantitative evolution is necessary to comprehensively grasp photo-conversion efficiency, which will be discussed in the following sections.

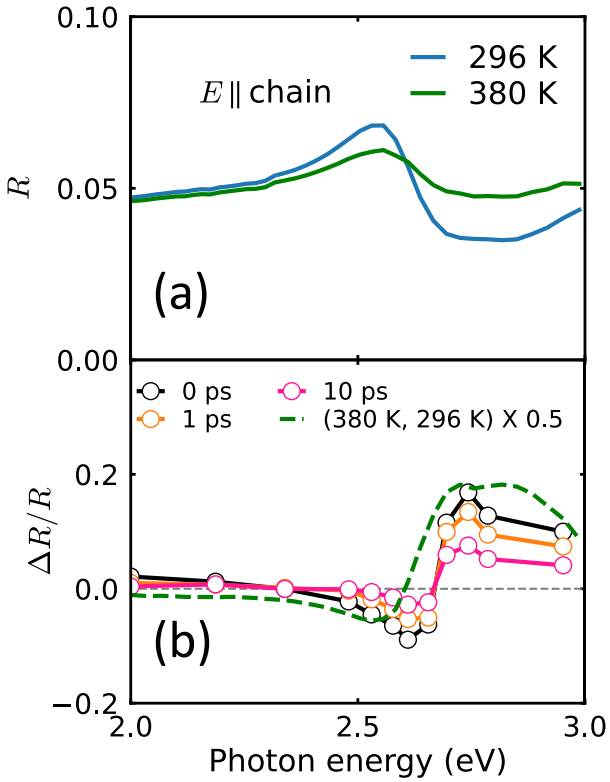

Fig. 5.7: (a) Temperature-dependent R spectra of a single crystal of $(NPr_4)_2[Fe_2(Cl_2An)_3]$ with E || chain. (b) Transient reflectivity ($\Delta R/R$) spectra with E || chain for pump and probe pulses at Δt = 0 (black circles), Δt = 1 (orange circles), and 10 ps (pink circles) at RT (LT phase). The fluency of the pump pulse is I_{ex} = 1.0 mJ/cm^2. The $\Delta R/R$ spectrum with E || chain between 296 K (the LT phase) and 380 K (the HT phase) is shown as a green line within the 2.0 -3.0 eV energy range.

Quantitative analysis of transient *ΔR/R* spectrum in the intramolecular transition energy range (method and discussion)

To evaluate the photoinduced $\Delta R/R$ spectra quantitatively, it is necessary to consider the spatial distribution of the density of photoinduced states because the intensity of the pump light weakens as it penetrates deeper into the crystal from the light-irradiated sample surface. Therefore, we adopted the multilayer method of analysis described in refs. [61] and [134].

According to the multilayer method, we consider Just after the photoexcitation, the distribution of the photoinduced state $r(z)$ can be assumed as exponential-type, as shown in Fig. 5.8(a) and 5.8(b), when the volume of the photoinduced state is proportional to the absorbed photon number.

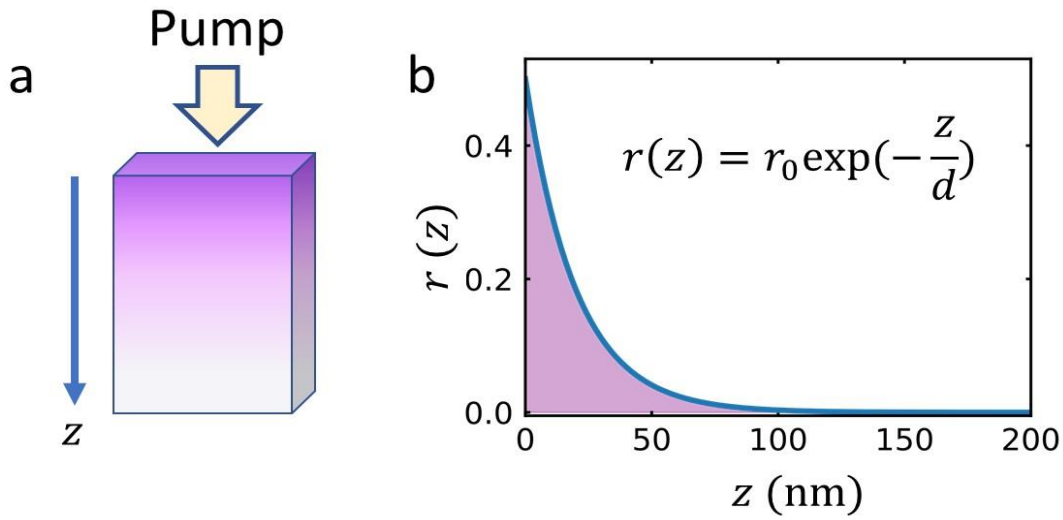

Fig. 5.8: (a) Schematic illustration of the distribution of the absorbed photon density. (b) The distribution of the excited state against the depth from the sample surface, which we assumed in the analysis, is exponential-type one.

Then, we constructed the dielectric function $[\varepsilon(\omega)]$ at depth z as a uniform mixture of the dielectric functions of the initial $[\varepsilon^{ini}(\omega)]$ and photoinduced $[\varepsilon^{PI}(\omega)]$ states. Given these assumptions, $\varepsilon(\omega)$ at depth, z is given by

$$\varepsilon(\omega, z) = \varepsilon^{PI}(\omega) r_0 \exp(-\frac{z}{d}) + \varepsilon^{ini}(\omega)\{1 - r_0 \exp(-\frac{z}{d})\}, \quad (5.2)$$

where ω is the frequency of the light and $\varepsilon^{ini}(\omega)$ is $\varepsilon(\omega)$ at 296 K. For discussing the intramolecular transition range 2.0–3.0 eV, we assumed $\varepsilon^{PI}(\omega)$ to be $\varepsilon(\omega)$ for the HT phase at 380 K $[\varepsilon^{HT}(\omega)]$, since it is reasonable to assume that the photoinduced CT excitation modulates the valence of the Cl_2An^{3-} ions (in the initial LT phase) into that of the Cl_2An^{2-} ions

(in the HT phase). The quantity r_0 ($0 < r_0 < 1$) represents the yield of the observed photoinduced state at the surface. The value of *d* is the specific length of the exponential-decay type distribution of photoinduced states, which we assume to be equal to the penetration depth of the pump light, about 162 nm. We determined this value from the KK analysis using the static reflectivity at 296 K.

$$d = \frac{1}{Abs_{0.8}}$$

$$d = \frac{1}{61756\ \mathrm{cm}^{-1}} = 162\ nm$$

The absorbance spectrum at 296 K (LT phase) is shown in Fig. 5.9 The dashed line shows the position of the pump photon energy 0.8 eV.

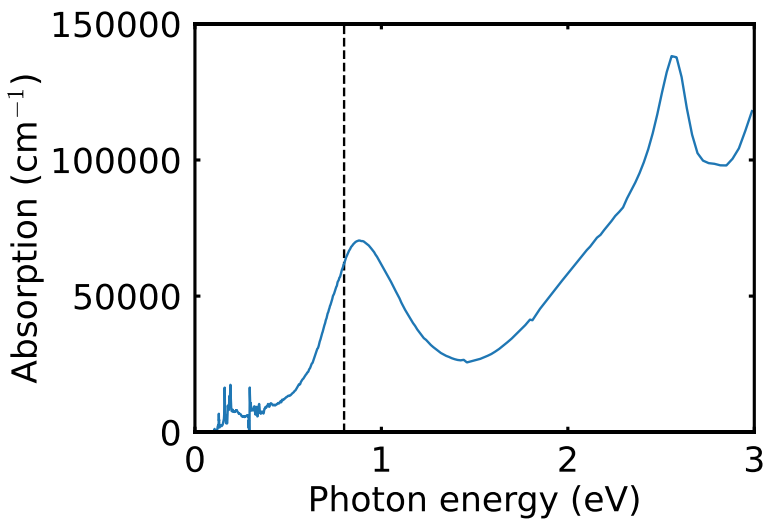

Fig. 5.9: The absorbance spectrum at 296 K. The dashed line shows the position of the pump photon energy 0.8 eV.

The reflectivity spectrum of the transient state can be calculated by using the transfer-matrix

method [135] for the accumulation of thin films with uniform $\varepsilon(\omega, z)$. The simulated $\Delta R/R$ spectrum has been calculated by the multilayer method in the energy range of 2.0–3.0 eV at a late delay time. As an assumption, the d value is fixed at 162 nm, the penetration depth at around CT transition energy, for all the delay time for simplicity. Only r_0 is the variable parameter in equation (1) (see the main text). Then r_0 has been evaluated by utilizing the least square method.

The thick purple line in Fig. 5.10(a) indicates that the calculated $\Delta R/R$ spectrum reproduces the experimentally observed spectrum well. We determined the value of r_0 to be 0.48 ± 0.002 from a least-squares fit to the 0 ps spectra. The result suggests the successful observation of photoinduced phase transition resembles the thermal-induced one.

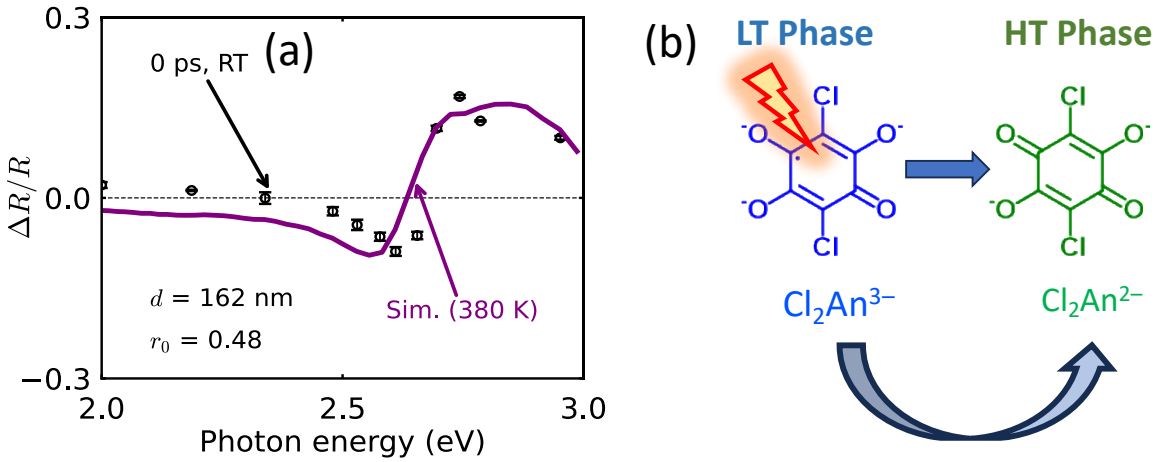

Fig. 5.10: (a) $\Delta R/R$ in the intramolecular transition region (~ 2.6 eV). The black circles represent the photoinduced values of $\Delta R/R$ at 0 ps and RT. The purple line shows the values of $\Delta R/R$ at 0 ps calculated by considering the distribution of the photoinduced state (see text). In this calculation, the photoinduced state is assumed to be the HT phase (380 K). The parameters are d = 162 nm and r_0 = 0.48. (b) The schematic representation of photoinduced phase transition (Cl_2An^{3-} (LT phase) → Cl_2An^{2-} (HT phase))

The transient $\Delta R/R$ spectrum for other delay times (for example, 1 or 10 ps) can also be well-fitted using the optimal r_0 values are drawn with the experimental $\Delta R/R$ spectra in Fig. 5.11,

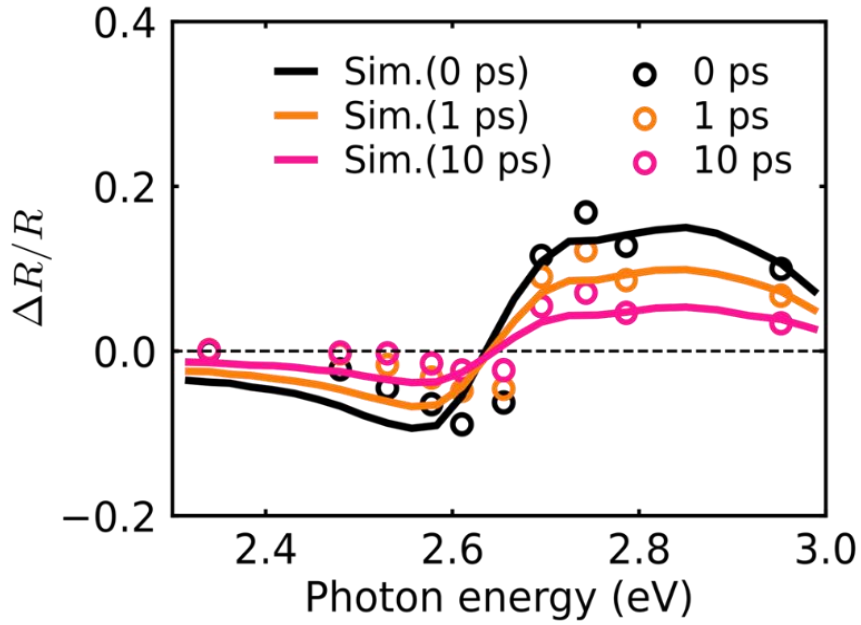

Fig. 5.11: The experimental and simulated $\Delta R/R$ spectra of 0 ps (black circles and solid black line), 1 ps (orange circles and solid orange line), and 10 ps (pink circles and solid pink line).

Since r_0 can be evaluated at any delay time using the same method of analysis, we obtained the time dependence of r_0 shown in Fig. 5.12, where we performed the fitting analysis using equation (5.1):

This result revealed a combination of two types of relaxation: a very fast relaxation on a timescale of 140 ± 32 fs (τ_1) and a slow relaxation on a timescale of 3.40 ± 0.24 ps (τ_2). In the following, we focus our discussion solely on the photoinduced state observed just after photoexcitation because the spectral shapes of $\Delta R/R$ for the photoinduced state in the observed

energy range did not show any apparent change during ~15 ps, and only the density change can explain the delay-time dependence.

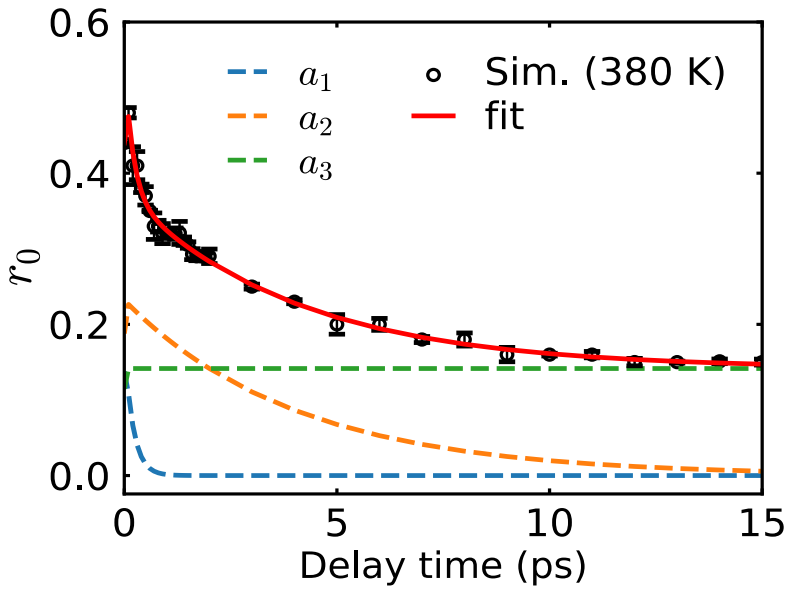

Fig. 5.12: The black circles show the values of r_0 at each delay time, along with a fit to the data (the solid red line). The temporal dependences of the three terms in equation (1) are shown as dashed lines [128].

Estimation of photo-conversion efficiency

For estimating the photo-conversion efficiency by the CT excitation, the number of the absorbed photon (N_{ph}) and the number of the excited states, Fe^{2+} and Cl_2An^{2-} pairs (N_{ex}), are evaluated as follows. N_{ph} and N_{ex} are evaluated in the cylinder of $S \times d$, as illustrated in Fig. 5.13. Here, $S = 50.24 \times 10^{-4}$ cm^2 and $d = 162$ nm are the spot size and the penetration depth of the pump light, respectively.

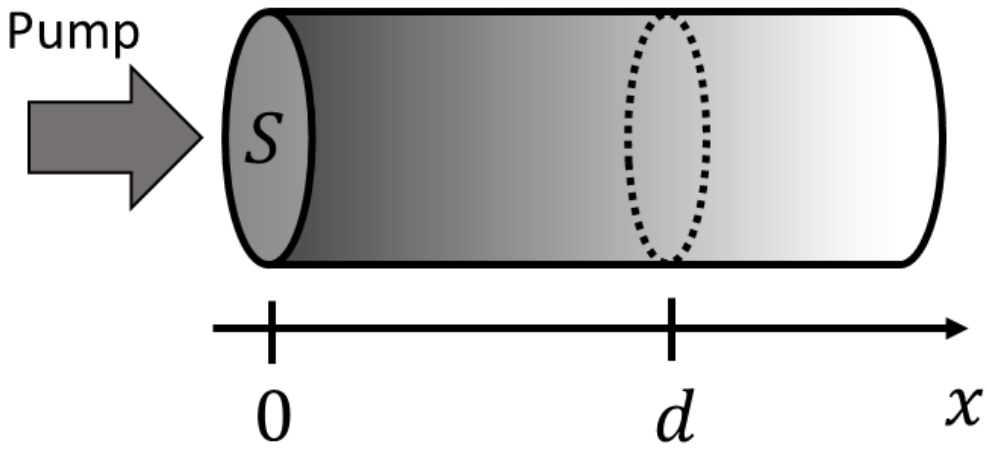

Fig. 5.13: Schematic illustration for the distribution of absorbed photon density as a function of the distance from the surface (x).

Considering the reflectivity (R) around the CT transition energy and the pump fluence (I_{pump}), N_{ph} can be expressed as the following formula.

$$N_{\mathrm{ph}} = (1-R)I_{\mathrm{pump}}S(1-e^{-1})$$

On the other hand, N_{ex} can be expressed as follows, considering our assumption of the distribution of the excited state as shown in Fig. 4.12b.

$$N_{\mathrm{ex}} = \int_0^d dx \left(\frac{2Z}{V_0}\right) S r_0 \exp\left(-\frac{x}{d}\right) = \left(\frac{2Z}{V_0}\right) r_0 S d(1-e^{-1})$$

Here, Z and V_0 are the number of formula units and the volume of the primitive cell, respectively. r_0 is the yield of the observed photoinduced state defined in the main text.

Then, the conversion efficiency is,

$$N_{\mathrm{ex}}/N_{\mathrm{ph}} = \left(\frac{2Z}{V_0}\right)\frac{r_0 d}{(1-R)I_{\mathrm{pump}}}.$$

Here, (Z/V_0) is 7.34×10^{20} /cm^3, R is 0.2, and I_{pump} is 7.7×10^{15} photons/cm^2 at 0 ps.

Therefore,

$$N_{ex}/N_{ph} = \frac{2\times7.34\times10^{20}\times0.48\times162}{0.8\times7.7\times10^{15}} = 1.85.$$

Hence, photo-conversion efficiency just after photoexcitation (N_{ex}/N_{ph}) is around 1.85 DA pair/photon.

Hence, we found that it exhibits an efficient photoinduced CT conversion between Fe and Cl_2An ions at RT by virtue of the cooperative valence instability.

As discussed in the previous sections, the observed spectral change at ultrafast speed in the intramolecular-transition range can be explained by an efficient photoinduced valence change from the LT phase (Cl_2An^{3-}) to the HT phase (Cl_2An^{2-}). This raises the naïve question of whether the photoinduced state resembles a pure HT phase. To answer this question adequately, it is essential to evaluate quantitatively the photoinduced $\Delta R/R$ spectra in the CT transition and mid-IR regions, as discussed in the following sections.

5.2.2.2 Transient *ΔR/R* spectrum in the CT energy range (0.5 – 1.5 eV)

We first want to emphasize that, as shown in Fig. 5.3(b) and Fig. 5.14(b), the shape of the photoinduced $\Delta R/R$ transient spectrum in the CT-transition energy range at RT is different from that of the thermally induced spectrum. There is a clear visible redshift at the zero-crossing point in the photoinduced *ΔR/R* spectrum just after photoexcitation (0 Ps) with respect to the thermal *ΔR/R* spectrum. A similar difference can also be observed in the transient spectrum of other delay times (1, 5, and 10 ps.)

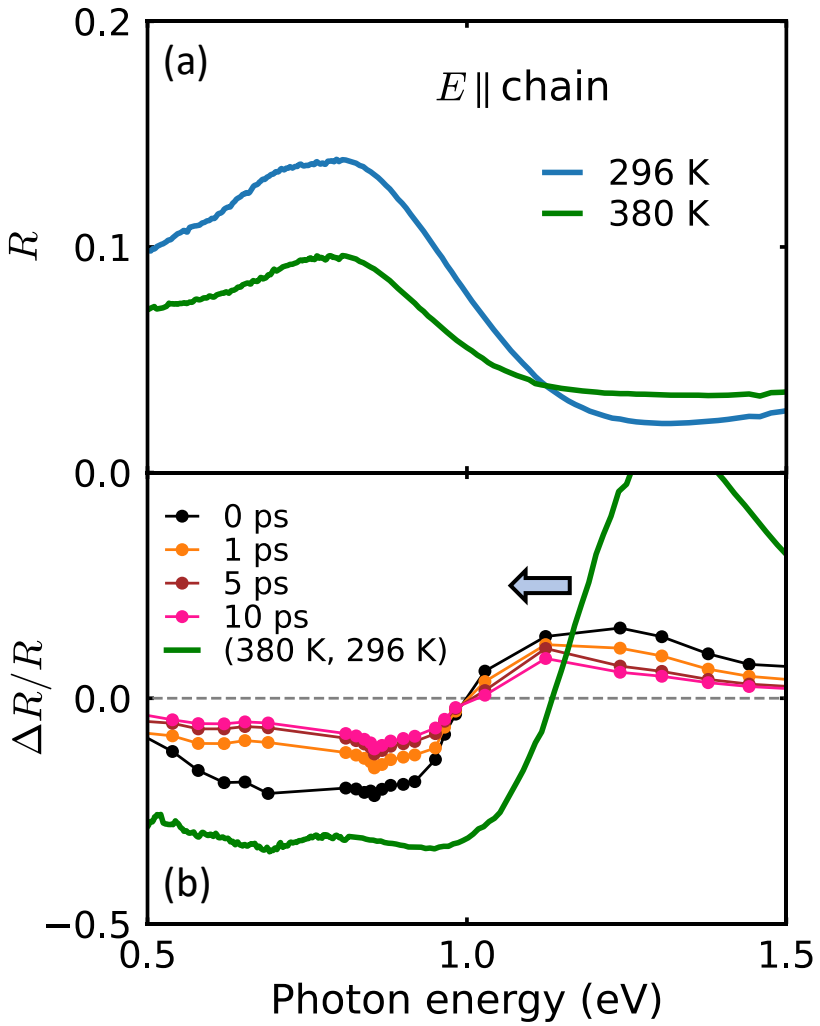

Fig. 5.14: (a) Temperature-dependent *R* spectra of a single crystal of $(NPr_4)_2[Fe_2(Cl_2An)_3]$ with *E* || chain. (b) Transient reflectivity ($\Delta R/R$) spectra with *E* || chain for pump and probe pulses at Δt = 0 (black circles), Δt = 1 (orange circles), and 10 ps (pink circles) at RT (LT phase). The

fluency of the pump pulse is I_{ex} = 1.0 mJ/cm^2. The $\Delta R/R$ spectrum with E || chain between 296 K (the LT phase) and 380 K (the HT phase) is shown as a green line within the energy range of 0.5 -1.5 eV.

In Fig. 5.15(a) and (b), we plotted the photoinduced R and optical conductivity spectrum over the photon energy range of 0.5–1.5 eV, corresponding to the CT transition energy. This spectral discrepancy is due to the appearance of a shoulder located on the higher-energy side of the R and optical conductivity spectrum, as shown in Fig. 5.15(a) and (b), which can be attributed to the photoinduced appearance of a new structure (a shoulder peak).

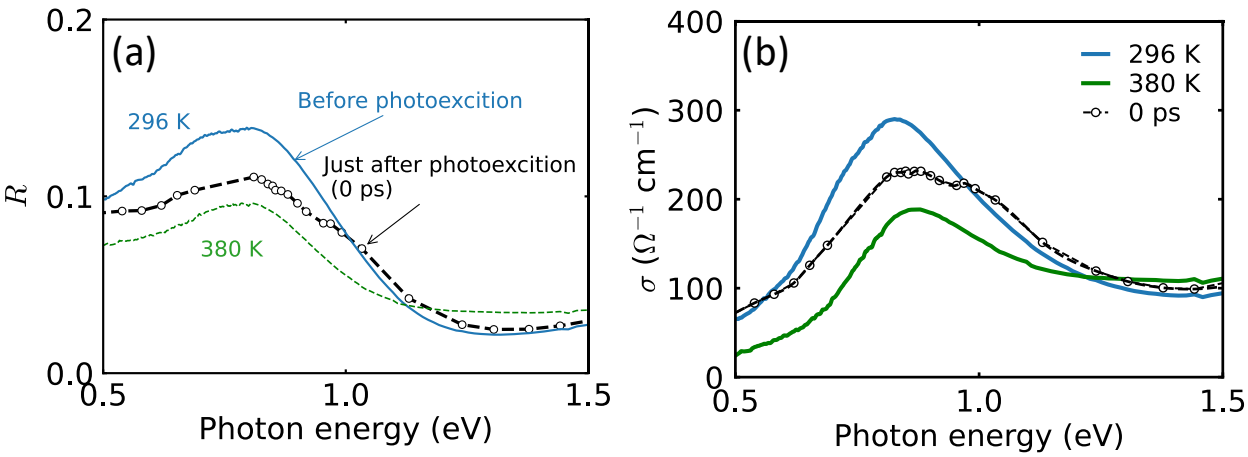

Fig. 5.15: photoinduced (a) reflectivity and (b) optical conductivity spectrum just after photoexcitation (0 ps), a clear shoulder peak is observed in the transient spectrum, which makes the photoinduced state distinct from the thermally induced one.

In the next section, we will discuss quantitatively the origin of the shoulder peak in the higher energy side of the CT band.

Quantitative analysis of transient *ΔR/R* spectrum in the CT energy range (0.5 – 1.5 eV) (method and discussion)

This section describes a simulation result for the transient ΔR/R spectrum in the CT energy range based on equation (5.2). Note that a simulation of the *R* variation using equation (2) and assuming that the photoinduced state is the HT phase (the purple line in Fig. 5.16) fails to reproduce the experimental data, even though utilizing the same parameter values for r_0 and *d* that obtained from the analysis for the intramolecular transition energy range (0 ps). This spectral discrepancy is due to the appearance of a shoulder located on the higher-energy side of the reflectivity spectrum, between 0.8 and 1.2 eV.

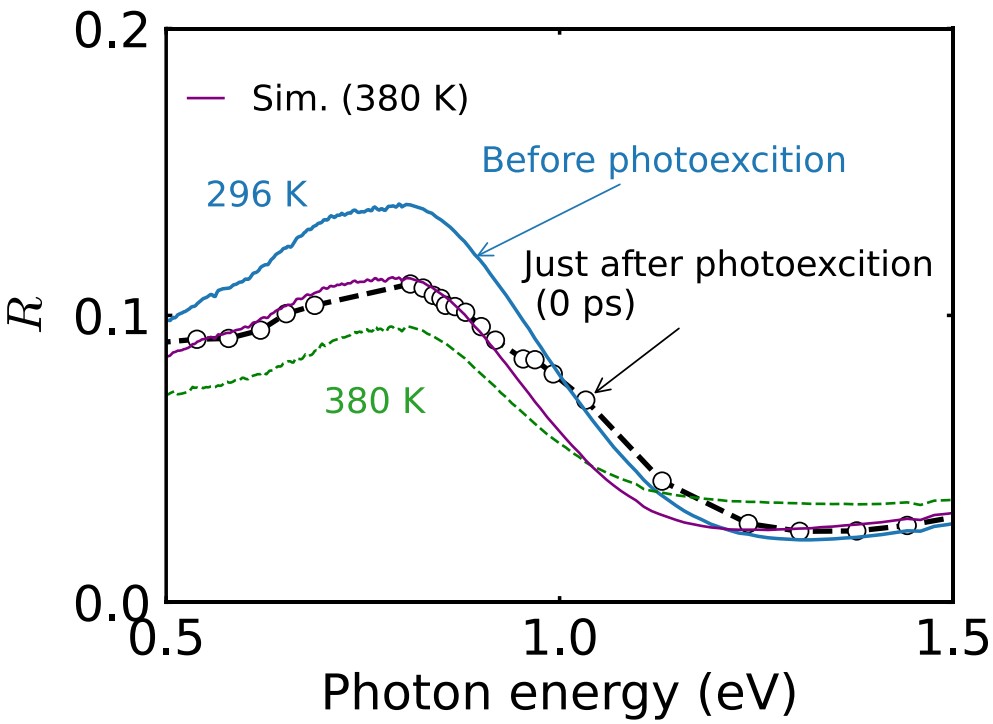

Fig. 5.16: Reflectance (*R*) spectrum of the photoinduced state of $(NPr_4)_2[Fe_2(Cl_2An)_3]$, obtained using a pump with $E \parallel$ chain and I_{ex} = 1.0 mJ/cm^2, at Δt = 0 and RT around the CT-transition range (0.5–1.5 eV). The observed spectrum is plotted as black circles. Calculated *R* spectra at 0 ps are also shown; they consider the photoinduced state to be 380 K (HT phase;

the purple line). The blue solid line and green dashed line represent the *R* spectra of the LT (296 K) and HT (380 K) phases.

To reproduce this unexpected spectral feature, we added one Lorentzian oscillator (The detail about the Lorentzian oscillator model is described in Appendix C) $\varepsilon^{l}(\omega)$ to $\varepsilon^{PI}(\omega)$ in equation (5.2) to represent another absorption feature, i.e., $\varepsilon^{PI}(\omega) = \varepsilon^{HT}(\omega) + \varepsilon^{l}(\omega)$, with

$$\varepsilon^{l}(\omega) = \frac{S_0}{\omega_0^2 - \omega^2 + i\gamma_0\omega}, \tag{5.3}$$

where ω_0, S_0, and γ_0 are the resonance frequency, oscillator strength, and damping constant, respectively, of the Lorentzian oscillator. We determined the optimal values of these parameters from a least-squares fit to the data at 0 ps. The resulting calculated photoinduced reflectivity spectrum (the thick red line in Fig. 5.17(a)) matches the experimental data (open black circles) well. The simulated σ(ω) spectrum of the photoinduced state based on this analysis is shown as the thick red curve in Fig. 5.17(b). This feature looks like a superposition of the spectrum of the HT phase (the dashed green line) and the spectrum of the new absorption feature (the dashed orange line). The peak position of the new absorption is around 1.02 ± 0.003 eV—with γ_0 = 0.22 ± 0.001 eV and S_0 = 0.20 ± 0.001 eV^2—which is significantly higher than the energy of the CT transition for either the LT or the HT phases. It is, therefore, reasonable to assume that the new absorption band can be assigned to a CT transition between D and A, i.e., to a double-peaked structure produced by the splitting of the CT transition.

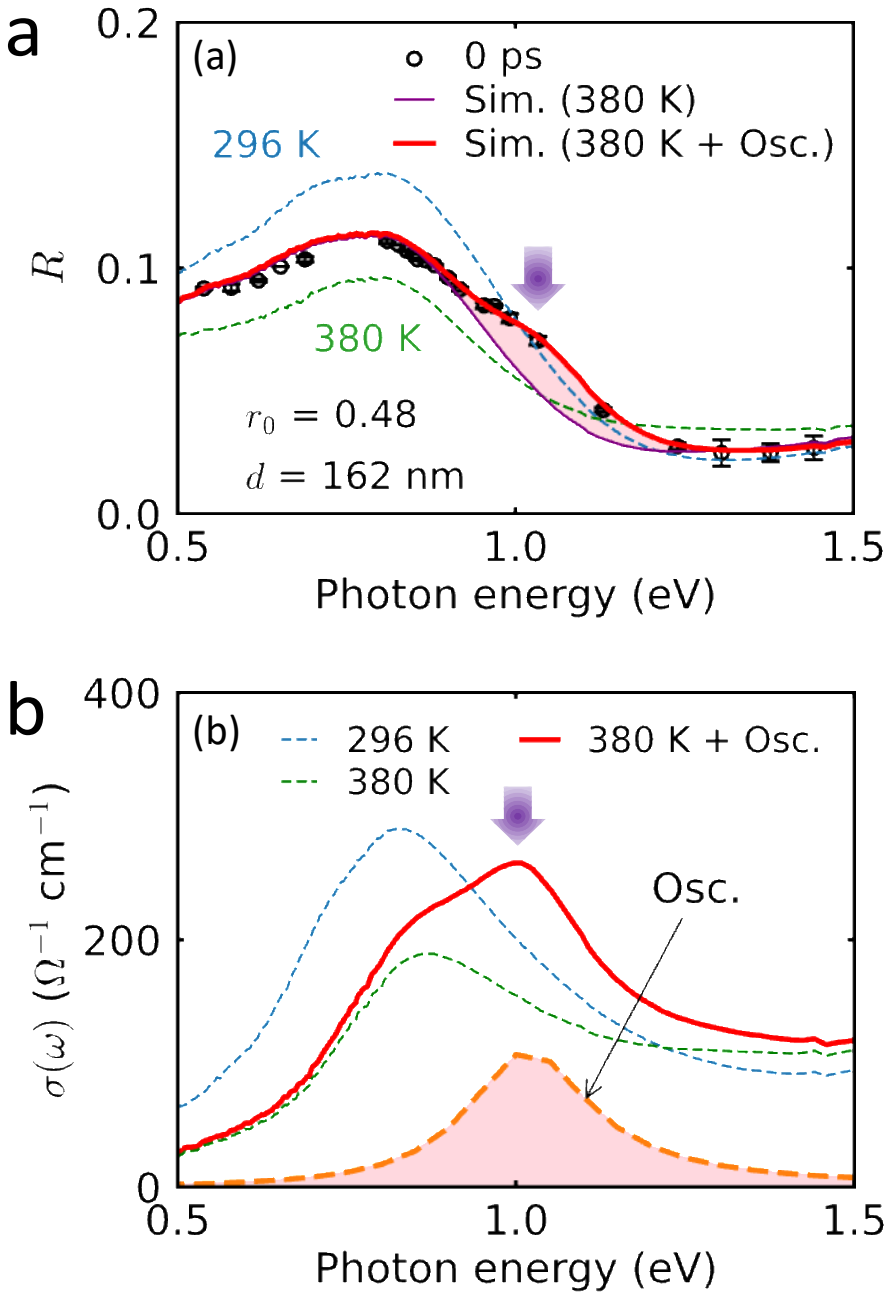

Fig. 5.17: (a) Reflectance (R) spectrum of the photoinduced state of $(NPr_4)_2[Fe_2(Cl_2An)_3]$, obtained using a pump with $E \parallel$ chain and I_{ex} = 1.0 mJ/cm^2, at Δt = 0 and RT around the CT-transition range (0.5–1.5 eV). The observed spectrum is plotted as black circles. Calculated R spectra at 0 ps are also shown; they consider the photoinduced state either to be the 380 K (HT phase; the purple line) or to be the sum of the 380 K (HT phase) and a Lorentzian oscillator (the thick red line). Details of the calculation are presented in the text. The solid pink fill shows

the difference between the purple and red lines. The dashed lines represent the *R* spectra of the LT (296 K) and HT (380 K) phases. (b) Calculated σ(ω) spectra of the photoinduced state (thick red line), 296 K (dashed blue line), and 380 K (dashed green line). The dashed orange line shows the new photoinduced absorption peak. Purple arrows indicate the resonance frequency of the Lorentzian oscillator.

Simulated Δ*R*/*R* around CT range (0.5–1.5 eV) for other delay times

In the CT energy range (from 0.5–1.5 eV), the photoinduced Δ*R*/*R* spectrum has been evaluated using equation (5.3). Here, the simulated spectra at every delay time are calculated with the same parameters set for 0 ps except r_0. Using the obtained r_0 values from the intra-molecular transition energy range analysis, the experimental data have been reproduced very well, as shown in Fig. 5.18 (for 1 and 10 ps).

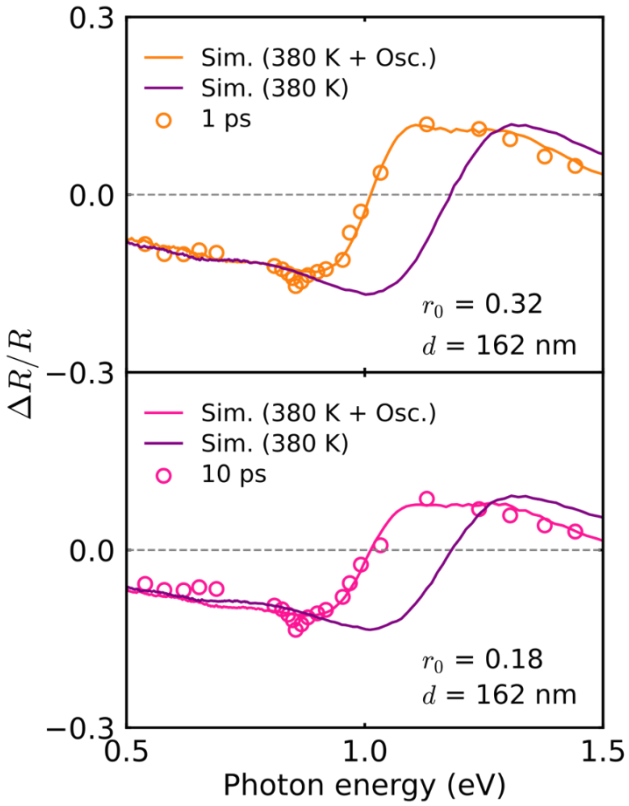

Fig. 5.18: Upper and lower panels are the Δ*R*/*R* spectra of the photoinduced state. The experimental spectra are plotted as open orange and pink circles for 1 and 10 ps, respectively.

The calculated spectra are drawn as purple [without $\varepsilon^{l}(\omega)$], orange (1 ps), and pink(10 ps) [with $\varepsilon^{l}(\omega)$] lines.

From the experimental result after photoexcitation, unexpected spectral behavior can be observed in the CT energy range. A new absorption band can be observed at the higher energy side of the CT transition. The emergence of the new peaks, which can only be observed in the photoinduced transient state, implies generating a photoinduced, thermally hidden state. This phenomenon is distinct from what we see in the thermally induced CT states. Later, we discuss the possible origin of this splitting in connection with the photoinduced spectral change in the mid-IR region, i.e., in the molecular vibration region, which will be discussed in the next part.

5.2.2.3 Transient *ΔR/R* spectrum in the mid-IR energy range (< 0.3 eV)

Experimental and optical setup

To measure time-resolved mid-IR $\Delta R/R$ (1200–2000 cm^{-1}), we detected the probe light reflected from the sample using the MCT detectors after passing it through a monochromator (Bunkokeiki M10, the only difference from our previously described setup). The energy resolution of this system was approximately 4 cm^{-1}. The schematic optical set is shown in Fig. 5.19, a monochromator is the main difference between this setup and the previous one.

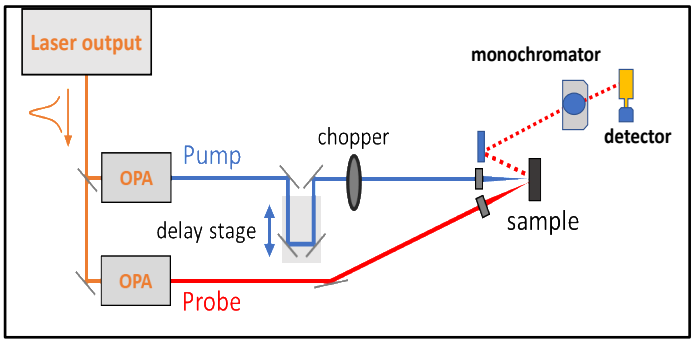

Fig. 5.19: Optical setup for reflection pump-probe measurement in mid-IR energy range.

The photoinduced transient spectra in the mid-IR energy range cannot be explained simply by photo-conversion from the LT phase to the HT phase, as shown in Fig. 5.3(b) and Fig. 5.20. After obtaining the results we sought, we should be able to come up with some interesting scientific findings. The upper panel of Fig. 5.20 High-resolution, temperature-dependent R spectra of $(NPr_4)_2[Fe_2(Cl_2An)_3]$ in the mid-IR range (1200–2000 cm^{-1}) with $E \parallel$ chain (296 K: blue line, 340 K: orange line, and 380 K: green line). The middle panel of Fig. 5.20 shows the $\Delta R/R$ with $E \parallel$ chain (black line) and $E \perp$ chain (brown line) probes for the pump with $E \parallel$ chain and I_{ex} = 1.0 mJ/cm^2 at Δt = 0 ps and RT. These spectra imply that the photoinduced spectral change is strongly anisotropic.

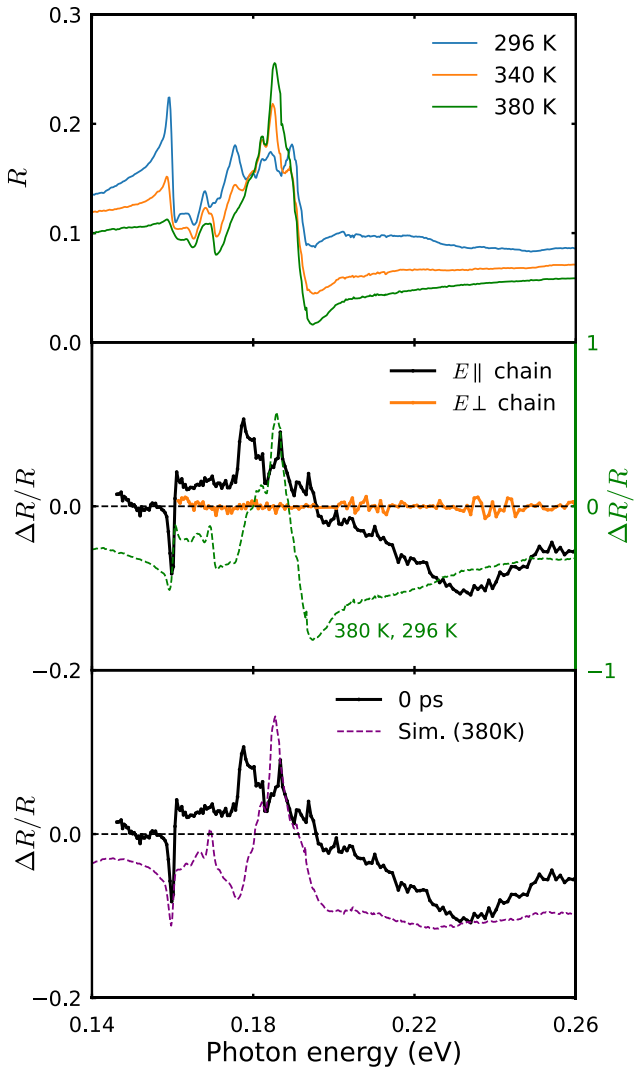

Fig. 5.20: (upper) Temperature-dependent R spectra of a single crystal of $(NPr_4)_2[Fe_2(Cl_2An)_3]$ with $E \parallel$ chain. (middle) $\Delta R/R$ with $E \parallel$ chain (black line) and $E \perp$ chain (brown line) probes

for the pump with E || chain and I_{ex} = 1.0 mJ/cm^2 at Δt = 0 ps and RT. The $\Delta R/R$ spectrum with E || chain between 296 K (the LT phase) and 380 K (the HT phase) is shown as a green dashed line. (lower) Photoinduced) $\Delta R/R$ with E || chain (black line) at Δt = 0 ps and the calculated $\Delta R/R$ spectra at 0 ps using d = 162 nm and r_0 = 0.48, considering the photoinduced state to be the 380 K (HT).

The spectrum obtained with the E ‖ chain produced a broad dispersion-type spectral shape overlapped with spiky structures due to the intramolecular vibrational modes, while the spectrum obtained with the E ⊥ chain showed no change. The differences ($\Delta R/R$) in the isothermal reflectivity spectra between 296 and 380 K are shown as green dashed lines. This suggests the clear difference between photoinduced and thermal induced $\Delta R/R$ spectrum. In the later section, by using a similar method of analysis as discussed previously during the CT energy range analysis, we will try to understand the nature of the spectral behavior and possibly the origin of this discrepancy.

The amplitude of the photoinduced $\Delta R/R$ is smaller than that of the thermally induced $\Delta R/R$ in this energy range. Since there are many spiky structures due to intramolecular vibrational modes, the energy resolution of the data in Fig. 5.3(b), where the wavelength resolution is about 150 cm^{-1}, is insufficient for this analysis. Therefore, we measured the $\Delta R/R$ spectra much more precisely to obtain better insight into the spectral nature of the photoinduced state in this range. In the setup used for this experiment, we sent the light reflected from the sample directly into a monochromator to obtain high-energy-resolution spectra with a wavelength resolution of ~6 cm^{-1}, so that the intramolecular vibration modes can be distinguished, even at the expense of a temporal resolution degraded to the order of 1 ps. The spectral width of the probe pulse in the pump-probe measurement determines the energy resolution of the photoinduced $\Delta R/R$ spectra. The spectral width of the ultrashort pulse must be wide due to the Fourier relation

between the spectral width and the temporal width. As written in the main text, the spectral width of the intramolecular vibrational structure is about 4–10 cm^{-1}. Still, the spectral width of our probe pulse is approximately 150 cm^{-1} in the mid-IR range. It is necessary to improve the energy resolution to distinguish the spiky structure. Therefore, we put the reflected light from the sample into a monochromator. This allows us to improve the energy resolution to roughly 6 cm^{-1} or less. However, the time resolution drops to about 1 ps in contrast to the improvement of the energy resolution.

Simulation of photoinduced transient spectrum in the mid-IR range

As a first step in analyzing these results, we calculated the photoinduced $\Delta R/R$ spectrum with $E \parallel$ chain using the r_0 and d values obtained in the previous analyses and assuming the photoexcited phase to be the HT phase. This result is represented by the thin-dashed purple curve in Fig. 5.21(b). There is an apparent discrepancy between this simulated curve and the experimental spectrum (the black line in Fig. 4.25(b)). This result supports the hypothesis that the photoinduced state differs from the thermally induced state. To test this hypothesis, we next included the additional Lorentzian oscillator absorption not observed in the HT phase as a second step in the simulation. We performed this spectral simulation successfully using equations (5.2) and (5.3), and the calculated $\Delta R/R$ spectrum that includes the additional oscillator (the thick red line in Fig. 5.21(b)) reproduces the curve of the experimental data considerably better, except for the spiky structures due to intramolecular vibrations. Using the least-squares fit, we determined the optimal values of the parameters for the added new absorption in the transient state to be $\omega_0 = 1570 \pm 9.06\ cm^{-1}$, $S_0 = 72.60 \pm 4.34\ cm^{-2}$, and $\gamma_0 = 403.28 \pm 5.06\ cm^{-1}$. The difference in the spiky structure due to the intramolecular vibration modes—especially those found below 1500 cm^{-1}—may reflect a difference in the molecular structure between the HT phase and the photoinduced state. Fig. 5.21(c) shows the simulated $\sigma(\omega)$ spectrum for the photoinduced state (the thick red line), including the additional new

absorption (the dashed orange curve). The peak position of the new absorption is higher than those of any of the peaks assigned to intramolecular vibrational modes, which are observed as spiky peaked structures in the spectra at 296 and 380 K (the thin blue and green dashed lines). Clarifying the parameters' delay time dependence must also be important in the mid-IR range. However, measuring the high energy-resolved spectra (precise scan) at several delay times is difficult because it takes too much time. Then, the low energy-resolved spectra (rough scan) were measured in the same energy range. The $\Delta R/R$ spectra of the precise and the rough scan at 0 ps are shown by a black line and closed circles, respectively, in Fig. 5.21(c). The rough scan's spectral shape is accurate enough to evaluate the overall structure discussed in the main text. The rough scan spectra have been measured at several delay times and compared with the simulated spectra in Fig. 5.21(d).

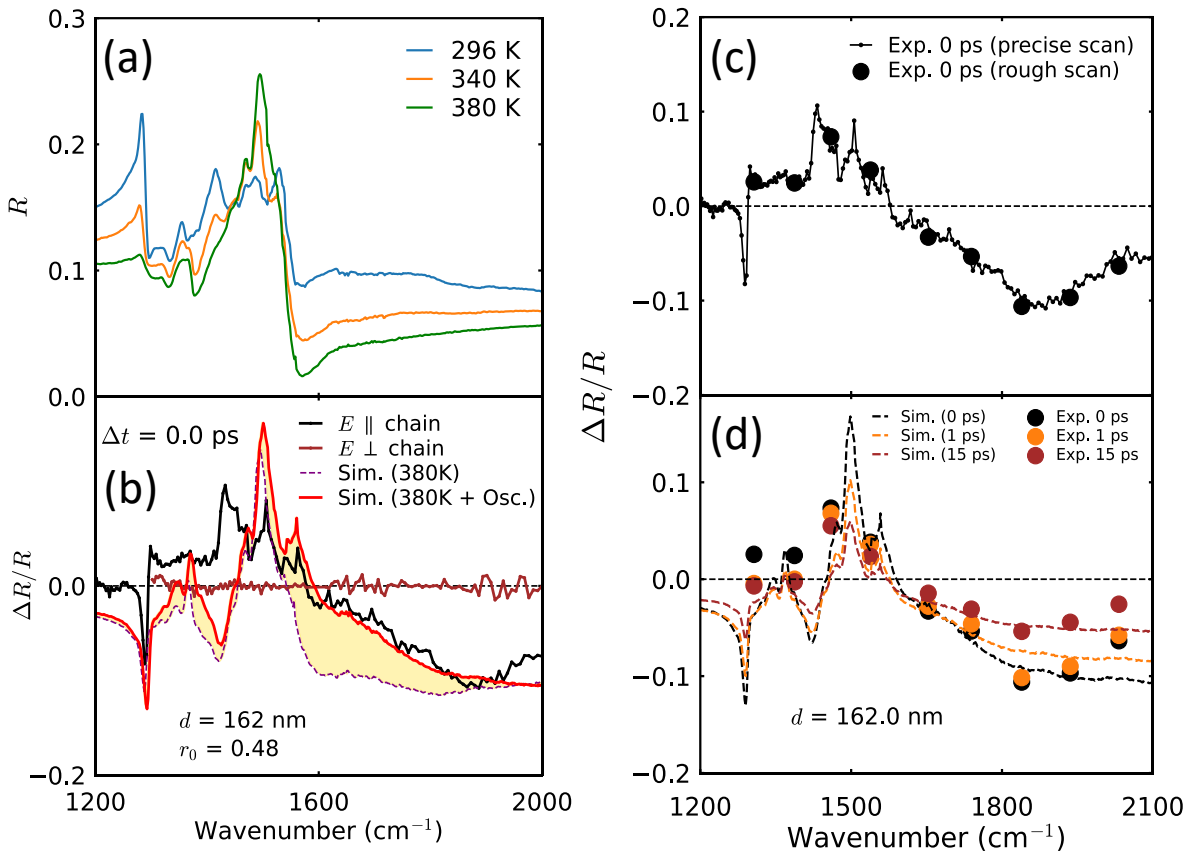

Fig. 5.21: (a) High-resolution, temperature-dependent R spectra of $(NPr_4)_2[Fe_2(Cl_2An)_3]$ in the mid-IR range (1200–2000 cm^{-1}) with $E \parallel$ chain. (b) $\Delta R/R$ with $E \parallel$ chain (black line) and $E \perp$

chain (brown line) probes for the pump with E || chain and I_{ex} = 1.0 mJ/cm^2 at Δt = 0 ps and RT. The R spectra at 0 ps, calculated using d = 162 nm and r_0 = 0.48, consider the photoinduced state to be either the 380 K (HT) phase (the purple dashed line) or the sum of the 380 K (HT) phase and a Lorentzian oscillator (the thick red line). (c) The $\Delta R/R$ spectra at 0 ps (black line: precise scan, and black circles: rough scan spectra of photoinduced $\Delta R/R$). (d) The calculated and experimental photoinduced $\Delta R/R$ spectra at the delay time of 0, 1, and 15 ps are represented by black, orange, and pink dashed lines and black, orange, and pink circles, respectively [128].

The experimental photoinduced $\Delta R/R$ results can be well reproduced by calculation [equation (5.3)] using fixed d value (162 nm), ω_0 = 1570 cm^{-1}, γ_0 = 403.28 cm^{-1}, and S_0 = 72.60 cm^{-2} and only changing the r_0 values obtained from the analysis of the intra-molecular transition energy range.

According to the results shown in Fig. 5.11 and 5.18, the photoinduced dynamics induced by the CT excitation can be explained only using the r_0 the value which reflects the degree of valence change.

To explore the origin of the new absorption in the mid-IR energy range, we compared the transient $\sigma(\omega)$ spectrum with Raman spectra (Fig. 5.22(b) and 5.22(c)), in which 'xx' and 'xy' mean that the polarization directions of the analyzer are respectively parallel and perpendicular to the polarization of the input light (E || chain). Fig. 5.22(b) shows these spectra for the HT phase (380 K), and Fig. 5.22(c) shows the 'xx' alignment spectra measured at temperatures 293, 340, and 380 K. The Raman spectra in the HT phase exhibit a characteristic mode at 1596 cm^{-1}, which is assigned to a C–O stretching mode [136] with A_g symmetry, as judged from the intensity ratio between 'xx' and 'xy'; [137] the inset of Fig. 5.22(b) depicts a schematic illustration of the atomic motions in this mode (the red arrows) [138]. Interestingly, we did not observe this C–O stretching mode at 1596 cm^{-1} in the LT phase (Fig. 5.22(c)), indicating that

this mode is related to the Cl_2An^{2-} ions. The peak position of this mode is very close to that of the new photoinduced absorption. This suggests that the Raman mode became IR-active in the photoinduced state. Considering the strongly anisotropic nature of the broad structure of $\Delta R/R$ observed and the A_g symmetry of the Raman mode at 1596 cm^{-1}, we conclude that the newly observed absorption band at around 1600 cm^{-1} in the photoinduced state can be attributed to an electron–molecular-vibration (e–MV) coupled mode. The e–MV coupled modes in DA complexes have been intensively studied in TTF–CA [139]. The CT energy between the D and A molecules becomes asymmetric because of the disappearance of the inversion centers in these molecules due to the dimerization-type lattice distortion. In other words, a totally symmetric A_g mode can become an IR-active mode in this situation. A characteristic of the e-MV coupled mode is its strong oscillator strength borrowed from the CT transition.[50] The A_g mode inherent to a single Cl_2An^{2-} ion can thus become the origin of the observed broad photoinduced IR band based on the same mechanism. That is, local inversion-symmetry breaking due to lattice modulation in the photoinduced state may induce the emergence of a new IR absorption band in the present system. Two possible structural modulations in the photoinduced state are shown schematically in Fig. 5.23(c) and 5.23(d). Model 1 is a DA-type dimer modulation similar to that in the ferroelectric I phase of TTF–CA, and model 2 represents an ADA-type trimer modulation. In model 1, the Fe-related e-MV coupled mode may be active. Therefore, observations of the Fe-related e-MV coupled modes associated with the symmetry around Fe ions are key for determining which mechanism is the actual origin of this state. Regrettably, we have not yet been able to carry out such experiments because the Fe-related e-MV coupled modes are characterized by wavenumbers—e.g., around 600 cm^{-1}—lower than those in our measurable range.

However, the lattice-modulation scenario can also be explained by another piece of evidence that is due to the appearance of the new absorption band in the CT transition region described

above: the double-peaked CT transitions tentatively associated with the disappearance of the inversion center from the Cl_2An ion in the smallest DAD model (see Appendix D). Indeed, similar observations of double-peaked structures have been reported in segregated [140] and mixed [64] stacked DA complexes with dimerization. In refs. [141] and [64], an asymmetric CT energy explained a double-peaked structure due to the disappearance of the inversion centers on the constituent molecules.

In addition to CT, lattice modulation in the 1D chain self-consistently explains the observed photoinduced spectral change in this system over the wide range of photon energies extending from the region related to intramolecular transitions to the mid-IR region. The remaining issue in this discussion concerns the speed of the lattice deformation.

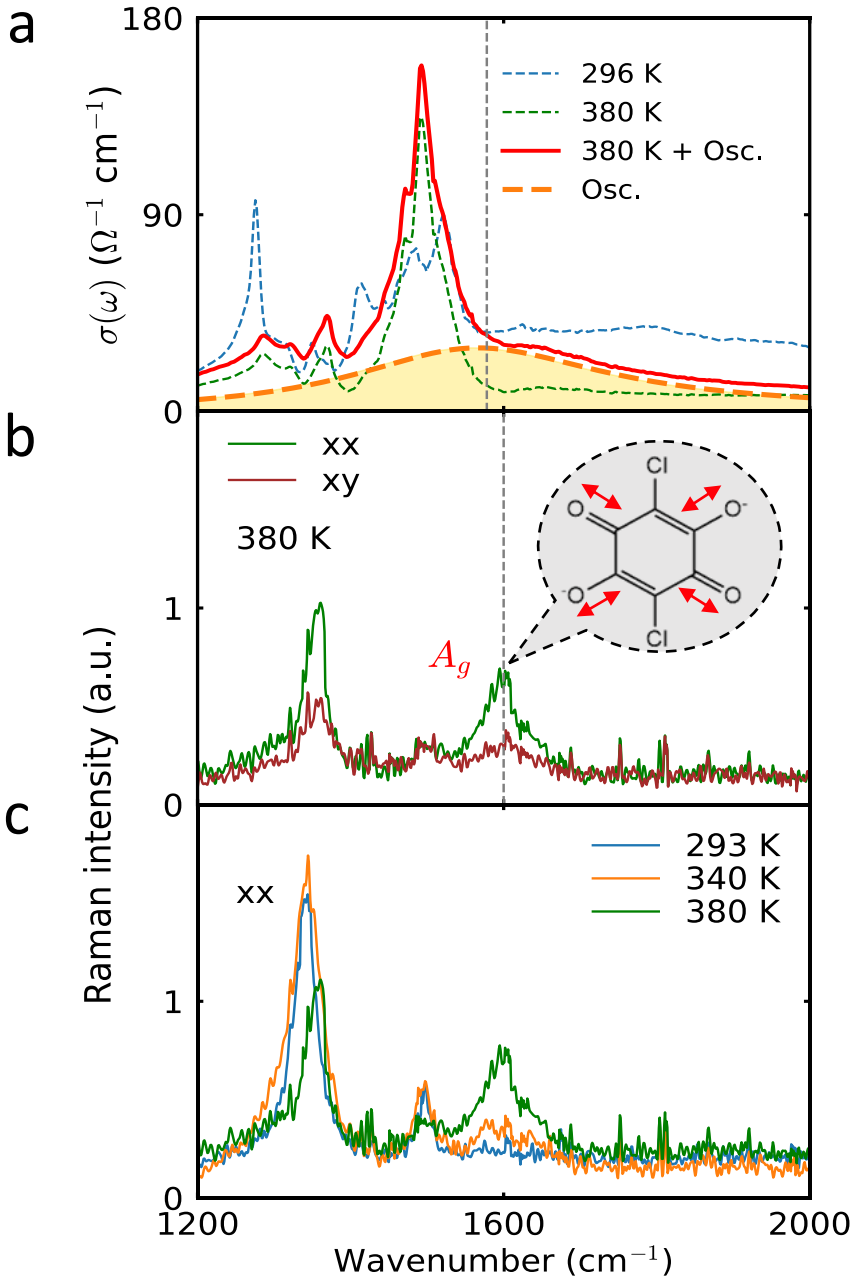

Fig. 5.22: (a) The calculated σ(ω) spectrum just after photoexcitation is shown as a thick red line. The photoinduced absorption in the model is also shown as an orange dashed line. The blue and green dashed lines are the observed σ(ω) spectra of the LT (296 K) and HT (380 K)

phases, respectively. (b) Polarized Raman spectra with 'xx' and 'xy' polarization geometries (see main text) at 380 K. The vertical dashed lines represent the oscillator's center wavenumber and the Raman spectral peak. (c) Raman spectra at 293 K (blue line), 340 K (orange line), and 380 K (green line) with 'xx' polarization geometry [128].

From the temporal dependence of $\Delta R/R$ observed in the CT-transition energy range, the structural change occurred immediately after photoexcitation, i.e., within the ~ 110 fs time resolution of our study (see Table 5.1). This timescale is much shorter than that for a typical change in the lattice structure, which, for example, was found to be ~600 fs in TTF–CA [62]. The TTF–CA system is constructed from π–π stacking between D and A; i.e., it can be described approximately as a "soft bonding" between D and A. In contrast, the present MOF system is composed of relatively "rigid bonds" between D and A so that the structural changes may be related primarily to the C–O stretching mode (around 1600 cm^{-1}) and the Fe–O stretching mode (about 600 cm^{-1}) [142], which have vibrational periods of about 20 or 60 fs, respectively. Thus, an ultrafast structural change within our time resolution (110 fs) may be reasonable.

Finally, the effect of the NPr_4^+ cations should be discussed because we neglected them during the above discussions. The initial photoexcitation occurs inside the 2D honeycomb layer, and then the successive dynamics are induced by energy transfer from the locally excited state. The time scale of the energy transfer should be evaluated by the inverse of the energy scale of the interaction. Then, we believe the dynamics related to the NPr_4^+ cation should be slower than the dynamics within the layer and can be neglected in the time scale we discussed here.

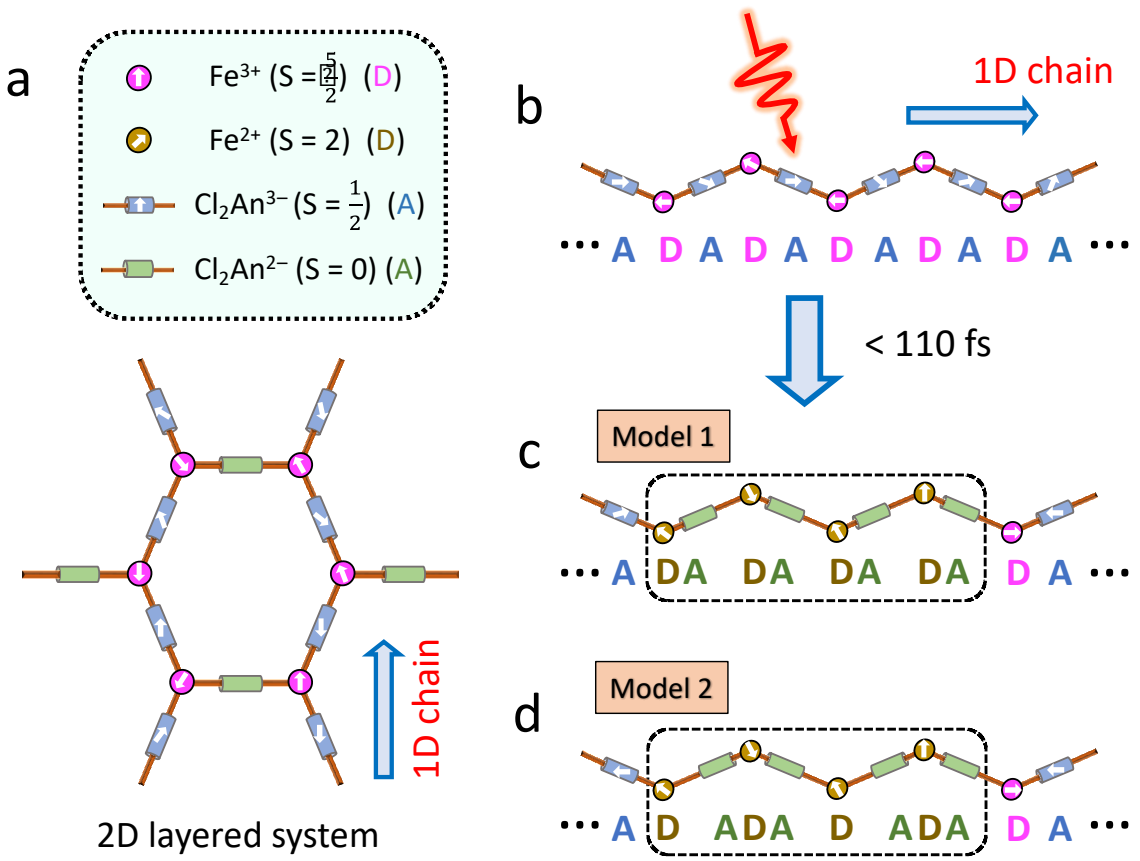

Fig. 5.23: (a) Schematic representation of the charge and spin patterns in the LT phase of the 2D-layered system $[Fe_2(Cl_2An)_3]^{2-}$. The donor units, Fe^{3+} and Fe^{2+}, are represented as pink and brown circles, respectively, whereas the acceptor units, Cl_2An^{3-} and Cl_2An^{2-}, are represented as blue and green cylinders, respectively. (b) Schematic 1D chain with DA units before photoexcitation. (c) and (d) Candidates for the photoinduced state at 0 ps. (c) DA-type dimer modulation between DA units are similar to that in the ferroelectric TTF–CA. (d) ADA-type trimer modulation [128].

Ultrafast and efficient photoinduced charge-transfer dynamics, along with a unique lattice-structure modulation, occur within 110 fs in the donor–acceptor type metal–organic framework $(NPr_4)_2[Fe_2(Cl_2An)_3]$ at room temperature (300 K). The present study provides an essential first step toward realizing flexible photo-controlled MOFs, opening the way for developing magnetically active photo-switching in such robust structures.

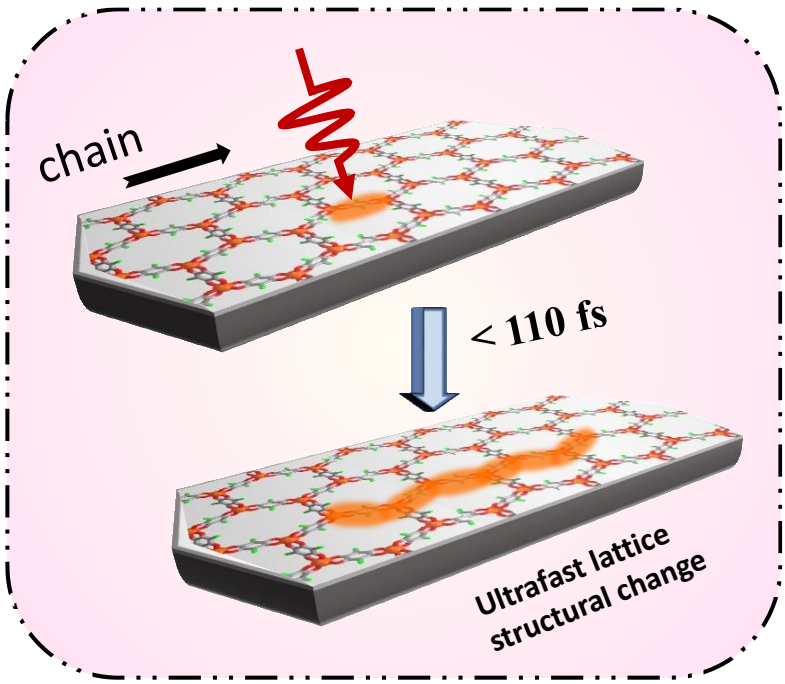

5.3 Summary

We have performed ultrafast time-resolved photoexcitation experiments using a well-shaped crystal sample of the DA-type layered MOF $(NPr_4)_2[Fe_2(Cl_2An)_3]$. We found that it exhibits an efficient photoinduced CT conversion between Fe and Cl_2An ions at RT by virtue of the cooperative valence instability. Two absorption bands emerged immediately after photoexcitation at the main CT band's higher-energy side (~ 1.02 eV) and at around 1570 cm−1 in the mid-IR energy range. The emergence of these two new peaks, which can only be observed in the photoinduced transient state, implies generating a photoinduced, thermally hidden state. This phenomenon is distinct from what we see in the thermally induced CT states. The hidden state may be produced by unexpected lattice modulations along the chain direction, with accompanying symmetry breaking of the local inversion centers on the Cl_2An ions. Two types of lattice modulations are expected, which may demonstrate a change from the SCM state to a paramagnetic and ferroelectric state similar to that of TTF–CA (model 1) or to a

paramagnetic state (model 2). It remains to be confirmed in the future whether or not this structural change involves long-range lattice and charge ordering. This will require lattice-structure measurements and magneto-optical measurements resolved on fs timescales. Ultrafast photocontrol of the charge, spin, and lattice structures in MOF systems may be quite challenging, but they will provide opportunities to develop ultrafast phase-switching systems. We also mention that the present study can be considered as a first step toward the development of high-speed photo-responsive MOFs with magnetic natures.

Note: This work is published as:

Samiran Banu, Mone Kato, Kou Takubo, Yoichi Okimoto, Shinya Koshihara, Kaoru Iwano, Wataru Kosaka, Hitoshi Miyasaka, and Tadahiko Ishikawa; Appearance of a photoinduced hidden state in the electron donor–acceptor type metal–organic framework $(NPr_4)_2[Fe_2(Cl_2An)_3]$, *Adv. Optical Mater.*, **2023**, 2301554.

Chapter 8

8. Conclusions

In this thesis, we investigated the ultrafast photoinduced dynamics of donor-acceptor-type layered MOF system, $(NPr_4)_2[Fe_2(Cl_2An)_3]$.

In Chapter 4, the static optical spectra of $(NPr_4)_2[Fe_2(Cl_2An)_3]$ for both E || chain and $E \perp$ chain have been reported. The reflectivity spectra reflect the anisotropic electronic structure of this crystal. The optical conductivity spectra led us to understand the optical transition peaks in our material. Herein, we observed two absorption peaks at around 0.8 and 2.6 eV. The peak at around 0.8 eV is attributed to the CT transition between the Fe and Cl_2An ions, while the peak at around 2.6 eV is attributed to an intramolecular transition in the Cl_2An ions. The spectral weight of each peak along the E || chain shows a steep drop at around each $T_{1/2}$ due to the LT–IM and IM–HT phase transitions. Therefore, optical spectra measurement can be utilized as suitable probes for detecting the degree of CT between the Fe and Cl_2An ions. We also measured the Raman spectra for both the E || chain and E $\perp$ chain. These results are very helpful in performing the ultrafast photoinduced study in our system.

Here, we performed the ultrafast photoinduced dynamics in $(NPr_4)_2[Fe_2(Cl_2An)_3]$ for both the LT and HT phase excitation. In chapters 5 and 6, we reported the results of LT phase excitation. In Chapter 5, we performed ultrafast time-resolved photoexcitation experiments using a well-shaped crystal sample of the DA-type layered MOF $(NPr_4)_2[Fe_2(Cl_2An)_3]$ at RT (300K). We found that it exhibits an efficient photoinduced CT conversion between Fe and Cl_2An ions at RT by the cooperative valence instability. Two absorption bands emerged immediately after

photoexcitation at the higher-energy side (~ 1.02 eV) of the main CT band and at around 1570 cm−1 in the mid-IR energy range. The emergence of these two new peaks, which can only be observed in the photoinduced transient state, implies generating a photoinduced, thermally hidden state. This phenomenon is distinct from what we see in the thermally induced CT states. The hidden state may be produced by unexpected lattice modulations along the chain direction, with symmetry breaking of the local inversion centers on the Cl_2An ions.

In Chapter 6, using a 6 fs ultra-short pulse, we can successfully observe the early-stage photoinduced dynamics of $(NPr_4)_2[Fe_2(Cl_2An)_3]$. A fast spectral change within 50 fs can be observed for both $E \parallel$ chain and $E \perp$ chain probe direction for $E \parallel$ chain CT excitation. The experimental results suggest the formation time scale for the photoinduced state, which we assigned as a structural modulation with local inversion symmetry breaking within the timescale of ~50 fs. The oscillator analysis shows that in the photoinduced state, a Raman inactive and IR active mode ~494 cm^{-1} becomes Raman active, suggesting breaking of symmetry inside D and A units leading to structural modulation.

In Chapter 7, we reported the result of photoinduced dynamics for HT phase excitation. We discussed the successful observation of revere CT behavior between D and A ($Fe^{2+} + Cl_2An^{2-} \rightarrow Fe^{3+} + Cl_2An^{3-}$) by exciting the high temperature (HT) using fs-time resolved spectroscopy (pulse width of 90 - fs). Also, in this measurement, we observed the threshold behavior for realizing reverse CT, i.e., $I_{ex} > 1.0$ mJ/cm^2, suggesting the photoinduced cooperativity effect.

In conclusion, we can mention that the present study can be considered a first step toward developing high-speed photo-responsive MOFs with magnetic nature.

Outcomes and Prospective of this research

In this research, primarily we employed the ultrafast time-resolved spectroscopic method to observe/detect the photoinduced responses from a well-shaped hexagonal DA-type MOF system, $(NPr_4)_2[Fe_2(Cl_2An)_3]$. As a major outcome from these experiments; some important features are discussed as follows:

1. Ultrafast control of electronic structure in our MOF system upon light irradiation can be well established.
2. In the process of photoinduced dynamical relaxation; within the time scale of 50 fs a unique lattice modulation ('Photoinduced hidden state') is observed. Which suggests photoinduced softening of rigid bond, which can never be achieved by thermal excitation.
3. As we observed a local inversion symmetry breaking in this system; can we expect a possibility to get a photo-ferroelectric MOF material in near future (maybe some structural modification or some other experiment is necessary to prove such comment, this is an open question to all future researcher in this field).
4. Ultrafast photoinduced bidirectional switching of valances between Fe and Cl_2An units can be observed.

As we can control the electronic structure of this material in an ultrafast time scale by photo irradiation and also make a system soft in its transient state, hence it can be easy to be modulated and apply it in various application fields. For example, it can be used in many potential application fields like Ultrafast electron storage devices, Gas sensor, fast energy transfer devices etc.

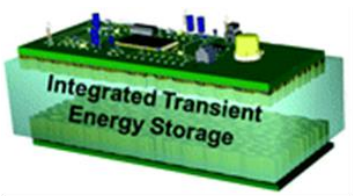

Ultrafast enegy storage devices


Gas sensor


Fast energy transfer devices

However, I believe we need to take on a challenging part in order to use such materials in real-world applications. The photo-induced research for MOF systems needs to be performed or expanded in order to make progress. Finally, it will provide the best material in terms of its application in a broader sense of how it can be applied. As a young scientist and researcher, my research represents the first step toward realizing this goal.

In addition, as a short comment for future dream, a combined excitation by 800 nm pulse and Terahertz (THz) pulse may expand the local inversion symmetry breaking. It will help us to expand the research towards realizing photo-ferroelectricity in MOF system.

Appendices

Appendix A: KRAMERS-KRONIG TRANSFORM

The Kramers - Kronig (KK) [143, 144] transformation, known in the field of reflectance spectrometry also as Robinson-Price [3, 4] analysis, is a powerful tool enabling a calculation of absorption spectra in cases where only reflectance spectra can be measured. The complex reflectance spectrum is mathematically decomposed into two separate spectra - extinction coefficient and refractive index spectrum. These are also called K and N spectra. The extinction coefficient spectrum can then be used to calculate the absorption spectrum [145].

The real (n = refractive index) and imaginary (k = extinction) parts of the complex index of refraction are calculated from the reflectance spectrum using the following formulas:

$$n(\nu) = \frac{1 - R(\nu)}{1 + R(\nu) - 2\sqrt{R(\nu)}cos(\theta(\nu))} \quad (1)$$

$$k(\nu) = \frac{-2\sqrt{R(\nu)}cos(\theta(\nu))}{1 + R(\nu) - 2\sqrt{R(\nu)}cos(\theta(\nu))} \quad (2)$$

Where R is the reflectance, n - wavenumber, θ – phase shift angle of the sample.

For a given wavenumber, the phase shift is calculated using the equation (3):

$$\theta(\nu_m) = \frac{2\,\nu_m}{\pi} \int_0^{\infty} \frac{ln\sqrt{R(\nu)}\,d\nu}{\nu^2 - {\nu_m}^2} \quad (3)$$

The KK Transform algorithm assumes that the reflectance spectra are measured at incidence angles close to zero. Calculating the integral presents two problems. First, in practice, the spectrum is obtained over a finite range, so approximations are required at either end. Second, there is a pole at $\nu = \nu_m$, which also requires an approximation. To overcome these problems, a Fourier transform is applied to solve the integral. [146, 147]

Appendix B: XYZ cluster coordinates in Fig. 4.4(b) for DFT calculation

Atomic	Coordinates (Angstroms)		
Number	X	Y	Z
Fe	–1.776	14.391	6.226
Fe	–0.739	6.537	5.75
Cl	–0.928	6.814	0.766
Cl	–5.767	17.278	5.222
Cl	–4.65	3.617	4.741
Cl	–2.044	14.081	1.247
Cl	–4.409	10.052	5.828
Cl	1.894	10.876	6.148
O	–0.347	15.723	6.598
O	–2.168	5.205	5.378
O	–4.527	15.669	0.61
O	–1.854	14.391	8.23
O	–0.66	6.537	3.746
O	–3.341	5.09	0.119
O	0.838	5.374	6.107
O	–3.353	15.554	5.869
O	–4.93	3.919	1.762
O	–0.751	6.545	7.75
O	–1.764	14.384	4.226
O	–2.857	12.611	6.2
O	0.342	8.317	5.776
O	–2.244	7.989	5.745
O	–0.271	12.939	6.231
C	0.005	15.759	7.832
C	–2.52	5.169	4.144
C	–4.175	15.634	1.844
C	–0.849	15.004	8.764
C	–1.666	5.925	3.212
C	–5.028	16.389	2.776
C	–1.94	5.935	1.86
C	–4.754	16.399	4.128

C	–3.024	5.203	1.356
C	1.156	5.261	7.344
C	–3.671	15.667	4.632
C	–3.912	4.493	2.299
C	0.267	5.971	8.287
C	–2.782	14.958	3.689
C	1.11	16.439	8.322
C	–3.625	4.489	3.654
C	–3.069	14.953	2.334
C	–2.181	11.555	6.073
C	–0.334	9.374	5.903
C	–2.69	10.286	5.911
C	0.175	10.642	6.065
C	–1.856	9.181	5.848
C	–0.658	11.747	6.128
C	–0.575	14.993	10.116
O	–6.034	17.001	2.242
C	2.24	4.529	7.848
C	0.555	5.975	9.642
C	1.398	16.435	9.677
Cl	2.136	17.312	7.235
Cl	–1.587	14.115	11.21
C	0.509	15.726	10.62
Cl	3.252	3.651	6.754
C	2.513	4.539	9.2
Cl	–0.471	6.848	10.729
C	1.66	5.295	10.132
O	2.416	17.009	10.214
O	0.827	15.839	11.857
O	3.519	3.927	9.734
O	2.012	5.259	11.366

Appendix C: Lorentzian oscillator model

Lorentz oscillator models describe bound charges' optical response. Lorentz's model is named after the Dutch physicist Hendrik Antoon Lorentz. It is a classical, phenomenological model for materials with characteristic resonance frequencies (or other characteristic energy scales) for optical absorption, e.g., vibrations in ions and molecules, interband transitions (semiconductors), phonons, and collective excitations. [149]

As a spring-mass-damper system, an electron orbits a massive, stationary nucleus [150]. A hypothetical spring connects the electron to the nucleus, and a hypothetical damper dampens its motion. At its resonance frequency, the oscillator's response is finite due to the damping force. Newton's second law can be applied to the electron to obtain its motion and expression for the dipole moment for a time-harmonic driving force generated by the electric field.

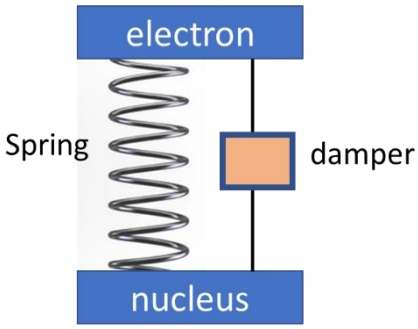

Equation of motion for electron oscillator:

$$F_{net} = F_{damping} + F_{spring} + F_{driving} = m\frac{d^2r}{dt^2}$$

$$\frac{-m}{\tau}\frac{dr}{dt} - kr - eE(t) = m\frac{d^2r}{dt^2}$$

$$\frac{d^2r}{dt^2} + \frac{1}{\tau}\frac{dr}{dt} + \omega_0^2 r = \frac{-e}{m}E(t)$$

Where,

- r is the displacement of charge from the rest position,
- t is time,
- τ is the relaxation time/scattering time,
- k is a constant factor characteristic of the spring,
- m is the effective mass of the electron,
- $\omega_0 = \sqrt{k/m}$ is the resonance frequency of the oscillator,
- e is the elementary charge,
- E(t) is the electric field.

For the time-harmonic field:

$$E(t) = E_0 e^{-i\omega t}$$

$$r(t) = r_0 e^{-i\omega t}$$

The stationary solution of this equation of motion is:

$$r(\omega) = \frac{\frac{-e}{m}}{\omega_0^2 - \omega^2 - i\omega/\tau} E(\omega)$$

Because the given solution is complex, a time delay (phase shift) exists between the driving electric field and the response of the electron's motion.

Now, in dielectric function:

Complex permittivity function using the Lorentz oscillator model can be written as:

$$\varepsilon(\omega) = \varepsilon_\infty + \sum_j \frac{S_j}{\omega_j^2 - \omega^2 + i\gamma_j\omega},$$

Here, ε_∞ is the permittivity in the high-energy region. S_j represents the vibration strength, ω_j represents the resonance frequency and γ_j represents the relaxation constant, respectively. j represents the number of oscillators to be considered, and in this analysis, its values are j = 1, 2, 3, 4……etc.

Appendix D: Optical transitions in donor-acceptor-donor (DAD) model

In the main text, the double peak structure in the absorption spectrum of the photoinduced state has been discussed and assigned the higher energy peak to the CT transition absorption due to the lattice modulation around Cl_2An^{2-} ions. The other works have already discussed the simplified picture of the CT excitation in the DA complex [139,141]. In addition, the existence of the higher energy peak has been mentioned in refs. [140] and [64]. However, there is a significant difference between the charge filling of previous works [140, 64, 151, 152] and our system. Then, the CT transition in the trimer model for our target material was evaluated here.

For simplicity, only the HOMO of D and the LUMO of A are considered for calculation. In the HT phase, the valences in the trimer unit can be written as $D^{2+}-A^{2-}-D^{2+}$. This trimer can be mapped to the two electrons in the trimer unit when only the electron number that concerns the CT transition is considered. In addition, the energy level of HOMO of D (E_D) is lower than that of LUMO of A (E_A), as shown in Fig. A1.

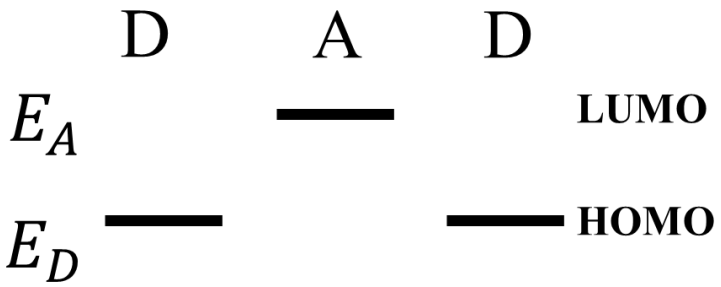

Fig. A1: The schematic representation of the energy levels of molecular orbitals for the DAD unit (HT phase).

When the double-occupied states can be neglected, considering large on-site Coulomb repulsion energy, the basis of the two-electron state can be written as follows.

$$|a\rangle \equiv |110\rangle, |b\rangle \equiv |101\rangle, |c\rangle \equiv |011\rangle$$

Here, the numbers in the ket represent the electron number in the DAD site.

The Hamiltonian for this system is, $\mathcal{H} = \sum_i E_i n_i - \sum_{i,j} t_{ij} c_j^\dagger c_i$. After the simple calculation, the matrix representation of the Hamiltonian for the above three bases is:

$$\mathcal{H} = \begin{pmatrix} E_D + E_A & -t_{32} & 0 \\ -t_{23} & 2E_D & -t_{21} \\ 0 & -t_{12} & E_D + E_A \end{pmatrix}$$

Diagonalizing the matrix, the solutions of the Schrodinger equation are as follows.

The eigenvalues:

$$E_0 - E_1,\ E_+,\ E_0 + E_1$$

Corresponding eigenvectors are:

$$\Psi_0 \equiv \begin{pmatrix} t_{32} \\ \frac{1}{2}E_- + E_1 \\ t_{12} \end{pmatrix}, \Psi_1 \equiv \begin{pmatrix} -t_{21} \\ 0 \\ t_{23} \end{pmatrix}, \Psi_2 \equiv \begin{pmatrix} t_{32} \\ \frac{1}{2}E_- - E_1 \\ t_{12} \end{pmatrix}$$

where $E_\pm \equiv E_A \pm E_D$, $E_0 \equiv E_+ - \frac{1}{2}E_-$, $W \equiv t_{12}t_{21} + t_{23}t_{32}$, and $E_1 \equiv \frac{1}{2}\sqrt{{E_-}^2 + 4W}$.

Noting that $E_- > 0$ and $E_1 = \frac{1}{2}\sqrt{{E_-}^2 + 4W} > E_+ - E_0 = \frac{1}{2}E_-$, the three states' energy levels can be schematically drawn in Fig. A2a.

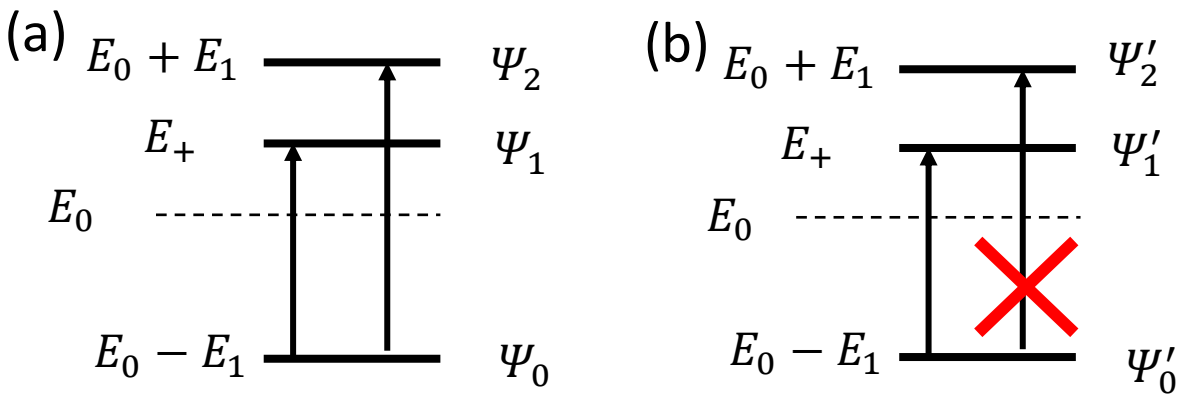

Fig. A2: Schematic energy diagram of the trimer model with two electrons. **a.** With lattice modulation. **b.** Without lattice modulation.

The ground state of the trimer model with two electrons is Ψ_0, while the excited states are Ψ_1 and Ψ_2. Therefore, two CT transitions can be considered, Ψ_0 to Ψ_1 and Ψ_0 to Ψ_2.

If we consider the no lattice modulation case, the values of t_{12} and t_{23} become equal, $t \equiv t_{12} = t_{23}$, then the eigenvectors can be expressed as:

$$\Psi_0{}' \equiv \begin{pmatrix} 1 \\ \frac{E_- + 2E_1}{2t} \\ 1 \end{pmatrix}, \Psi_1{}' \equiv \begin{pmatrix} -1 \\ 0 \\ 1 \end{pmatrix}, \Psi_2{}' \equiv \begin{pmatrix} 1 \\ \frac{E_- - 2E_1}{2t} \\ 1 \end{pmatrix}$$

$\Psi_0{}'$ and $\Psi_2{}'$ have even parity for the inversion operation, while $\Psi_1{}'$ has odd parity. Then, the CT transition from $\Psi_0{}'$ to $\Psi_2{}'$ is optically forbidden (Fig. A2b) in the no lattice modulation case, then only one CT transition can be considered.

From the above discussion, it is concluded that the lattice modulation around Cl_2An^{2-} can induce the new absorption at higher energy than the original CT transition without lattice modulation.

References

[1] P.P. Edwards, C.N.R. Rao (Eds.), Metal-Insulator Transitions Revisited, Taylor & Francis, (2005).

[2] E. Dagotto, Nanoscale Phase Separation and Colossal Magnetoresistance, in: Springer Series in Solid-State Sciences, vol. 136, Springer-Verlag,Berlin, Heidelberg, New York, (2010).

[3] R.J.D. Tilley, Perovskite: Structure-Property Relationship, John Wiley & Sons Ltd., (2016).

[4] K.A. Müller, H. Burkard, Phys. Rev. B **19**, 3593–3602 (1979).

[5] T. Wolfram, S. Ellialtioglu, Cambridge University Press, New York, (2006).

[6] K. Nasu (Ed.), Photoinduced Phase Transitions, World Scientific, New Jersey, Singapore, (2004).

[7] S. Koshihara, T. Ishikawa, Y. Okimoto, K. Onda, R. Fukaya, M. Hada, Y. Hayashi, S. Ishihara, T. Luty, *Phys. Rep.* **942**, 1-61 (2022).

[8] S. Decurtins, P. Gutlich, C. P. Kohler, H. Spiering, and A. Hauser, Chem. Phys. Lett. **105**, 1 (1984).

[9] R.S. Potember, T.O. Poehler, R.C. Benson, Appl. Phys. Lett. **41**, 548–550 (1982).

[10] S. Koshihara, Y. Tokura, T. Mitani, G. Saito, T. Koda, Phys. Rev. B **42**, 6853–6856 (1990).

[11] S. Koshihara, Y. Tokura, Y. Iwasa, T. Koda, Phys. Rev. B **44**, 431–434 (1991).

[12] S. Koshihara, Y. Takahashi, H. Sakai, Y. Tokura, T. Luty, J. Phys. Chem. B **103**, 2592–2600 (1999).

[13] S. Iwai, S. Tanaka, K. Fujinuma, H. Kishida, H. Okamoto, Y. Tokura, Phys. Rev. Lett. **88**, 057402 (2002).

[14] S. Koshihara, Y. Tokura, K. Takeda, T. Koda, Phys. Rev. Lett. **68** ,1148–1151 (1992).

[15] S. Koshihara, Y. Tokura, K. Takeda, T. Koda, Phys. Rev. B **52**, 6265–6272 (1995).

[16] M. Fiebig, K. Miyano, Y. Tomioka, Y. Tokura, Science **280**, 1925–1928 (1998).

[17] N. Ogawa, A. Shiraga, R. Kondo, S. Kagoshima, K. Miyano, Phys. Rev. Lett. 87, 256401 (2001).

[18] A. Cavalleri, Cs. Tóth, C. W. Siders, J. A. Squier, F. Rak´si, P. Forget, J. C. Kieffer, Phys. Rev. Lett. **87**, 237401(2001).

[19] P. Gütlich, A. Hauser, H. Spoering, Angew. Chem. **33**, 2024–2054 (1994).

[20] Y. Ogawa, S. Koshihara, K. Koshino, T. Ogawa, C. Urano, H. Takagi, Phys. Rev. Lett. **84**, 3181–3184 (2000).

[21] C. Enachescu, U. Oetliker, A. Hauser, J. Phys. Chem. B **106**, 9540–9545 (2002).

[22] N. Huby, L. Guerin, E. Collet, L. Toupet, J.-C. Ameline, H. Cailleau, T. Roisnel, T. Tayagaki, K. Tanaka, Phys. Rev. B **69**, 020101 (2004).

[23] Sato, T. Iyoda, A. Fujishima, K. Hashimoto, Science **272**, 704–705 (1996).

[24] S. Koshihara, A. Oiwa, M. Hirasawa, S. Katsumoto, Y. Iye, C. Urano, H. Takagi, H. Munekata, Phys. Rev. Lett. **78**, 4617–4620 (1997).

[25] T. Ishikawa, S.A. Hayes, S. Keskin, G. Corthey, M. Hada, K. Pichugin, A. Marx, J. Hirscht, R.J.D. Miller, K. Shionuma, K. Onda, Y. Okimoto, S. Koshihara, T. Yamamoto, C. Hengbo, M. Nomura, Y. Oshima, M. Abdel-Jawad, R. Kato, Science **350**, 1501–1505 (2015).

[26] M. Collet, L. Guerin, N. Uchida, S. Fukaya, H. Shimoda, T. Ishikawa, K. Matsuda, T. Hasegawa, A. Ota, H. Yamochi, et. al, Science **307**, 86 (2005).

[27] K. Onda, S. Ogihara, K. Yonemitsu, N. Maeshima, T. Ishikawa, Y. Okimoto, X. Shao, Y. Nakano, H. Yamochi, G. Saito, and S. Koshihara, Phys. Rev. Lett. **101**, 067403 (2008).

[28] A. Cavalleri, Th. Dekorsy, H. H. W. Chong, J. C. Kieffer, R. W. Schoenlein, Phys. Rev. B

70, 161102 (2004).

[29] D. J. Hilton, R. P. Prasankumar, S. Fourmaux, A. Cavalleri, D. Brassard, M. A. El Khakani, J. C. Kieffer, A. J. Taylor, R. D. Averitt, Phys. Rev. Lett. **99**, 226401 (2007).

[30] M. Rini, R. Tobey, N. Dean, J. Itatani, Y. Tomioka, Y. Tokura, R. W. Schoenlein, A. Cavalleri, Nature **449**, 72 (2007).

[31] T. Kawamoto, Y. Asai, S. Abe, Phys. Rev. B **60**, 12990 (1999).

[32] T. Kawamoto, Y. Asai, S. Abe, Phys. Rev. Lett. **86**, 348 (2001).

[33] H. Ohnishi, K. Nasu, Phys. Rev. B **79**, 054111 (2009).

[34] J. Kanasaki, E. Inami, K. Tanimura, H. Ohnishi, K. Nasu, Phys. Rev. Lett. **102**, 087402 (2009).

[35] H. Aoki, N. Tsuji, M. Eckstein, M. KOllar, T. Oka, P. Werner, Rev. Mod. Phys. **86**, 779-837 (2014).

[36] A. Dei, D. Gatteschi, C. Sangregorio, L. Sorace, Acc. Chem. Res. **37**, 827 (2004).

[37] S. Takaishi, M. Takamura, T. Kajiwara, H. Miyasaka, M. Yamashita, M. Iwata, H. Matsuzaki, H. Okamoto, H. Tanaka, S. I. Kuroda, H. Nishikawa, H. Oshio, K. Kato, M. Takata, *J. Am. Chem. Soc.* **130**, 12080 (2008).

[38] K. G. Alley, G. Poneti, J. B. Aitken, R. K. Hocking, B. Moubaraki, K. S. Murray, B. F. Abrahams, H. H. Harris, L. Sorace, C. Boskovic, *Inorg. Chem.* **51**, 3944 (2012).

[39] N. Hoshino, F. Iijima, G. N. Newton, N. Yoshida, T. Shiga, H. Nojiri, A. Nakao, R. Kumai, Y. Murakami, H. Oshio, *Nat. Chem.* **4**, 921 (2012).

[40] O. Sato, *Nat. Chem.* **8**, 644 (2016).

[41] K. Nakabayashi, M. Nishio, H. Miyasaka, *Inorg. Chem.* **55**, 2473 (2016).

[42] D. Aguilà, Y. Prado, E. S. Koumousi, C. Mathonière, R. Clérac, *Chem. Soc. Rev.* **45**, 203 (2016).

[43] J. Chen, Y. Sekine, Y. Komatsumaru, S. Hayami, H. Miyasaka, *Angew. Chem., Int. Ed.* **130**, 12219 (2018).

[44] G. Mínguez Espallargas, E. Coronado, *Chem. Soc. Rev.* **47**, 533 (2018).

[45] Joulie´, L. F.; Schatz, E.; Ward, M. D.; Weber, F.; Yellowlees, L. J., J. Chem. Soc., Dalton Trans. 799-804 (1994).

[46] Abakumov, G. A.; Cherkasov, V. K.; Nevodchikov, V. I.; Kuropatov, V. A.; Noll, B. C.; Pierpont, C. G. Inorg. Chem. **37**, 6117-6119 (1998).

[47] Auburn, P. R.; Lever, A. B. P. Inorg. Chem. **29**, 2551-2553 (1990).

[48] Kahn O.; Launay, J. P. Chemtronics **3**, 140-151(1988).

[49] Hauser, A. Coord. Chem. Rev. **111**, 275-290 (1991).

[50] H. Miyasaka, N. Motokawa, T. Chiyo, M. Takemura, M. Yamashita, H. Sagayama, T. H. Arima, *J. Am. Chem. Soc.* **133**, 5338 (2011).

[51] Kistenmacher, T. J.; Emge, T. J.; Bloch, A. N.; Cowan, D. O.Acta Cryst., Sect. B 38, 1193–1199 (1982).

[52] J. B. Torrance, J. E. Vazquez, J. J. Mayerle, and V. Y. Lee, Phys. Rev. Lett. **46**, 253 (1981).

[53] J. B. Torrance, A. Girlando, J. J. Mayerle, J. I. Crowley, V. Y. Lee, and P. Batail, Phys. Rev. Lett. **47**, 1747 (1981).

[54] Y. Tokura, T. Koda, T. Mitani, and G. Saito, Solid State Commun. **43**, 757 (1982).

[55] Y. Tokura, T. Koda, G. Saito, and T. Mitani, J. Phys. Soc. Jpn. **53**, 4445 (1984).

[56] J. Hubbard and J. B. Torrance, Phys. Rev. Lett., **47**, 1750 (1981).

[57] S. Koshihara, Y. Tokura, T. Mitani, G. Saito, T. Koda, Phys. Rev. B: Condens. Matter Mater. Phys. **42**, 6853 (1990).

[58] T. Suzuki, T. Sakamaki, K. Tanimura, S. Koshihara, Y. Tokura, Phys. Rev. B: Condens. Matter Mater. Phys. **60**, 6191(1999)**.**

[59] S. Iwai, S. Tanaka, K. Fujinuma, H. Kishida, H. Okamoto, H. Okamoto, H. Okamoto, Y. Tokura, Phys. Rev. Lett., 88, 057402 (2002).

[60] E. Collet, M. H. Lemée-Cailleau, M. B. Le Cointe, H. Cailleau, M. Wulff, T. Luty, S. Y. Koshihara, M. Meyer, L. Toupet, P. Rabiller, S. Techert, Science, 300, 612 (2003).

[61] H. Okamoto, Y. Ishige, S. Tanaka, H. Kishida, S. Iwai, Y. Tokura, Phys. Rev. B: Condens. Matter Mater. Phys. **70**, 165202 (2004).

[62] H. Uemura, H. Okamoto, *Phys. Rev. Lett.* **105**, 258302 (2010).

[63] L. Guérin, J. Hébert, M. Buron-Le Cointe, S. I. Adachi, S. Y. Koshihara, H. Cailleau, E. Collet, Phys. Rev. Lett. **105**, 246101 (2010).

[64] S. Iwai, Y. Ishige, S. Tanaka, Y. Okimoto, Y. Tokura, H. Okamoto, Phys. Rev. Lett., **96**, 057403 (2006).

[65] R. E. Morris, P. S. Wheatley, Angew. Chem., Int. Ed., **47**, 4966 (2008).

[66] H. Li, L. Li, R. B. Lin, W. Zhou, Z. Zhang, S. Xiang, B. Chen, EnergyChem., **1**,100006 (2019).

[67] W. G. Cui, T. L. Hu, X. H. Bu, Adv. Mater. (Weinheim, Ger.) **32**, 1806445 (2020).

[68] A. Dhakshinamoorthy, A. M. Asiri, H. Garcia, ChemComm **50**, 12800 (2014).

[69] W. Wang, X. Xu, W. Zhou, Z. Shao, Adv. Sci. (Weinheim, Ger.) **4**, 1600371 (2017).

[70] V. Pascanu, G. González Miera, A. K. Inge, B. Martín-Matute, J. Am. Chem. Soc. 141, 7223 (2019).

[71] Tomic, E. A. J. Appl. Polym. Sci., **9**, *3745*–3752 (1965).

[72] Furukawa, H.; Cordova, K.E.; O'Keeffe, M.; Yaghi, O.M. *Science* **341**,1230444 (2013).

[73] Yusuf, V. F.; Malek, N. I.; Kailasa, S. K. ACS Omega 7, 44507– 44531 (2022),

[74] M. Zhu, X. Wu, B. Niu, H. Guo, Y. Zhang, Appl. Organomet. Chem. **32(5)**, (2018) No. e4333.

[75] S. Abedi, A. A. Tehrani, A. Morsali, New J. Chem. **39**, 5108−5111(2015).

[76] P. Tong, J. Liang, X. Jiang, J. Li, Crit. Rev. Anal. Chem. **50**, 376−392 (2020).

[77] H. Yu, W. Zhang, S. Lv, J. Han, *G. Xiea, S. Chen,* Chem. Commun. **54**, 11901−11904 (2018).

[78] S. Duan and Y. Huang, J. Electroanal. Chem., 807, 253–260 (2017).

[79] Yanai, N., Kitayama, K., Hijikata, Y. *et al*. Nature Mater, **10**, 787–793 (2011).

[80] J. Ye, X. Li, H. Zhou, J. Zhang, Sci. China Chem. **62**,341−346 (2019).

[81] J. H. Cavka, S. Jakobsen, U. Olsbye, N. Guillou, C. Lamberti, S. Bordiga, K. P. Lillerud, J. Am. Chem.Soc. **130**, 13850−13851 (2008).

[82] Howarth, A.J.; Peters, A.W.; Vermeulen, N.A.; Wang, T.C.; Hupp, J.T.; Farha, O.K. Chem. Mater. **29**, 26–39 (2017).

[83] M. S. Khan, M. Khalid, M. Shahid, Mater. Adv. **1**, 1575-1601 (2020).

[84] M. Safaei, M. M. Foroughi,N. Ebrahimpoor, S. Jahani, A. Omidi, M. Khatami, Trends in Analytical Chemistry **118**, 401 – 425 (2019).

[85] L. Yang, X. Cui, Y. Zhang, Q. Wang, Z. Zhang, X. Suo, H. Xing, ACS Sustainable Chem. Eng. **7**, 3138–3144 (2019).

[86] K. Cheng, Y. Li, Z. Gao, F. Chen, C. You, B. Sun, Inorg. Chem. Commun. **101**, 27-31 (2019).

[87] D. Wang, Z. Liu, L. Xu, C. Li, D. Zhao, G. Ge, J. Lin, Dalton Trans. **48**, 278-284 (2019)

[88] S. Wang, B. Ye, C. An, J. Wang, Q. Li, J. Mater. Sci. 54, 4928-4941 (2019).

[89] S. Choi, M. Oh, Angew. Chem. Int. Ed. **58**, 866-871(2019).

[90] M.J. Chang, W.N. Cui, X.J. Chai, J. Liu, K. Wang, L. Qiu, J. Mater. Sci. **30**, 1-8 (2019).

[91] X. Zhang, X. Lv, X. Shi, Y. Yang, Y. Yang, J. Colloid Interf. Sci. **539**, 152-160 (2019).

[92] W. Liu, Y. Wang, L. Song, M.A. Silver, J. Xie, L. Zhang, S. Wang, Talanta **196**, 515-522 (2019).

[93] K.M. Park, H. Kim, J. Murray, J. Koo, K. Kim, Supramol. Chem. **29**, 441-445 (2017).

[94] M.X. Wu, Y.W. Yang, Adv. Mater. **29**, 1606134 (2017).

[95] M. Kotzabasaki, I. Galdadas, E. Tylianakis, E. Klontzas, Z. Cournia, G.E. Froudakis, J. Mater. Chem. B, **5**, 3277-3282 (2017).

[96] V. Gupta, S. Mohiyuddin, A. Sachdev, P.K. Soni, P. Gopinath, S. Tyagi, J. Drug Deliv. Sci. Technol. **52**, 846-855 (2019).

[97] X. J. Wan, C. X. Li, M. T. Zhang, Y. S. Chen, Chem. Soc. Rev.*, **49***, 2828-2842 (2020).

[98] M. Kim, S. U. Ryu, S. A. Park, K. Choi, T. Kim, D. Chung, T. Park, Adv. Funct. Mater.**,** **30**, 1904545 (2020).

[99] S. Holliday, Y. L. Li and C. K. Luscombe, Prog. Polym. Sci.*,* **70**, 34-51 (2017).

[100] A. Esteban, M. R. Lenze, K. Meerholz, F. Wurthner, Elementary Processes in Organic Photovoltaics*,* **272**, 193–214 (2017).

[101] J. J. Bergkamp , S. Decurtins, S. X. Liu, Chem. Soc. Rev.*,* **44** , 863-874 (2015).

[102] M. Yu, B. L. Pagenkopf, Tetrahedron*,* **61**, 321-347 (2005).

[103] D. M. Khrarnov, C. W. Bielawski, J. Org. Chem.*,* **72**, 9407-9417 (2007).

[104] B. Zhang, B. B. Qian, C. T Li, X. W. Li, H. X. Nie, M. H. Yu, Z. Chang, CrystEngComm, **24**, 5538-5551 (2022).

[105] J. S. Wu, S. W. Cheng, Y. J. Cheng, C. S. Hsu, Chem. Soc. Rev., **44**, 1113–1154 (2015).

[106] J. Zhang, W. Xu, P. Sheng, G. Zhao, D. Zhu, Acc. Chem. Res., 50, 1654–1662 (2017).

[107] P. Li, L. J. Zhou, N. N. Yang, Q. Sui, T. Gong, E. Q. Gao, Cryst. Growth Des., **18**, 7191–7198 (2018).

[108] X. L. Li, J. R. Yu, D. J. Gosztola, H. C. Fry, P. Deria, J. Am. Chem. Soc., **141**, 16849–16857 (2019).

[109] Q. W. Li, W. Y. Zhang, O. S. Miljanic, C. B. Knobler, J. F. Stoddart, O. M. Yaghi, Chem. Commun., **46**, 380–382 (2010).

[110] D. E. Williams, N. B. Shustova, Chem. – Eur. J., **21**, 15474–15479 (2015).

[111] M. C. So, G. P. Wiederrecht, J. E. Mondloch, J. T. Hupp, O. K. Farha, Chem. Commun., **51**, 3501–3510 (2015).

[112] M. Y. Guo, P. Li, S. L. Yang, R. Bu, X. Q. Piao, E. Q. Gao, ACS Appl. Mater. Interfaces, **12**, 43958–43966 (2020).

[113] J. Li, C. P. Men, Y. Q. Luo, S. J. Mo, W. H. Huang, L. Cui, Z. Anorg. Allg. Chem., **644**, 228–234 (2018).

[114] W. Kosaka, T. Morita, T. Yokoyama, J. Zhang and H. Miyasaka, Inorg. Chem., 54, 1518–1527 (2015).

[115] N. Sikdar, A. Hazra, D. Samanta, R. Haldar and T. K. Maji, Angew. Chem., Int. Ed., 59, 18479–18484 (2020).

[116] H. Fukunaga and H. Miyasaka, Angew. Chem., Int. Ed., 54, 569–573 (2015).

[117] T. Yan, Y.-Y. Li, J. Su, H.-Y. Wang and J.-L. Zuo, Chem. – Eur. J., 27, 11050–11055 (2021).

[118] G. Férey, C. Mellot-Draznieks, C. Serre, F. Millange, J. Dutour, S. Surblé, I. Margiolaki, Science, **309**, 2040–2042 (2005).

[119] D.Y. Hong, Y.K. Hwang, C. Serre, G. Férey, J.S. Chang, Adv. Funct. Mater., **19**, 1537–1552 (2009).

[120] Y. Gao, K. Liu, R. Kang, J. Xia, G. Yu, S Deng, Journal of Hazardous Materials, **359**, 248–257 (2018).

[121] B. Pattengale, S. Ostresh, C. A. Schmuttenmaer, J. Neu, Chem. Rev., **122**, 132-166 (2021).

[122] Zhu, J.; Shaikh, S.; Mayhall, N. J.; Morris, A. J.; World Scientific, 1−732 (2018).

[123] Kent, C. A.; Liu, D.; Ma, L.; Papanikolas, J. M.; Meyer, T. J.; Lin,W., J. Am.Chem. Soc., **133**, 12940−12943 (2011).

[124] Maza, W. A.; Padilla, R.; Morris, A. J.; J. Am. Chem. Soc., **137**, 8161−8168 (2015).

[125] Xu, H.-Q.; Hu, J.; Wang, D.; Li, Z.; Zhang, Q.; Luo, Y.; Yu, S.-H.;Jiang, H.-L.; .J. Am. Chem. Soc., **137**, 13440−13443 (2015).

[126] J. Chen, Y. Sekine, A. Okazawa, H. Sato, W. Kosaka, H. Miyasaka, Chem. Sci., **11**, 3610 (2020).

[127] J. Chen, Y. Sekine, Y. Komatsumaru, S. Hayami, H. Miyasaka, Angew. Chem., Int. Ed., **130**, 12219 (2018).

[128] S. Banu, M. Kato, K. Takubo, Y. Okimoto, S. Koshihara, K. Iwano, W. Kosaka, H. Miyasaka, T. Ishikawa, Adv. Optical Mater., 2301554 (2023).

[129] L. Lin, X. Bi, Y. Gu, F. Wang, J. Ye, J.Appl.Phys., **129**, 191101 (2021).

[130] E. Seres · J. Seres · C. Spielmann, Appl Phys A, **96**, 43–50 (2009)

[131] Y. Kawakami, H. Itoh, K. Yonemitsu, S. Iwai, J. Phys. B: At. Mol. Opt. Phys., **51**, 174005 (2018).

[132] T. Amano, Doctoral thesis, Tohoku University (2022).

[133] Gaussian 16, Revision C.01, M. J. Frisch, G. W. Trucks, H. B. Schlegel, G. E. Scuseria, M. A. Robb, J. R. Cheeseman, G. Scalmani, V. Barone, G. A. Petersson, H. Nakatsuji, X. Li, M. Caricato, A. V. Marenich, J. Bloino, B. G. Janesko, R. Gomperts, B. Mennucci, H. P. Hratchian, J. V. Ortiz, A. F. Izmaylov, J. L. Sonnenberg, D. Williams-Young, F. Ding, F. Lipparini, F. Egidi, J. Goings, B. Peng, A. Petrone, T. Henderson, D. Ranasinghe, V. G. Zakrzewski, J. Gao, N. Rega, G. Zheng, W. Liang, M. Hada, M. Ehara, K. Toyota, R. Fukuda, J. Hasegawa, M. Ishida, T. Nakajima, Y. Honda, O. Kitao, H. Nakai, T. Vreven, K. Throssell, J. A. Montgomery, Jr., J. E. Peralta, F. Ogliaro, M. J. Bearpark, J. J. Heyd, E. N. Brothers, K. N. Kudin, V. N. Staroverov, T. A. Keith, R. Kobayashi, J. Normand, K. Raghavachari, A. P. Rendell, J. C. Burant, S. S. Iyengar, J. Tomasi, M. Cossi, J. M. Millam, M. Klene, C. Adamo, R. Cammi, J. W. Ochterski, R. L. Martin, K. Morokuma, O. Farkas, J. B. Foresman, and D. J. Fox, Gaussian, Inc., Wallingford CT, (2016).

[134] Y. Okimoto, X. Peng, M. Tamura, T. Morita, K. Onda, T. Ishikawa, S. Koshihara, N. Todoroki, T. Kyomen, M. Itoh, Phys. Rev. Lett., **103**, 027402 (2009).

[135] M. Born and E. Wolf, Principles of Optics (Pergamon, Oxford, 1975)**.**

[136] L. Liu, J. A. Degayner, L. Sun, D. Z. Zee, T. D. Harris, Chem. Sci., **10**, 4652 (2019).

[137] T. I. Milenov, T. Tenev, I. Miloushev, G. V. Avdeev, C. W. Luo, W. C. Chou, Opt. Quantum Electron., **46**, 573 (2014).

[138] K. Nakabayashi, H. Miyasaka, Chem. - Eur. J., **20**, 5121 (2014).

[139] A. Girlando, F. Marzola, C. Pecile, J. B. Torrance, J. Chem. Phys., *79*, 1075 (1983).

[140] H. Okamoto, Y. Tokura, T. Koda, Phys. Rev. B: Condens. Matter Mater. Phys.**, 36**, 3858 (1987).

[141] A. Painelli, A. Girlando*, J. Chem. Phys,* **84**, 5655 (1986).

[142] J. A. DeGayner, I. R. Jeon, L. Sun, M. Dincă, T. D. Harris, J. Am. Chem. Soc., **139**, 4175

(2017).

[143] Dunken H.H., Stephanowitz R., Zeitschrift für Chemie, **23**, 353 (1983).

[144] Pelikán P., Čeppan M., Li.ka M.: Applications of Numerical Methods in Molecular Spectroscopy, Chap. 5, 9CRC Press, Boca Raton, (1994).

[145] Robinson T.S., Proc. Phys. Soc., London, **66B**, 969 (1953).

[146] Klucker R., Nielsen U., Comp. Phys. Commun., **6**, 187 (1983).

[147] Cameron D.G., Jones J.P., Computer Programs forInfrared Spectrophotometry XLII-XLVII, in: NRC Bulletin No. 16, p.6 (1977).

[148] Ohta K., Ishida H., Applied Spectroscopy, **42**, 952 (1988).

[149] M. Dressel, G. Grüner, "Semiconductors". Electrodynamics of Solids: Optical Properties of Electrons in Matter. Cambridge. pp. 136–172 (2002).

[150] Colton, John "Lorentz Oscillator Model" (PDF). Brigham Young University, Department of Physics & Astronomy. Brigham Young University. Retrieved 2021-11-18 (2020).

[151] M. Tanaka, Bull. Chem. Soc. Jpn., **50**, 2881 (1977).

[152] H. Okamoto, Dr. Thesis in University of Tokyo, (1988) (Unpublished).

Acknowledgements

This study has been carried out at Koshihara - Okimoto Laboratory in the School of Science, Department of Chemistry, Tokyo Institute of Technology.

I would like to express my special thanks to the supervisor Prof. Shinya Koshihara for his constant support and much insightful advice. I have no words to express my gratitude to my supervisor for his invaluable patience and feedback. Additionally, this endeavour would not have been possible without the generous support from Asst. Prof. Tadahiko Ishikawa. A special thanks to him. I am grateful to Prof. Y. Okimoto and Asst. Prof. K. Takubo for their fruitful discussion to complete my research work. The constant support of Mrs. H. Sakurai (our lab. secretory) in solving academic and technical problems is also greatly appreciated.

I am greatful to Prof. H. Miyasaka (IMR, Tohoku University) and Assoc. Prof W. Kosaka for their provision of intriguing samples and trustful cooperation. I also thank Prof. S. Iwai, Dr. T. Amano, Assoc. Prof Y. Kawakami, Asst. Prof. H. Itoh in Tohoku University, Dept. of physics, for their support in performing the 6 – fs experiment and fruitful discussions. I would also like to thank the late Prof. K. Iwano (Institute of Materials Structure Science, KEK) for his support in theoretical work.

I would also like to thank all the colleagues in our group for their benign association: Ms. M. Kato, Mr. H. Yu, Mr. A. Sugisawa, Mr. S. Shimanuki, Mr. S. Ueno, Mr. X. Wang, Mr. K. Kawasaki, Mr. Y. Saburi, Mr. K. Aoyagi, and Mr. T. Koike.

Furthermore, I am deeply grateful to my father (Late Sunil Kumar Banu), my mother (Rita Banu), and my family for their generous and encouraging support. Last but not least, I acknowledge my friends (especially S. Panja), without whom I would have completed this thesis way sooner.

For allowing me to conduct this research, I would like to thank the Tokyo Institute of Technology. My sincere gratitude goes out to all the funding and scholarships (mainly JST SPRING, Grant Number JPMJSP2106) that have made my research life in Japan possible without any difficulties.

Finally, I am grateful to my dissertation committee: Prof. Y. Okimoto, Prof. Y. Ohshima, Prof. M. Kawano, and Prof. K. Taniguchi.

– Samiran Banu